Thermodynamic and kinetic investigations into the syntheses of CdSe and CdTe nanoparticles

DISSERTATION

zur Erlangung des akademischen Grades

Doctor rerum naturalium
(Dr. rer. nat.)

vorgelegt

der Fakultät Mathematik und Naturwissenschaften
der Technischen Universität Dresden

von

Diplom Chemiker Christian Waurisch
geboren am 28. März 1984 in Hoyerswerda

Eingereicht am: 07. Mai 2012

Tag der Verteidigung: 19. Juli 2012

Die Dissertation wurde in der Zeit von Juli/2008 bis April/2012 in der Professur für Physikalische Chemie/ Elektrochemie angefertigt.

Gutachter:	Prof. Dr. rer. nat. habil. Alexander Eychmüller
	Prof. Dr. rer. nat. habil. Stefan Kaskel

To my family
Ricarda and Lena-Marie …

… and to the memory of my father
Klaus Waurisch (1958 - 2001).

„The problems of chemistry and biology can be greatly helped if our ability to see what we are doing, and to do things on an atomic level, is ultimately developed - a development which … cannot be avoided.”

Richard P. Feynman 1959

Abstract

This thesis addresses the syntheses towards high quality CdSe and CdTe nanoparticles. Therefore, thermodynamic and kinetic aspects of the hot injection method are investigated. By means of the introduction of a thermodynamically less favored nuclei species the nucleation event of CdSe quantum dot synthesis is affected. Utilizing highly reactive tin or lithium silylamides, primarily formed SnSe or Li_2Se nuclei undergo a cation exchange to the demanded CdSe particles. The further growth proceeds without the incorporation of the so called *quasi*-seed species. In this manner, the mechanism of the cation exchange-mediated nucleation is proven and optimized with respect to the required amount of the *quasi*-seed species. Furthermore, this protocol is applied to up-scaling attempts to reduce the efforts for optimization to a minimum. Following this, a successful laboratory batch up-scaling is achieved by increasing flask size as well as precursor concentrations by factors of 2 and 10, respectively.

A further possibility to thermodynamically influence the hot injection synthesis is the activation of the precursor species. By altering the injection pathway, as compared to the standard synthesis, the precursor species are differently coordinated and hence possess different thermodynamic stabilities. Investigations on the system of CdTe quantum dots lead to the result of a cation activation by the use of the thermodynamically less stable carboxylate ligands instead of phosphonates. Additionally, anion activation is suggested due to a kind of aging of the phosphine ligands via their oxidation by phosphonic acids. Furthermore, it is found that the ratio of Cd-to-Te strongly influences the formation of so called magic-sized clusters. Following the results, the smallest detectable species is determined as a cluster species with a size of 1.8 nm. The role of the magic-sized clusters is not fully resolved, but the initial growth is assumed to occur via monomer deposition onto or the fusion of the observed clusters. On the other hand, cluster dissolution is thermodynamically forced by the decreasing monomer concentration and can simply be explained by the process of Ostwald ripening via the creation of a smaller cluster species. Mechanistically this is explained by the formation of configurational deviations from the ideal closed-shell structure.

Finally the inorganic coating of the core quantum dots in investigated. Therefore, homoepitaxial coating is employed to overcome the limit in particle size by introducing additional monomer supply. As a result, following the classical crystallization theory, defined injections of precursor material during the diffusion limited growth regime allow a fine tuning of the final particle size. Nevertheless, homoepitaxial coating inevitably leads to photoluminescence quenching, whereas heteroepitaxial growth usually improves the optical quality. By means of a type I structure, CdSe/CdS/ZnS, the successive ion layer adsoption and reaction mechanism is discussed. Furthermore, alloy structures of CdSe/ZnSe with a radially gradated intermediate shell of CdZnSe are achieved by postsynthetic high temperature treatments. This annealing induces internal diffusion processes and allows exactly adjusting the emission wavelength due to defined shrinkage of the initial core size during the alloying process.

Contents

Abstract i
Contents iii
Abbreviations vii
Symbols viii

1 Introduction and objectives 1
  1.1. Motivation 3
  1.2. Properties of quantum dots 3
  1.3. Applications of quantum dots 5
  1.4. Objectives and outline 7
  1.5. References 8

2 Theoretical background to the hot injection method and related procedures 11
  2.1. Hot injection method 13
    i. Nucleation 14
    ii. Growth 16
    iii. Ripening 19
    iv. Theory of LaMer and Dinegar 20
  2.2. Seeded growth 21
    Quasi-seeded growth 21
  2.3. Core/shell heterostructures 23
  2.4. References 25

3 Thermodynamic aspects of the nucleation of CdSe QDs 29
  3.1. Introduction 31
  3.2. Synthesis optimization applying the *quasi*-seeded growth approach 32
  3.3. Proof of the reaction mechanism 34
    i. Preliminary control experiments 34
    ii. Structural and crystallographic investigations 36
    iii. Influence on the nucleation 37
  3.4. Optimization by means of *quasi*-seed concentration 40
    i. Growth kinetics 40
    ii. Quantum yield 43
    iii. Summary 45
  3.5. Nature of the *quasi*-seed precursor 45
  3.6. Laboratory batch up-scaling 49
  3.7. Conclusion and outlook 52
  3.8. References 53

4 Thermodynamic and kinetic effects on the synthesis of CdTe QDs....................55
4.1. Introduction 57
4.2. Precursor activation by altered injections..59
i. Particle growth 61
ii. Photoluminescence properties 66
iii. Conclusion...68
iv. Supporting experiments...70
v. Summary 72
4.3. CdTe magic-sized clusters and their mechanistic role 73
i. MSCs as critical nuclei..73
ii. Particle growth from MSCs as nuclei 75
iii. MSCs dissolution to free monomer..77
iv. Conclusion.. 80
v. Proposed mechanism for the MSC disappearance.............................. 80
4.4. Summary..82
4.5. Equations and calculations...84
i. Mean particle size 84
ii. QD concentration...84
iii. Monomeric cadmium concentration..85
iv. Size dispersion 85
5 Inorganic coating of CdSe and CdTe QDs 89
5. 1. Extra precursor addition 91
i. CdSe/CdSe...92
ii. CdTe/CdTe 95
5. 2. Type I core/shell heterostructures..97
i. CdSe/CdS/ZnS...97
ii. Gradated alloy structure: CdSe/ZnSe 99
5.3. Conclusion..102
5.4. References..103
6 Summary and conclusion 105
Quasi-seeded growth approach: CdSe QDs... 107
Precursor activation by altered injections: CdTe QDs....................................108
Inorganic coating: core/shell QDs 109

Appendix ... 111

A Experimental ... 113

A.1. Reagents ... 115

A.2. Precursor solutions ... 116

A.3. Synthesis of QDs ... 118

i. Synthesis of CdSe QDs ... 118

ii. Synthesis of CdTe QDs ... 120

A.4. Inorganic coating of QDs ... 120

i. Seeded growth: extra precursor addition ... 120

ii. Type I core/shell heterostructures ... 121

A.5. Purification of core and core/shell QDs ... 122

A.6. Characterization methods and apparatus ... 122

i. Optical characterization ... 122

ii. Crystallographic characterization ... 123

iii. Elemental analysis ... 123

A.7. References ... 124

B Validation of Yu's sizing equations ... 125

B.1. Yu's sizing equations ... 127

B.2. Validation using TEM measurements ... 128

i. CdTe QDs ... 128

ii. CdSe QDs ... 129

B.3. References ... 130

C Constants ... 131

C.1. Natural constants ... 133

C.2. Element and compound specific constants ... 133

i. Ionic radii in crystals ... 133

ii. Ionization potential ... 133

iii. Band gap energy ... 133

iv. Effective masses at 300 K ... 134

v. Dielectric constant ... 134

vi. Lattice constant ... 134

vii. Unit cell volume ... 134

C.3. References ... 135

D Figures and tables ... 137

List of figures ... 139

List of tables ... 143

Acknowledgment ... 145

List of publications ... 147

Erklärung ... 149

Abbreviations

Abs	absorbance
CB	conduction band
Ch.	chapter
C_i	hydrocarbon chain with i CH_x units
conc.	concentration
cf.	confer to/ with
DFT	density functional theory
eq.	equation
fig.	figure
fwhm	full width at half maximum
HDA	hexadecylamine
hi	hot injection
HOMO	highest occupied molecule orbital
ICDD: PDF	International Center for Diffraction Data: powder diffraction file
ICP-OES	inductive coupled plasma - optical emission spectroscopy
LCAO	linear combination of atomic orbitals
LED	light emitting diode
LoQ	limit of quantification
LSW	Lifshitz-Slyozov-Wagner
LUMO	lowest unoccupied molecule orbital
MSC	magic-sized cluster
NC	nanocrystal
OlAc	oleic acid
PL	photoluminescence
PSD	particle size distribution
QD	quantum dot
QY	quantum yield
qsg	quasi-seeded growth
SILAR	successive ion layer adsorption and reaction
tab.	table
TDPA	*n*-tetradecylphosphonic acid
TEM	transmission electron microscopy
TOP	*n*-trioctylphosphine
TOPO	*n*-trioctylphosphine oxide
VB	valence band
XRD	x-ray diffraction

Symbols

[MSC]	concentration of MSCs
[Sn]	tin(II) silylamide concentration
$Abs_{1^{st}}$	absorbance at first absorbance maximum
$Abs_{3.1eV}$	absorbance at 3.1 eV (400 nm)
c^*	critical concentration
c_0	initial concentration
c^∞	equilibrium monomer concentration at an infinitely flat surface
c_b	monomer concentration in bulk solution
c_c	concentration in crystal phase
c_{diff}	monomer concentration in diffusion limited regime
c_e	equilibrium solubility
c_{equil}	monomer equilibrium concentration
c_i	monomer concentration at interfacial layer at crystal surface
c_N	nuclei concentration
c_{Prec}	precursor concentration
$\langle c_{QD} \rangle$	mean QD concentration
c_{qs}	concentration of quasi-seed species
c_{react}	monomer concentration in reaction limited regime
c_{ripe}	monomer concentration in Ostwald ripening regime
c_s	concentration in solution phase
d	diameter
D	diffusion constant
d_L	diffusion layer
e^-	electron
E_g	band gap energy
h^+	hole
J	monomer flux
J_{diff}	monomer flux under diffusional control
J_{react}	monomer flux under reaction control
k	rate constant
K_1	constant (definition given in caption of eq. 2.15)
k_B	Boltzmann's constant
k_{diff}	rate constant of diffusion limited regime
k_{react}	rate constant of reaction limited regime
k_{ripe}	rate constant of Ostwald ripening regime
L	path length of light in the cuvette
M, M^{2+}	metal, metal ion
$MSC_{xxx\ nm}$	MSC with absorbance maximum at xxx nm

n	molar amount
N_A	Avogadro's number
$N_{Cd/QD}$	number of Cd atoms per QD
p^{∞}	vapor pressure of bulk
p_{NC}	vapor pressure of NCs
r	radius
R^2	coefficient of regression
r_c	critical radius
T	temperature
t_{gr}	reaction/ growth time
V_m	molar volume of crystal
V_R	total volume of reactants (reaction volume)
$\langle V_{QD} \rangle$	mean particle volume
V_{UC}	volume of the unit cell
X, X^{2-}	chalcogenide, chalcogenide ion
x	variable distance
z	number of unit ion pairs per unit cell

Greek symbols

γ	surface tension
ΔG	Gibbs free energy
ΔVij	volume difference between smaller (i) and larger particles (j)
$\Delta\mu$	supersaturation
$\varepsilon_{1^{st}}$	molar extinction coefficient at first absorbance maximum
$\varepsilon_{3.1eV}$	molar extinction coefficient at an absorbance of 3.1 eV (400 nm)
λ	wavelength of first excitonic transition
μ_c	chemical potential of crystalline phase
μ_s	chemical potential of solution phase
ν_i	vibration i, consecutive numbering
ξ	size dispersion
$\tilde{\xi}$	relative size dispersion

1

Introduction and objectives

1.1. Motivation

The research field of nanoscience deals with nanoparticular materials those properties are somehow found between macromolecular bulk solids and molecular species. In 1983/84 Louis E. Brus worked out the solutions of the Hamiltonian of a Wannier exciton in nanoparticles that is formed due to excitation of an electron from the valence to the conduction band.[1] These elementary model calculations allow the interpretation of the quantum size effects in semiconductor nanomaterials.

A methodology to versatile prepare colloidal nanoparticles is provided by the hot injection synthesis.[2] This method allows to precisely control the optical properties of a semiconducting material by adjusting size and shape as well as surface conditions.[3] An outstanding advantage of this method is given by the use of high boiling solvents and coordinating compounds as precursors to realize a nanoparticle growth at high temperatures that yields almost defect-free and well-passivated crystals. Experimentally, due to the injection a nucleation burst is induced which is accompanied by a temperature drop that theoretically results in a separation of nucleation and growth in terms of time. In practice this is somehow limited and efforts for synthesis optimization are required.

This thesis is motivated by the attempt to influence the hot injection syntheses to obtain an improved degree of control over nucleation and growth. Aim of the work is an increased reproducibility of the syntheses that result in highly monodisperse CdSe and CdTe nanoparticles of high optical quality. The results obtained by modification of the original synthesis protocols are investigated with respect to classical crystallization theory to identify the underlying reaction mechanisms.

1.2. Properties of quantum dots

Semiconductor nanoparticles, quantum dots (QDs), are solid crystalline particles with sizes on the nanometer scale ($d < 50$ nm). They exhibit unique optical and electronic properties, which are significantly influenced by the size of the inorganic crystallites. Hence, upon reaching a certain size they behave more like large molecules then bulk material. These effects are attributed to the quantum size effect: if the particle size reaches or falls below that of the bound electron-hole pair as would be present in the respective bulk material (exciton Bohr diameter), the crystallites confine the electron wave functions.[1, 4] For example, in quantum dots where a spherical shape is attributed, the electron wave function may be assumed to be confined in all three dimensions. Upon decreasing the size, the density of

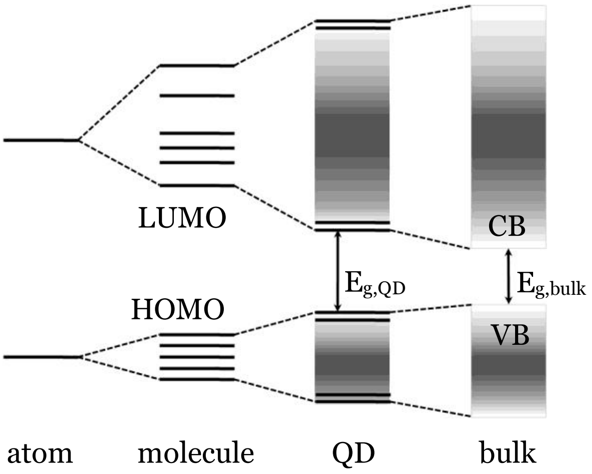

Figure 1. 1: Appropriate the LCAO theory the energetic structure from single atom to bulk semiconductor pass discrete energy levels to merge into continuous bands.

electronic states changes from being a continuous band, as found in bulk semiconductors, to discrete energy eigenfunctions in QDs and consequently the band gap increases.[5] This development is shown schematically in fig. 1.1. Starting with atoms and using the linear combination of atomic orbitals (LCAO), molecules are formed which contain a HOMO-LUMO gap. With an increasing number of atoms, QDs are formed with discrete energy states at the edges of the valence (VB) and conduction band (CB). Further addition of atoms results in the bulk semiconductor with its continuous bands.[5]

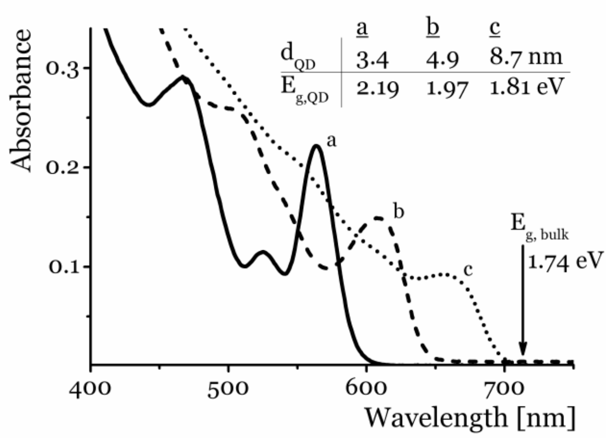

Figure 1. 2: Increasing particle sizes result in red shifted first absorbance maxima and decreased band gap energies.
Particle sizes are calculated from the respective first absorbance maximum,[6] and are used to calculate the band gap energies.[7]

Due to the quantization, the band gap increases and for small size distributions, transitions between two discrete energy levels (from VB to CB) can be determined as sharp, pronounced absorbance maxima in the respective absorption spectra. This is exemplarily shown in fig. 1.2 for CdSe quantum dots of different sizes. With increasing particle size, the band gap decreases and the discrete energy levels begin to be superimposed and the excitonic transitions (appearing as peaks) become less pronounced.

1.3. Applications of quantum dots

The most important advantage of the quantum size effect within semiconductors is the ability to adjust the band gap via the particle size. Important representatives beside transition metal oxides, e.g. ZnO and TiO_2, are binary and alloy compounds of metal pnictogens and chalcogens of the elements from group III (Al, Ga, In) and IV (Sn, Pb) as well as transition metals of group II (Zn, Cd, Hg), e.g. InP, Cd_3P_2, ZnSe or SnS). Accessible band gaps range from the near IR to close to the UV merely by adjusting the size and composition.[8]

Single or combinational processing of these nanomaterials opens a variety of applications, which mostly depend on structural, electronic as well as compositional and surface properties, e.g. crystal structure, band gap energy and position of the valence and conduction band with respect to the vacuum level and surface coating or stabilization.

By choosing the right material and adjusting its properties according to the requirements, the following applications, and many others beside, are accessible:

- *Solar cells*: applications for sun light harvesting. Many efforts have been undertaken towards different kinds of new generation solar cells. Tremendous research is on-going on the sensitization of solar cells with dye molecules, nanoparticles or both. There are two main crucial parts in nanoparticle design to achieve high efficiencies in charge carrier separation for solar cell applications: an optimal alignment of *i)* the surface properties, i.e. defined by the stabilizing ligands, and *ii)* the energy gap with its band positions, defined by the particle size.[9]

- *Solar fuel photocatalysts* may be applied for the splitting of water into hydrogen and oxygen to provide reactants within a fuel cell or, with the addition of carbon dioxide, to produce hydrocarbons. To this end, hybrids of semiconductor and metal nanoparticles are envisaged. For photocatalytic water splitting, metal sites are considered as the active site whereat protons are reduced to form hydrogen:

$$4\ H^+ + 4\ e^- \rightarrow 2\ H_2;$$

and semiconductors to oxidize hydroxide ions to form oxygen and water:

$$4\,OH^- \rightarrow O_2 + 2\,H_2O.$$

For CO_2 conversion photogenerated holes and electrons are utilized to oxidize water and to reduce carbon dioxide, respectively[10]:

$$H_2O + 2\,h^+ \rightarrow \tfrac{1}{2}\,O_2 + 2\,H^+$$

$$CO_2 + 2\,H^+ + 2\,e^- \rightarrow HCOOH.$$

- *Thermoelectric devices* convert thermal energy into electrical energy. A reasonable application would be an effective conversion of excess or waste heat from industrial processes. Thermoelectricity is based on the Seebeck effect, which is mainly caused by electron diffusion on account of a temperature gradient. Due to differences in their thermal energies electrons are induced to move and thus generate small voltages. Therefore, the thermoelectric efficiency of a material is increased with decreasing thermal conductivity and electrical resistivity. Nanoscale materials have great potential to decrease the thermal lattice conductivity due to phonon scattering at grain boundaries, however with the drawback of increased electrical resistivity due to the presence of stabilizing ligands.[11]

- *Fluorescent labels* as biomarkers within fluorescence-based biomedical imaging, i.e. tumor targeting or metabolism investigations. Comparing single quantum dots with single dye-labeled molecules many advantages become obvious, e.g. *i)* with size adjustable emission wavelength enables the use of standard protocols for the respective QD material; *ii)* their broad absorption spectrum allows the use of different excitation sources as well as simultaneous excitation; and *iii)* increased photo-stability facilitates a photo-bleaching of the surrounding biological medium before imaging. Drawbacks are the size and composition dependent toxicity, as currently used quantum dots contain toxic heavy metal ions like cadmium and may pass cell membranes.[12]

- *Light emitting diodes (LEDs)* containing quantum dots, may be used to extend the current field of colored lightning. Aside from hybrid LEDs, wherein quantum dots are excited by commercially available blue LEDs, inorganic light emitting species with organic charge transporting layers and all-inorganic LEDs, based on electroluminescence, are presently the focus of research. Advantages of all-inorganic devices are, on the one hand, extended band alignment using several semiconductor materials, and on the other increased photo-stability in comparison to organic layers.[13]

Fundamental research into all of the above mentioned applications has one important requirement: the provision of ensembles of nanoparticles with narrow size distributions. The understanding of the mechanisms present in and relevant to many applications becomes more difficult to obtain if the effects due to different nanoparticle sizes are present.

Furthermore, the surface chemistry of the nanoparticles plays a crucial role for their application. Due to their small size, the ratio of surface atoms to those within the volume is very high, i.e. 3 nm particles exhibit 50% of their atoms at the surface.[14] Thus surface states are expected due to the higher probability of surface defects occurring as well as the presence of dangling bonds and undesirable adsorbates at the particle surface.[15] Consequently, additional recombination pathways, radiative or non-radiative, are introduced, which leads to changes in their optical quality, i.e. surface state emission[16] or fluorescence quenching.[17] Therefore, passivation of the core materials with either organic or inorganic coatings has to be considered.[18] Organic shells are strongly binding ligands in addition to or as replacement for the primary stabilizing molecules, which may reduce the propensity of dangling bonds. On the other hand, inorganic coatings can lead to improvements in the initial optical properties, when utilizing type I core/shell structures, e.g. CdSe/ZnS or CdSe/ZnSe, which leads to a confinement of both charge carriers in the core material. However, completely different optical characteristics can be obtained using type II structures due to separation of the charge carriers such that one is present in the core and the other in the shell, e.g. CdSe/CdTe.[19]

1.4. Objectives and outline

The main attention in this work is paid to the syntheses of CdTe and CdSe nanoparticles with narrow size distributions and improved optical properties of the resulting particle ensembles. The overall objectives are focused on the thermodynamic and kinetic aspects of the hot injection method towards the synthesis of these quantum dots. A detailed view into the nucleation and growth mechanisms is given with respect to the investigated strategies and nanoparticle systems.

Furthermore, effects of surface coating are investigated, with inorganic shells via defined material deposition onto the core quantum dots.

Therefore this thesis is structured as follows: The theoretical background to the hot injection method and the relevant thermodynamic and kinetic models and mechanisms are given in chapter 2. Additionally, the necessity and possibilities of organic and inorganic coatings of quantum dots are considered. The following two chapters deal with the thermodynamic (Ch. 3) and kinetic (Ch. 4) considerations of the investigated syntheses with respect to CdSe and CdTe nanoparticles, respectively. Furthermore, strategies for a coating of the obtained core materials with inorganic shells of either the same or a different material are pointed out and discussed in chapter 5.

Supporting information, including all experimental details, e.g. precursor preparations and synthesis protocols are given in the Appendix. Therein, the characterization methods and techniques are also briefly explained and measurement parameters presented.

1.5. References

[1] L. E. Brus, *The Journal of Chemical Physics* **1984**, *80*, 4403.

[2] C. B. Murray, D. J. Norris, et al., *Journal of the American Chemical Society* **1993**, *115*, 8706.

[3] C. de Mello Donegá, P. Liljeroth, et al., *Small* **2005**, *1*, 1152.

[4] L. E. Brus, *The Journal of Physical Chemistry* **1986**, *90*, 2555.

[5] A. P. Alivisatos, *Science* **1996**, *271*, 933.

[6] W. W. Yu, L. Qu, et al., *Chemistry of Materials* **2003**, *15*, 2854.

[7] R. K. Čapek, I. Moreels, et al., *The Journal of Physical Chemistry C* **2010**, *114*, 6371.

[8] a) X. Peng, J. Wickham, et al., *Journal of the American Chemical Society* **1998**, *120*, 5343; b) V. Lesnyak, A. Plotnikov, et al., *Journal of Materials Chemistry* **2008**, *18*, 5142; c) S. G. Hickey, C. Waurisch, et al., *Journal of the American Chemical Society* **2008**, *130*, 14978; d) S. G. Hickey, V. Lesnyak, et al.*, Vol. 7469*, The International Society for Optics and Photonics (SPIE), **2009**, p. 746908; e) N. Gaponik, S. G. Hickey, et al., *Small* **2010**, *6*, 1364; f) S. Miao, S. G. Hickey, et al., *Journal of the American Chemical Society* **2010**, *132*, 5613; g) D. K. Harris, P. M. Allen, et al., *Journal of the American Chemical Society* **2011**, *133*, 4676.

[9] a) B. O'Regan, M. Gratzel, *Nature* **1991**, *353*, 737; b) L. M. Peter, *The Journal of Physical Chemistry C* **2007**, *111*, 6601; c) P. V. Kamat, *The Journal of Physical Chemistry C* **2008**, *112*, 18737; d) I. Mora-Seró, J. Bisquert, et al., *The Journal of Physical Chemistry C* **2007**, *111*, 14889; e) S.-C. Cui, T. Tachikawa, et al., *The Journal of Physical Chemistry C* **2008**, *112*, 19625; f) A. J. Nozik, *Nano Letters* **2010**, *10*, 2735.

[10] a) A. J. Bard, M. A. Fox, *Accounts of Chemical Research* **1995**, *28*, 141; b) E. Amouyal, *Solar Energy Materials and Solar Cells* **1995**, *38*, 249; c) P. V. Kamat, *The Journal of Physical Chemistry C* **2007**, *111*, 2834; d) C. Wang, R. L. Thompson, et al., *The Journal of Physical Chemistry Letters* **2010**, *1*, 48; e) S. C. Roy, O. K. Varghese, et al., *ACS Nano* **2010**, *4*, 1259.

[11] a) A. J. Minnich, M. S. Dresselhaus, et al., *Energy & Environmental Science* **2009**, *2*, 466; b) J. R. Sootsman, D. Y. Chung, et al., *Angewandte Chemie International Edition* **2009**, *48*, 8616.

[12] a) M. Bruchez, M. Moronne, et al., *Science* **1998**, *281*, 2013; b) X. Michalet, F. F. Pinaud, et al., *Science* **2005**, *307*, 538; c) O. T. Bruns, H. Ittrich, et al., *Nature Nanotechnology* **2009**, *4*, 193; d) A. Bartelt, O. T. Bruns, et al., *Nature Medicine* **2011**, *17*, 200.

[13] a) J. M. Phillips, M. E. Coltrin, et al., *Laser & Photonics Reviews* **2007**, *1*, 307; b) H. V. Demir, S. Nizamoglu, et al., *Nanotechnology* **2008**, *19*, 335203; c) P. O. Anikeeva, J. E. Halpert, et al., *Nano Letters* **2009**, *9*, 2532; d) V. Wood, M. J. Panzer, et al., *Nano Letters* **2010**, *10*, 24; e) J. S. Bendall, M. Paderi, et al., *Advanced Functional Materials* **2010**, *20*, 3298.

[14] K. J. Klabunde, J. Stark, et al., *The Journal of Physical Chemistry* **1996**, *100*, 12142.

[15] U. Soni, S. Sapra, *The Journal of Physical Chemistry C* **2010**, *114*, 22514.

[16] S. Sapra, S. Mayilo, et al., *Advanced Materials* **2007**, *19*, 569.

[17] a) N. Chestnoy, T. D. Harris, et al., *The Journal of Physical Chemistry* **1986**, *90*, 3393; b) J. Z. Zhang, *Accounts of Chemical Research* **1997**, *30*, 423.

[18] B. O. Dabbousi, J. Rodriguez-Viejo, et al., *The Journal of Physical Chemistry B* **1997**, *101*, 9463.

[19] A. Eychmüller, *The Journal of Physical Chemistry B* **2000**, *104*, 6514.

2

Theoretical background to the hot injection method and related procedures

2.1. Hot injection method

The hot injection method for the synthesis of semiconductor nanoparticles has been established in 1993 by Murray et al.[1] This method is based on a rapid injection of room temperature organometallic precursors into a hot solution of coordinating solvents. Upon injection, a supersaturation of the monomers and a temperature drop are imposed. Due to this monomer oversaturation homogeneous nucleation occurs, which is subsequently quenched by the temperature drop and may then be followed by a growth stage.

The general reaction mechanism for a hot injection synthesis is illustrated schematically in fig. 2.1. Starting from the time of injection, precursors of metal [M^{2+}] and chalcogenide [X^{2-}] form monomers whose concentration rapidly rises. At a given concentration, the so called oversaturation concentration, nuclei are formed. These nuclei exhibit the nature of either molecule like clusters which possess a defined number of atoms, also called magic-sized clusters (MSCs) or already formed small nanocrystals, also called quantum dots (QDs).[2]

Depending on the size of these nuclei with respect to some critical value for the system, they continue to grow or redissolve to provide more monomer to the growth solution. The subsequent growth of the nanocrystals usually occurs via monomer deposition at the nuclei surface, whereas the ideas presented in the literature concerning the process involving magic-sized clusters remain inconsistent and are presently under vigorous investigation.

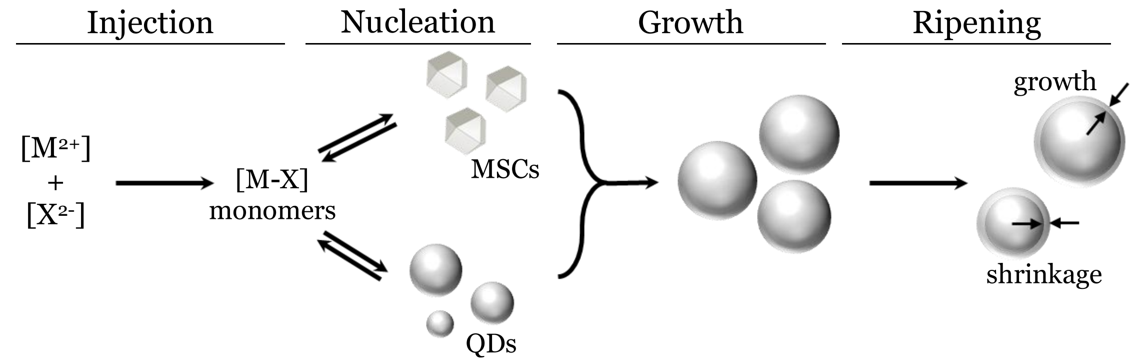

Figure 2. 1: General reaction scheme of the processes present in a standard hot injection synthesis.

[M^{2+}], [X^{2-}] denote the precursor species of the metal and the calcogenide, respectively. Detailed descriptions of the processes *Nucleation* to *Ripening* are given in the main text.

For the purposes of these studies there are three conceivable ways for nanoparticle growth involving MSCs:

- Coalescence of MSCs among each other and onto quantum dots: this mechanism suggests a decrease in chemical potential due to the agglomeration or oriented attachment, as larger particles exhibit a lower chemical potential.[3]
- Monomer deposition onto the MSCs: as MSCs possess a closed-shell structure they exhibit a high thermodynamic stability against monomer deposition. Hence they follow a discontinuous growth mechanism, which is driven by the higher thermodynamic stability of large MSCs.[2a, 4] However, Pan et al. assign those MSCs as critical nuclei within the two-phase synthesis of CdS QDs following a continuous growth mechanism.[5]
- Dissolution of the MSCs to monomers and hence acting as monomer reservoir, keeping the monomer concentration constant. This mechanism is suggested for the synthesis of different nanostructures and has already been shown within the synthesis of CdSe nanorods.[2b]

Even though only partial monomer consumption may have occurred, ripening processes may then follow. The most important ripening process, known as Ostwald ripening, is associated with the dissolution of the smaller particles (shrinkage) by feeding monomeric material to the larger particles (growth).

The general theory of the different processes (nucleation, growth, ripening) is discussed in the following sections. Furthermore, the theory of LaMer and Dinegar, and their use to describe the processes that are influential in allowing one to obtain monodisperse colloids, and the (*quasi-*) seeded growth approach as an opportunity to influence the nucleation event, are introduced.

i. Nucleation

Following the classical crystallization theory and assuming the model of a spherical isotropic particle, homogeneous nucleation depends on the nuclei size r and their corresponding Gibbs free energy ΔG:

$$\Delta G = -\frac{4}{3}\frac{\pi r^3}{V_m}(\mu_s - \mu_c) + 4\pi r^2 \gamma \qquad (2.1)$$

V_m is the molar volume of the crystal, γ is the surface tension/ energy, and μ_c and μ_s are the chemical potentials of the crystalline and the solution phase, respectively.

This equation implies that the difference in the chemical potentials of the solution and the crystalline phase ($\mu_s - \mu_c$) is the driving force of the homogeneous nucleation event. As shown in fig. 2.2, with $\mu_s < \mu_c$ the solution phase is stable and all atoms are unbound and free in the solution. In the opposite behavior $\mu_s > \mu_c$, the crystals are

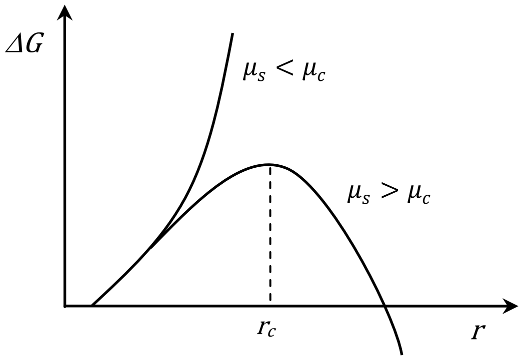

Figure 2. 2: Nuclei radius r as function of Gibbs free energy ΔG in supersaturated solutions.

thermodynamically stable and nuclei are formed. The difference in the chemical potentials represents the freed energy due to bond formations in the growing crystals. Therefore the free energy ΔG needs to reach a maximum to overcome the nucleation barrier, which is referred to as the critical radius r_c and depends on the supersaturation $\Delta\mu = \mu_s - \mu_c$.

$$\frac{d\Delta G}{dr} = 0 = -\frac{4\pi}{V_m}(\Delta\mu)r^2 + 8\pi\gamma r \quad \Rightarrow \quad r_c = \frac{2\gamma V_m}{\Delta\mu} \tag{2. 2}$$

The nucleation barrier constitutes a maximum in the progression of ΔG(r) and hence the first derivative must be zero at this point, implying the existence of a corresponding critical radius r_c.

It is important to note, that this model is based on the assumption of spherical isotropic (non-facetted) crystals and hence approximates the surface energy γ to be a constant for any size and morphology. This implication will result in appreciable errors in the presence of smaller sized materials as, compared to bulk solids, nanocrystals exhibit such small sizes that interactions of surface atoms and those inside the crystal are weaker due to short ranges between them. Additionally, nanocrystals are not completely spherical and isotropic, i.e. crystals with a cubic lattice form truncated octahedrons and hence are facetted as they possess square and hexagonal faces. These crystal facets differently contribute to the surface energy which is attributed to differences in the number of atoms and dangling bonds at the surface. A higher stability or lower surface energy is estimated by a closer packing of the atoms as well as a smaller number of unsaturated bonds at the crystal facet.[6] Throughout this work QDs are described as *spherical* although they possess a facetted shape.

In addition, determining the critical radius for a desired experiment is difficult. The sizes of the nuclei are not necessarily equal to the critical radius as, during the injection, the temperature is lowered and thus the nuclei may already have exceeded the critical radius.[7]

ii. Growth

The subsequent growth of the nanocrystals from the nuclei is differentiated into two processes: monomer diffusion to the surface of the particles and monomer deposition onto the particle surface. Therefore, the model assumes a spherical diffusion layer around the surface of the particles as depicted in fig. 2.3. Following this model the overall growth process is determined by three stages.

Stage 1. The monomer flux through the diffusion layer, as described by Fick's first law of diffusion, with the monomer diffusion coefficient D and the monomer concentration c_M:

$$J_{\text{diff}}\,(x > r) = 4\pi x^2 D \frac{dc_M}{dx} \tag{2. 3}$$

Within the limit of an infinite diffusion layer around the particles surface this equation is to be integrated from x = r to ∞, resulting in

$$J_{\text{diff}} = 4\pi r D(c_b - c_i) \tag{2. 4}$$

Stage 2. The monomer flux within the interfacial region (surface area of the particles), with a rate constant k:

$$J_{\text{react}}\,(x = r) = 4\pi r^2 k(c_i - c_e) \tag{2. 5}$$

This flux is further controlled by the rate constants for attachment and desorption of monomers. Therefore, the equilibrium solubility represents the quotient of the rate constants for desorption and adsorption of monomers at the particle surface. It is defined by the Gibbs-Thomson equation, and involves the equilibrium concentration of monomer at an infinitely flat surface c_∞ as well as the surface tension γ:[8]

$$c_e = c_\infty \cdot exp\left(\frac{2\gamma V_m}{r k_B T}\right) \tag{2. 6}$$

With k_B and T being Boltzmann's constant and temperature, respectively.

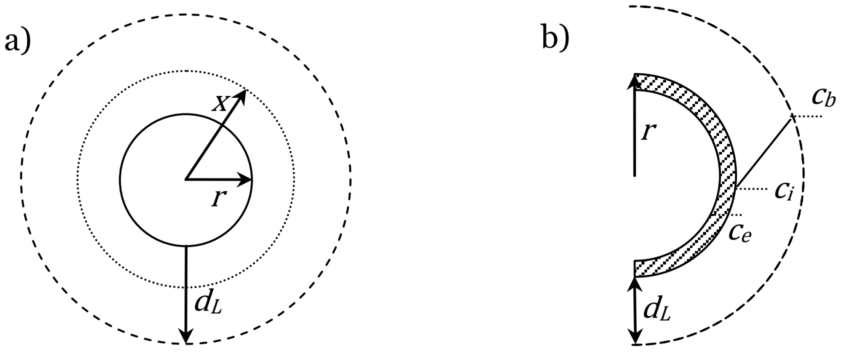

Figure 2. 3: Model of a diffusion layer around a spherical particle of radius r.
This model was introduced by Sugimoto: a) A 2 dimensional view of a nanoparticle of radius r and its corresponding diffusion layer of width d_L. The variable x is denoted as being any distance from the particle center into the diffusion layer. b) The concentration gradient is indicated by the monomer concentrations in bulk solution (c_b) and at the interfacial layer at the crystal surface (c_i) as well as the equilibrium solubility (c_e) with respect to the particle radius, with $c_b > c_i > c_e$.

Stage 3. The deposition process, considering the monomer incorporation reaction per crystal area and corresponding molar volume V_m:

$$\frac{dr}{dt} = \frac{dn}{dt}\frac{V_m}{4\pi r^2} \Leftrightarrow J = \frac{dn}{dt} = \frac{4\pi r^2}{V_m}\frac{dr}{dt} \tag{2. 7}$$

According to this model, two limitations need to be considered. First, the reaction limit or the *reaction controlled growth regime*, wherein the monomer concentration in bulk solution (c_b) is sufficiently high, that diffusion processes may be neglected and the growth rate is determined by the reaction at the particle surface. Hence, the monomer diffusivity is much larger than the monomer deposition rate ($D \gg kr$) and the interfacial monomer concentration equals that of the bulk solution ($c_i \simeq c_b$). Excluding a further precursor supply, the monomers are consumed with time and the monomer concentration in the bulk solution decreases to the value of the equilibrium solubility. Thus the diffusion becomes the rate determining step and the monomers instantaneously react at the particle surface ($D \ll kr$). This reaction stage represents the second limitation, namely the diffusion limit or *diffusion controlled growth regime*.

Within the classical theory, both limitations are considered separately. Therefore, the growth rate for the reaction and the diffusion limit can be written as given in eq. 2.8 and 2.9.

$$J_{\mathrm{react}} = \frac{dn}{dt} = 4\pi r^2 k(c_b - c_e) \Leftrightarrow \frac{dr}{dt} = V_m k(c_b - c_e) \tag{2. 8}$$

$$J_{\mathrm{diff}} = 4\pi r D(c_b - c_e) \Leftrightarrow \frac{dr}{dt} = \mathrm{D}V_m \frac{1}{r}(c_b - c_e) \tag{2. 9}$$

As described by these equations within a diffusion controlled growth regime the growth rate is decreasing with increasing particle size. This behavior is reflected by the particle size distribution (PSD[†]) as within diffusion controlled growth a narrowing in the PSD is observed. However, within a reaction controlled growth regime, the growth rate is independent of particle size and hence the size dispersion of the particle ensemble does not vary (ξ= const.). Consequently, only the relative size distribution $\tilde{\xi} = \xi/2\mathrm{r}$ is decreasing with increasing mean particle radius r.[6, 9]

[†] The PSD represents the distribution of the particle radii around an average radius and is assumed to be Gaussian. The absorbance spectrum is expected to represent the PSD and hence a Gaussian fit of the first absorbance maximum allows determining the PSD. A measure of the PSD is the size dispersion which is defined as quotient of the standard deviation of the Gaussian distribution and the average particle radius. Using a Gaussian fit of the first absorbance maximum:

$$y = y_0 + \frac{A}{w\sqrt{\pi/2}} exp\left(-2\frac{(x-x_c)^2}{w^2}\right)$$

the absolute (ξ) and the relative ($\tilde{\xi}$) size dispersion derive as:

$$\xi = \frac{w}{x_c} \qquad \tilde{\xi} = \frac{\xi}{d}$$

During the growth of nanoparticles, a narrowing of the size distribution is usually observed. Following classical theory, this is attributed to the diffusion limit and consequently eq. 2.9 is to be applied.[10] Considering the Stokes-Einstein formula for determination of the diffusion coefficient of spherical particles diffusing through a liquid, characteristic magnitudes for monomer diffusion are of the order of 10^{-11}-10^{-9} m^2/s. Applying this to eq. 2.9 with respect to nanoparticles, orders of magnitude of growth rates in the diffusion limit can be estimated:[11]

$$\frac{dr}{dt} = DV_m \frac{1}{r} c_M = 10^{-11} \frac{m^2}{s} \cdot 10^{-28} m^3 \frac{1}{10^{-9} m} 10^{25} m^{-3} = 10^{-5} \frac{m}{s} \qquad (2.\,10)$$

In comparison to experimental conditions, wherein usually much smaller growth rates (10^{-9} m/s) are determined, the growth process is thought to occur under conditions best described by the reaction limit.

Therefore, various models are proposed to simulate the growth of nanoparticles, there growth occurs in the regime of the reaction limitation.[8, 11-12] Considering the overall growth rate i.e. including both limitations, a steady state is assumed, where the reaction rate is slower or equal to the monomer diffusion to the surface. Thus, both fluxes are equal ($J_{\mathrm{react}} = J_{\mathrm{diff}}$) and the interfacial monomer concentration can be determined:

$$4\pi r^2 k(c_i - c_e) = 4\pi \mathrm{r} D(c_b - c_i) \Leftrightarrow c_i = \frac{Dc_b + rk\,c_e}{rk + D} \qquad (2.\,11)$$

The term obtained for c_i, allows the determination of the overall monomer flux by substitution of this term into eq. 2.4. In combination with eq. 2.6 and 2.7 it follows that for the size dependent growth rate:

$$\frac{dr}{dt} = \frac{DV_m k}{D + kr}\left(c_b - c_\infty exp\left(\frac{2\gamma V_m}{r k_B T}\right)\right) \qquad (2.\,12)$$

iii. Ripening

As mentioned above, the critical radius represents the nucleation barrier, which implies that particles with sizes below this threshold undergo a negative growth rate and dissolve to provide free monomer. Theoretically this event is expressed by means of the Gibbs-Thomson effect wherein smaller droplets (or crystals) have a higher vapor pressure than larger ones and thus a monomer release occurs much easier:

$$p_{NC} = p_{\infty} \cdot exp\left(\frac{2\gamma V_m}{r k_B T}\right) \tag{2. 13}$$

p_{NC} and p_{∞} denote the vapor pressures of the nanocrystals and those of an infinitely large size (i.e. bulk), respectively. For crystalline material, e.g. nanoparticles, this equation is applied for the equilibrium solubility of the material, see eq. 2.7.

As the reaction proceeds, the concentration of monomers starts to deplete and the difference in the chemical potential decreases. As described by eq. 2.2, the critical radius increases and consequently particles smaller than r_c start to dissolve while larger ones continue to grow consuming the freed monomers. This effect is named *Ostwald ripening* and affects the size dispersion in terms of broadening. Thus the size dispersion ξ is increasing while the relative size dispersion $\tilde{\xi}$ stays constant or also increases (cf. eq. 2.9).

$$\frac{d\xi}{dt} \sim \frac{dr}{dt} \rightarrow \tilde{\xi} = \text{constant}; \quad \frac{d\xi}{dt} > \frac{dr}{dt} \rightarrow \tilde{\xi} \text{ increases} \tag{2. 14}$$

The relative size dispersion in the Ostwald ripening regime cannot be decreasing, as in such a case $\mathrm{d}\xi/\mathrm{dt}$ would be smaller than $\mathrm{dr/dt}$, a situation that is not possible as larger particles grow from the released monomers supplied by the dissolution of smaller particles. If one considers two particles with a significant differences in their sizes, for monomer deposition of a full monolayer at the surface of the larger particle, more than one monolayer is required from the smaller particle, hence $\mathrm{d}\xi/\mathrm{dt} > \mathrm{dr/dt}$.[6a, 13]

However, the ripening regime may also be of benefit to the particle ensemble. In the case of annealing in coordinating solvents the quality of the crystals can be tuned. Therefore, the temperature needs to be adjusted correctly, such that diffusion processes are induced, but Ostwald ripening does not occur. Diffusion processes inside the crystals increase the crystallinity and improve the internal structure, e.g. internal defects may be repaired, while diffusion of coordinating ligands at the particles surface may improve the surface passivation. These effects will be discussed further in section 2.3 and chapter 5.[1, 14]

iv. Theory of LaMer and Dinegar

When describing the dependence of size focusing on the initial size distribution, the theory of LaMer and Dinegar for the production of monodispersed colloids needs to be considered.[15]

Within this theory a separation of nucleation and growth in time is attributed to obtain particle ensembles with narrow size distributions. In accordance with fig. 2.4, this is imposed by a nucleation burst and hence the aforementioned oversaturation. Therefore, the nucleation event depends on the concentration of the monomers. Due to the injection, the monomer concentration increases rapidly (stage I) and as soon as a minimum or critical concentration c^* is exceeded, self-nucleation takes place. This induces a partial relief of the supersaturation (stage II) and consequently, the nucleation event is quenched if the monomer concentration falls below the critical value. Subsequently, the particles are induced to melt (as a contribution to stage I) or allowed to grow (stage III).The succeeding process mainly depends on the size of the nuclei with regard to the free energy ΔG, following the classical crystallization theory as mentioned earlier. If the nuclei size falls below the critical radius, the nuclei dissolve and in the opposite case, if the nuclei exceed the critical radius, they start growing. This additionally supports the inhibited nucleation in stage I of the LaMer-Dinegar-plot (fig. 2.4), as it represents sizes smaller than the critical radius.

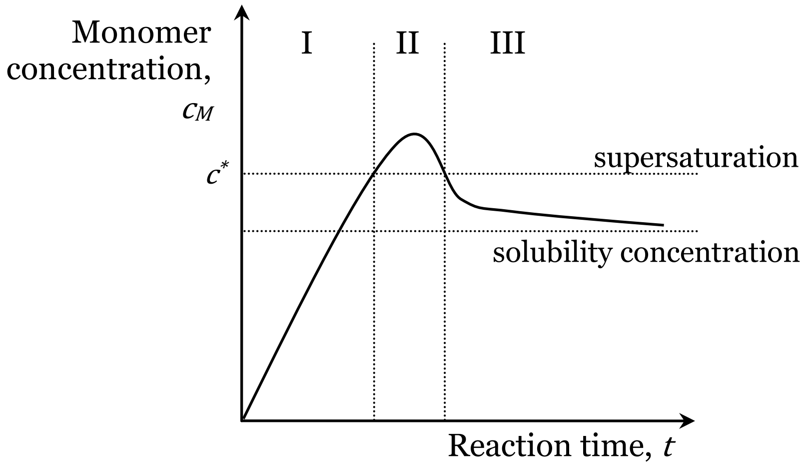

Figure 2. 4: LaMer-Dinegar-plot: development of monomer concentration with proceeding reaction.

Starting with the injection at t = 0, the monomer concentration increases in stage I. Exceeding c^*, homogeneous self-nucleation occurs with partial relief of the supersaturation in stage II. Followed by the crystal growth (stage III), which proceeds as long as the solubility concentration is exceeded.

2.2. Seeded growth

An important variation of the hot injection method is *seeded growth*, where heterogeneous nucleation is intended. Here, crystal seeds are introduced as nuclei which are then allowed to grow. This technique plays a major role in the directed growth of nanostructures as well as the synthesis of heterostructured particles. Seed mediated growth of nanostructures follows the solution-liquid-solid (SLS) mechanism. This means that the material to be deposited onto the seeds first forms an alloy with the seeds. As the concentration of the dissolved monomers at the surface of the seed increases to supersaturation, the nanostructure, e.g. a nanowire, grows out from the seed.[16]

However, heterostructures include the seed within the nanostructure. These core/shell structures can be formed isotropicly (preservation of the seeds shape) or anisotropicly (with changes in the shape). Therefore, the crystal structure of the seeds has significant influence. E.g. coating of CdSe wurtzite and zinc blende seeds of spherical shape with CdS material, results in spherical core/shell particles following isotropic coating, while anisotropic coating by selective blocking of the (100) facet results in rodlike structures for wurtzite and tetrapod structures for zinc blende seeds.[17]

Quasi-seeded growth

A special case of the seeded growth mechanism is the so called *quasi-seeded growth*, whereby the nucleation event is mediated by a cation exchange. Therefore, nuclei, which are different than the required material, are formed *in situ* and which are subsequently converted by ion exchange processes into the desired material. The mechanism is schematically shown in fig. 2.5.[18]

The driving force for the nucleation of the *quasi*-seeds is a higher reactivity of the precursors. Thus the *quasi*-seed precursor species should significantly increase the nucleation rate of the required material. Following the classical crystallization theory, the rate of nucleation is defined as

$$\frac{dc_N}{dt} = K_1 \cdot exp\left(-\frac{16\pi\gamma^3 {V_m}^2}{3kT\,(\mu_c-\mu_s)^2}\right) \qquad (2.15)$$

With c_N the nuclei concentration and a constant K_1. K_1 includes three sets of parameters: i) an interval or deviation around the critical radius within equation 2.1; ii) the frequency of the monomer attachment to the critical nuclei (independent of nuclei size); and iii) the concentration of the nuclei. In comparison to the second term in this equation it is very insensitive to the supersaturation and can be accepted to be a constant.[6a]

Under consideration of the chemical potentials of the solution and the crystal phase, the logarithmic expression of equation 2.16 evinces an inverse proportionality of the nucleation rate and the concentration, i.e. of the *quasi*-seed precursor[20a]:

$$\ln\left(\frac{dc_N}{dt}\right) = \ln(K_1) - \frac{16\pi\gamma^3 {V_m}^2}{3kT\left(\ln\left(\frac{c_C}{c_S}\right)\right)^2} \qquad (2.16)$$

Using this equation, the dependency of the nucleation rate on the precursor concentration can be used to prove, if a reaction follows the *quasi*-seeded growth mechanism.[6a, 18]

The subsequent cation exchange is driven by differences in the solubility products of the two materials used. Therefore, the solubility product of the desired material should be smaller than that of the *quasi*-seed material. Additionally, it is shown that these exchange reactions are reversible, thus the argument concerning the solubility products does not hold entirely, but effects of an excess ion concentration need to be taken into account. As the *quasi*-seed species is usually used in catalytic amounts up to 10%, in relation to the concentration of the intended material, the exchange reaction can be reinforced by increasing the ion flux towards the exchange interface.[19] Furthermore, considering these cation exchanges as solid-state reactions, the size of the nuclei is far below the width of the reaction zone, which is expected to be 4 to 5 nm in bulk material. In addition, a large increase of the diffusion rates is evinced, considering the high surface-to-volume ratio in nanocrystals and increasing vibrational amplitudes of surface atoms.[18, 20]

Furthermore, the extraction of the *quasi*-seed ions can be driven by a combinatorial use of precursors and complexing agents. Within the synthesis of soft Lewis acid chalcogenides (i.e. CdSe, PbSe) the cation exchange can be strengthened following the theory of Pearson concerning *hard & soft acids & bases*. Therefore, the use of hard Lewis acids as *quasi*-seeds (i.e. Sn^{2+}, Li^{1+}, Ca^{2+}) and nitrogen or phosphorus containing complexing agents as hard bases (i.e. hexadecylamine, trioctylphosphine) are required.[18, 20b, 21]

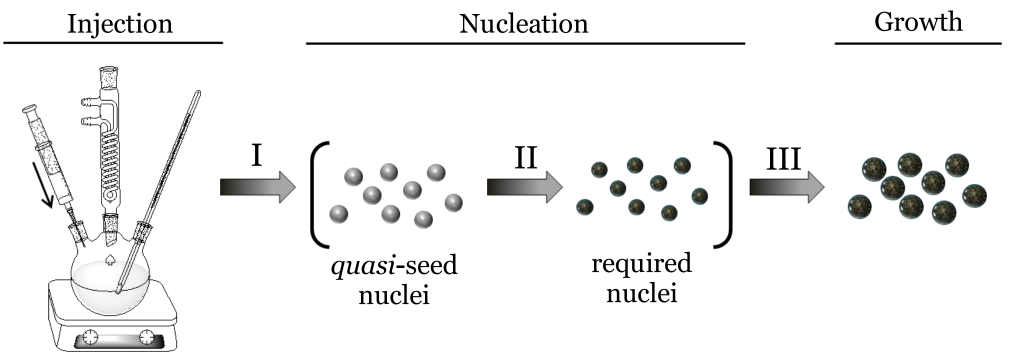

Figure 2. 5: Illustration of the *quasi*-seeded growth approach.
After injection, nuclei of the *quasi*-seed material are formed (stage I), which subsequently undergo a cation exchange to the required material (stage II). Without incorporation of the *quasi*-seed material or alloy formation the desired material grows to larger crystals (stage III).

2.3. Core/shell heterostructures

Many applications have strict requirements as to the properties of the nanoparticulate materials. As the electronic and thus optical properties are determined by the inorganic material, the outer layer defines the solubility properties (cf. fig. 2.6). As particles derived from a hot injection synthesis are only soluble within organic solvents, the outer shell needs to be modified to achieve a degree of hydrophilicity, i.e. for biological applications. This is possible by considering post synthetic ligand exchange or encapsulation into polymers or micelles.[22] However, nanoheterostructures formed via seeded growth approaches have an inner shell (cf. fig. 2.6) which consists of an inorganic material and influences the electronic properties as well as addresses a number of drawbacks of the core material. According to the high sensitivity of the bare core material towards defects and uneven passivation, non-radiative or competitive pathways are introduced due to trap states whose energies are located within the band gap of the core QDs. As a result the charge carriers may be localized in these traps and hence photoluminescence quenching or emission from these surface states occurs.[23] Furthermore, a phenomenon that is still the subject of investigation is the so called blinking effect. This intermittency of the fluorescence can be understood as a random *on* and *off* behavior during continuous excitation. Within intensity modulated excitation experiments it is found that the duration of the *on* state scales inversely with the excitation intensity. Thus the non-radiative *off* period is suggested to be generated while the crystal is excited.[23b]

Mechanistic examinations of the blinking phenomenon involve a second excitation of already excited nanocrystals. Subsequent Auger annihilation of those non-

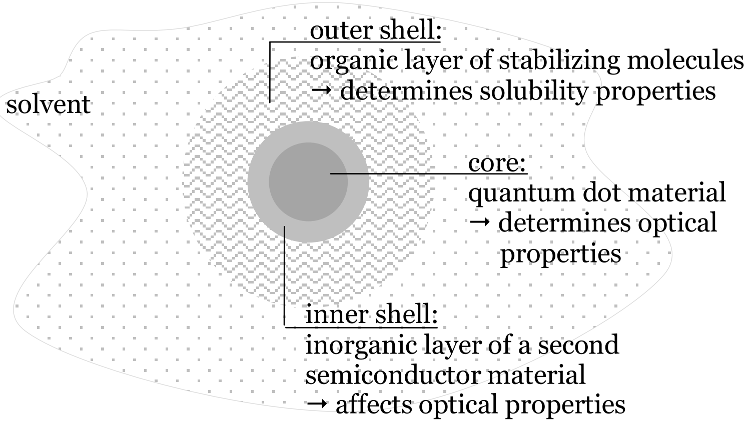

Figure 2. 6: Model of a core/shell QD in a solvent droplet.
The core material is illustrated with an inorganic layer and the organic capping as inner and outer shell, respectively. The dimensions are not drawn to scale. In the following chapters, the outer shell is termed *organic layer* and the inner shell as *shell*, *inorganic shell* or *shell material*.

equilibrated excitons leads to photoionization of the particles and hence non-radiative decay rates are enhanced.[24]

The possibility to reduce defects by an inorganic coating brings into question how one may achieve a proper surface passivation of the crystals. Important for a successful and complete surface passivation is that the core and shell materials should possess similar crystal structures with a small mismatch of the lattice constants, otherwise additional defects may be introduced or an inadequate coating achieved. Additionally, besides decreasing surface defects by the saturation of dangling bonds, intrinsic defects can be reduced by the coating process as it usually requires temperatures above 180°C. These temperatures induce diffusion processes within the core material and thus self-healing effects occur.

The electronic properties of the overall material are affected by the shell material. Thus, mainly two types of combinations are possible. As depicted in fig. 2.7, type I semiconductor materials are those containing a wider band gap material as shell, resulting in a confinement of the charge carriers within the core material, or vice versa (not schemed in fig. 2.7). Examples of type I structures are CdSe or CdTe particles coated with CdS or ZnS shells. On the other hand, type II combinations utilize semiconductors with band gaps those valence and conduction band positions are shifted against each other, e.g. CdSe on top of CdTe or vice versa. This results in a separation of the charge carriers and a recombination at the band gap offset with a red shifted photoluminescence.

Furthermore, gradated band alignments are known to possess increased optical qualities.[14b, 24d, 25] One possibility to achieve this is by the enhancement of the aforementioned intrinsic diffusion processes by increasing the temperature. Another possibility is to experimentally determine compositional mixtures of the deposited material that can be utilized for each coating layer, resulting in gradually alloyed particles as outlined below.

$$CdSe/Cd_{1-x_i}Zn_{x_i}Se_{1-y_i}S_{y_i}/ZnS$$

With the mole fraction (x, y) increasing with the number of shells (i).

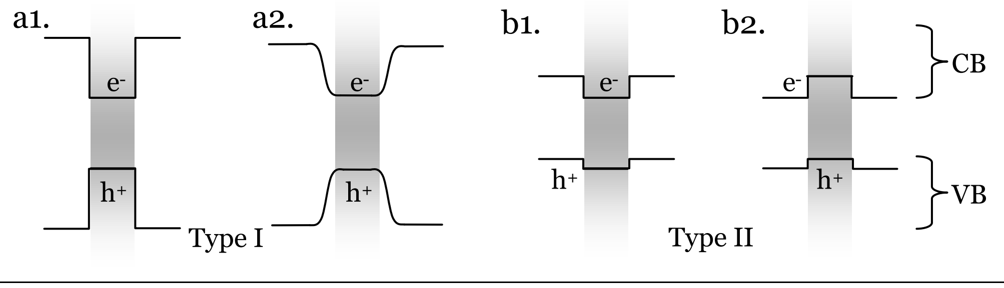

Figure 2. 7: Types of core/shell nanoheterostructures.
Type I represents the confinement of the charge carriers within the core material (grey field) with sharp (a1) and gradated band alignment (a2), while type II possesses charge carrier separation. Depending on the material arrangement in type II structures either the electron (b1) or the hole (b2) are confined within the core and the associated charge carriers within the shell.

2.4. References

[1] C. B. Murray, D. J. Norris, et al., *Journal of the American Chemical Society* **1993**, *115*, 8706.

[2] a) K. Yu, M. Z. Hu, et al., *The Journal of Physical Chemistry C* **2010**, *114*, 3329; b) Z.-J. Jiang, D. F. Kelley, *ACS Nano* **2010**, *4*, 1561.

[3] a) Z. Tang, N. A. Kotov, et al., *Science* **2002**, *297*, 237; b) M. Ethayaraja, R. Bandyopadhyaya, *Langmuir* **2007**, *23*, 6418; c) P. Dagtepe, V. Chikan, et al., *The Journal of Physical Chemistry C* **2007**, *111*, 14977; d) H. S. Chen, R. V. Kumar, *Crystal Growth & Design* **2009**, *9*, 4235; e) S. Sengupta, D. D. Sarma, et al., *Journal of Materials Chemistry* **2011**, *21*, 11585.

[4] M. Zanella, A. Z. Abbasi, et al., *The Journal of Physical Chemistry C* **2010**, *114*, 6205.

[5] D. Pan, X. Ji, et al., *Chemistry of Materials* **2008**, *20*, 3560.

[6] a) I. V. Markov, *Crystal Growth for Beginners*, 2nd ed., World Scientific, Singapore, **2003**; b) S. Kudera, L. Carbone, et al., (Ed.: A. L. Rogach), *Semiconductor Nanocrystal Quantum Dots*, Springer Vienna, **2008**, pp. 1.

[7] C. de Mello Donegá, P. Liljeroth, et al., *Small* **2005**, *1*, 1152.

[8] J. van Embden, J. E. Sader, et al., *The Journal of Physical Chemistry C* **2009**, *113*, 16342.

[9] T. Sugimoto, *Advances in Colloid and Interface Science* **1987**, *28*, 65.

[10] a) X. Peng, J. Wickham, et al., *Journal of the American Chemical Society* **1998**, *120*, 5343; b) Y. Chen, E. Johnson, et al., *Journal of the American Chemical Society* **2007**, *129*, 10937.

[11] J. Y. Rempel, M. G. Bawendi, et al., *Journal of the American Chemical Society* **2009**, *131*, 4479.

[12] a) M. D. Clark, S. K. Kumar, et al., *Nano Letters* **2011**, *11*, 1976; b) N. V. Mantzaris, *Chemical Engineering Science* **2005**, *60*, 4749.

[13] a) C. Wagner, *Zeitschrift für Elektrochemie, Berichte der Bunsengesellschaft für physikalische Chemie* **1961**, *65*, 581; b) P. Reiss, (Ed.: A. L. Rogach), *Semiconductor Nanocrystal Quantum Dots*, Springer Vienna, **2008**, pp. 35.

[14] a) E. V. Shevchenko, D. V. Talapin, et al., *Journal of the American Chemical Society* **2003**, *125*, 9090; b) S. K. Panda, S. G. Hickey, et al., *Journal of Materials Chemistry* **2011**, *21*, 11550.

[15] V. K. LaMer, R. H. Dinegar, *Journal of the American Chemical Society* **1950**, *72*, 4847.

[16] Y.-w. Jun, J.-s. Choi, et al., *Angewandte Chemie International Edition* **2006**, *45*, 3414.

[17] a) D. V. Talapin, A. L. Rogach, et al., *Nano Letters* **2001**, *1*, 207; b) D. V. Talapin, J. H. Nelson, et al., *Nano Letters* **2007**, *7*, 2951.

[18] M. V. Kovalenko, D. V. Talapin, et al., *Angewandte Chemie International Edition* **2008**, *47*, 3029.

[19] M. Ethayaraja, R. Bandyopadhyaya, *Industrial & Engineering Chemistry Research* **2008**, *47*, 5982.

[20] a) L. Dloczik, R. Könenkamp, *Nano Letters* **2003**, *3*, 651; b) D. H. Son, S. M. Hughes, et al., *Science* **2004**, *306*, 1009; c) W. Zhu, W. Wang, et al., *The Journal of Physical Chemistry B* **2006**, *110*, 9785.

[21] a) R. G. Pearson, *Journal of the American Chemical Society* **1963**, *85*, 3533; b) P. H. C. Camargo, Y. H. Lee, et al., *Langmuir* **2007**, *23*, 2985.

[22] a) W. K. Bae, K. Char, et al., *Chemistry of Materials* **2008**, *20*, 531; b) A. Sukhanova, L. Venteo, et al., *Laboratory Investigation* **2002**, *82*, 1259; c) H. Soo Choi, W. Liu, et al., *Nature Biotechnology* **2007**, *25*, 1165; d) V. V. Breus, C. D. Heyes, et al., *ACS Nano* **2009**, *3*, 2573; e) A. Dubavik, V. Lesnyak, et al., *The Journal of Physical Chemistry C* **2009**, *113*, 4748; f) B. Dubertret, P. Skourides, et al., *Science* **2002**, *298*, 1759.

[23] a) M. Kuno, J. K. Lee, et al.*, Vol. 106*, American Institute of Physics (AIP), **1997**, pp. 9869; b) M. Nirmal, L. Brus, *Accounts of Chemical Research* **1998**, *32*, 407; c) S. Sapra, S. Mayilo, et al., *Advanced Materials* **2007**, *19*, 569.

[24] a) D. I. Chepic, A. L. Efros, et al., *Journal of Luminescence* **1990**, *47*, 113; b) M. Nirmal, B. O. Dabbousi, et al., *Nature* **1996**, *383*, 802; c) A. L. Efros, M. Rosen, *Physical Review Letters* **1997**, *78*, 1110; d) X. Wang, X. Ren, et al., *Nature* **2009**, *459*, 686.

[25] D. Dorfs, T. Franzl, et al., *Small* **2008**, *4*, 1148.

3

Thermodynamic aspects of the nucleation of CdSe QDs

Quasi-seeded growth approach

3.1. Introduction

For the consideration of the thermodynamic aspects of a hot injection synthesis the thermodynamic stability of precursor species, nuclei or particles must be taken into account. In accordance with the proposed general reaction mechanism for a hot injection synthesis, during the injection the precursors become thermodynamically unstable and start to form the monomers, which further react to nuclei. These nuclei are considered to be thermodynamically unstable as they exhibit the highest Gibbs free energy, as depicted in fig. 2.2. Fulfilling the criteria of eq. 2.1 and 2.2 the nuclei may grow by decreasing their Gibbs free energy. Therefore, the nuclei have to possess a size similar to the critical radius and a chemical potential for the crystals smaller than that of free monomers is required. The stability of the resulting particles obtained from nuclei growth is described by the Gibbs-Thomson theory given in eq. 2.8 by means of size dependent solubility of the compounds.

As the solubility product of a compound is related to its precursor concentration, one possibility to thermodynamically influence the nucleation is to add a second cation species. Those *quasi*-seed precursors need to exhibit a higher reactivity, or lower thermodynamic stability. Additionally the formed nuclei must have a larger solubility product to enable the possibility of a cation exchange reaction towards the intended material. A second possibility to initiate the cation exchange is the use of catalytic amounts of the *quasi*-seed species. Following this, the excess concentration of the intended material increases the flux of ions towards the interface where the exchange occurs and thus the process is favored.[1] This allows materials with similar or lower solubility products to be used.

First experimental results on partial ion substitution were obtained for core/shell quantum dots of CdS/ZnS and CdS/PbS via *in situ* and post synthetic approaches.[2] Son et al. extended these findings to exchange reactions of entire nanocrystals and Kovalenko et al. found the possibility to use the *quasi*-seeded growth for the synthesis of PbSe nanocrystals catalyzed by $[(Me_3Si)_2N]_2Sn$.[3]

These considerations of the cation exchange-mediated nucleation will be applied here for the system of CdSe quantum dots using SnSe as *quasi*-seeds. Within these investigations the applicability of the *quasi*-seed mechanism is to be shown and the reaction conditions optimized. The main goal is the implementation of this *quasi*-seeded growth (qsg) approach for a laboratory batch up-scaling for the synthesis of CdSe quantum dots.

3.2. Synthesis optimization applying the *quasi*-seeded growth approach

The standard synthesis of CdSe nanoparticles involves long chained amines and phosphine oxides, in particular hexadecylamine (HDA) and *n*-trioctylphosphine oxide (TOPO). As described by the theory of Pearson for *hard & soft acids & bases*, cadmium is a soft Lewis acid while HDA and TOPO are hard.[4] Therefore, a hard Lewis acid is chosen to encourage the cation exchange. Hence, Sn^{2+} twice coordinated by trimethylsilylamide, as used by Kovalenko et al., is a prime candidate.[3b]

Applying 5% of bis[bis(trimethylsilyl)amino] tin(II), $[(Me_3Si)_2N]_2Sn$ to the synthesis of CdSe quantum dots, a significant improvement in the optical spectra is obtained. As presented in fig. 3.1, more distinct excitonic transitions may be seen within the absorption spectra recorded following the *quasi*-seeded growth (qsg) approach in comparison to the standard hot injection (hi) method. These findings are attributed to a narrower size distribution which results in a better separation of the transitions within the absorption spectra as well as a smaller full width at half maximum (fwhm) of the photoluminescence (PL) peak. Additionally, in comparison to the standard hot injection method the reproducibility of the synthesis is improved.

For further investigations, progression aliquots were taken at given time intervals during the reaction and characterized using absorption and emission spectroscopy. As a result of the obtained data the particle sizes and their corresponding concentrations could be calculated. The sizes are calculated from the wavelength position of first absorbance maxima using an empirical formula by Yu et al. (see eq. B.2 in Appendix B), whereas QD concentrations are calculated by a method established by de Mello Donegá et al.[5] This method is based on the bulk absorption

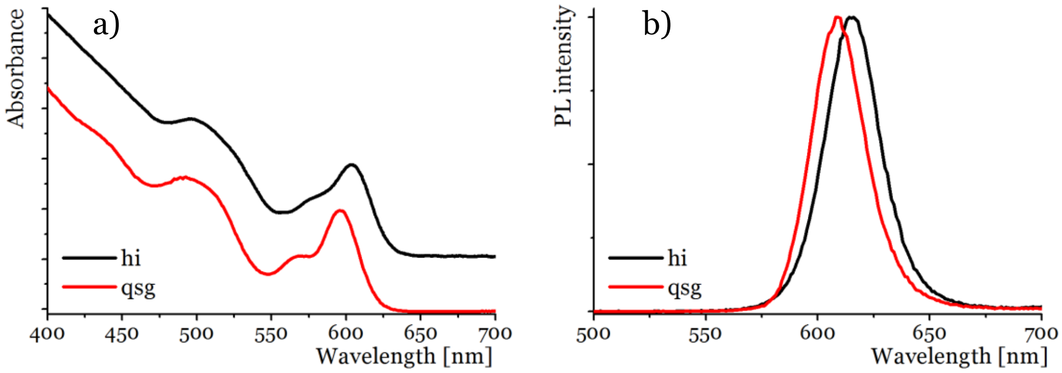

Figure 3. 1: CdSe quantum dots prepared via the *quasi*-seeded growth (qsg) approach result in optical spectra (Abs: a, PL: b) of improved quality, with respect to their size distribution, in comparison to the standard hot injection method (hi).

behavior of the quantum dots at the high energy end of the absorption spectra. Thus the absorbance at a wavelength of 400 nm is used to calculate the molar extinction coefficient (eq. 3.1). Finally the QD concentration is obtained using the law of Lambert-Beer (eq. 3.2).

$$\varepsilon_{3.1eV} = 5.8\cdot 10^{-18}\cdot N_A\cdot z\cdot \frac{\langle V_{QD}\rangle}{V_{UC}}\cdot\frac{1}{2303} = 1.52\cdot 10^{3}\cdot\frac{z\cdot\langle V_{QD}\rangle}{V_{UC}} \qquad (3.\,1)$$

With $\varepsilon_{3.1eV}$ the molar extinction coefficient at an absorbance of 3.1 eV (400 nm) (in M^{-1} cm^{-1}), N_A Avogadro's number, z the number of unit ion pairs per unit cell (for zinc blende z is 4), $\langle V_{QD}\rangle$ the mean particle volume (assuming spherical particles $\langle V_{QD}\rangle = \frac{4}{3}\cdot\pi\cdot r^3$), and V_{UC} the volume of the unit cell (given as $V_{UC} = 2.723\cdot 10^{-22}\,cm^3$ for CdSe).

$$Abs_{3.1eV} = \varepsilon_{3.1eV}\cdot\langle c_{QD}\rangle\cdot L \qquad (3.\,2)$$

With $Abs_{3.1eV}$ the absorbance at 3.1 eV (400 nm), $\langle c_{QD}\rangle$ the mean QD concentration, and L the path length of light in the cuvette (given as 1 cm).

As shown in fig. 3.2 a, the particles obtained by the *quasi*-seeded growth approach possess sizes smaller than those derived from standard hot injection. This finding is plausible and underpins the qsg mechanism: as the $[(Me_3Si)_2N]_2Sn$ is the more reactive precursor in comparison to the $Cd(oleate)_2$, it is able to affect the nucleation

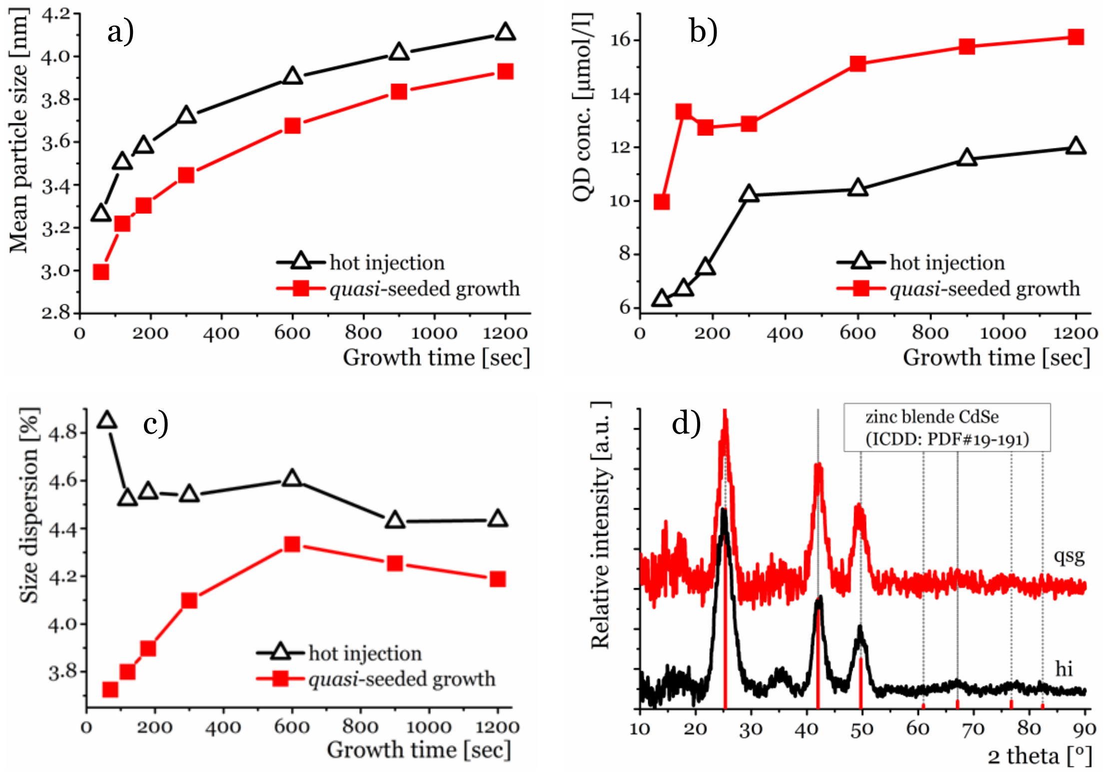

Figure 3. 2: CdSe QDs obtained utilizing the qsg approach result (a) in a smaller final particle size with (b) increased particle concentrations and (c) narrower size dispersion. d) The zinc-blende crystal structure remains uneffected.
For comparison the theoretical pattern of bulk zinc blende CdSe is shown as reference.

by increasing the number of nuclei and hence of the obtained QDs, as shown in fig. 3.2 b. This may be seen from the narrowing of the size dispersion or distribution, as this is an indication for an improved synthesis. Experimentally this may be derived from the full width at half maximum of the first absorbance maximum and can be calculated assuming a Gaussian distribution.[6] Accordingly, fig. 3.2 c shows that an improvement over the standard hot injection synthesis in terms of narrower size dispersions can be achieved by the use of catalytic amounts of $[(Me_3Si)_2N)_2Sn$. In addition, experimentally it is shown that the crystal structure of the QDs influences the absorption spectra, which is explained by means of an impact on the exciton fine structure by the crystal field.[7] As the quantum dots obtained by both synthesis methods exhibit the same crystal structure (cf. fig. 3.2 d), differences in the absorption spectra due to different crystal structures can be excluded.

Following these results, the mechanism of the *quasi*-seeded growth approach is to be sufficiently proofed.

3.3. Proof of the reaction mechanism

The use of catalytic amounts tin(II) silylamide significantly improves the quality of the resulting CdSe QDs. Ensuring the catalytic character of the tin species following the *quasi*-seeded growth approach, further investigations were required.

i. Preliminary control experiments

Initially, preliminary control experiments had to be undertaken as recently Yarema et al. postulated a different reaction mechanism which included the tin silylamide precursor within a synthesis for silver chalcogenides in oleylamine and *n*-trioctylphosphine. The mechanism is proposed to proceed via the conversion of Ag silylamide to elemental silver with a subsequent reaction by chalcogenides to form the desired nanoparticles. In addition, they applied this mechanism to the synthesis of CdSe and CdTe quantum dots.[8] Furthermore, this mechanism coincides with a second procedure, wherein high-quality CdTe quantum dots are synthesized via the formation of intermediate elemental cadmium.[9] Osovsky et al. attributed the presence of a monomer reservoir to this Cd^0 species, as a way of balancing the cadmium oleate concentration while the reaction proceeds.

Therefore, control experiments were performed by means of thermal decomposition of the precursors without the presence of the chalcogenide, similar to the suggestion by Yarema et al. for the synthesis of Ag_2Se. Within these investigations in the presence as well as the absence of $[(Me_3Si)_2N]_2Sn$, the reaction solution turned grayish and cloudy within a few minutes. The obtained particles were collected and

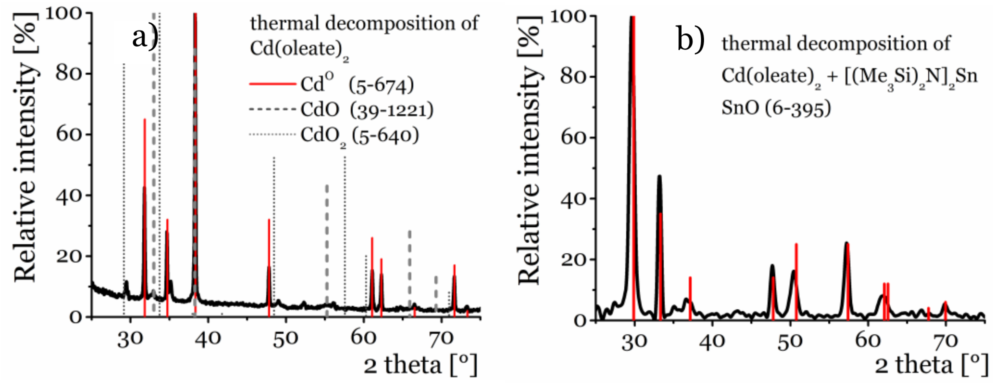

Figure 3. 3: Precipitated products after thermal decomposition of $Cd(oleate)_2$ in absence (a) and presence of $[(Me_3Si)_2N]_2Sn$ (b) which result in Cd^0 and SnO, respectively.

The theoretical patterns of the associated compounds are shown as red lines. Additional theoretical patterns are shown in (a) to explain further reflexes (dashed and dotted black line).

characterized by powder x-ray diffraction. As depicted in fig. 3.3, in the absence of tin silylamide Cd^0 is obtained (besides small amounts of CdO and CdO_2), whereas in its presence phase pure tin(II) oxide is found.

The observation of Cd^0 is in agreement with Osovsky and Kloper,[9] whereas the formation of cadmium oxides is contradictory to the proposed mechanism. An additional nonconformity regarding the mechanism proposed by Yarema et al.[8] is suggested due to the obtained SnO. The origin of the oxygen source in both cases is the formation of peptide bonds between oleic acid and hexadecylamine resulting in a release of water. Further experiments regarding the peptide formation and release of water were undertaken including a further cleaning step before the injection of $[(Me_3Si)_2N]_2Sn$. Therefore, after evacuation of the reaction mixture at 100°C, the temperature is raised to 250°C under argon atmosphere and kept there for at least 40 to 50 minutes. Afterwards, this mixture is allowed to cool to 100°C and subsequently vacuum is applied for 30 minutes to remove any residual amounts of water present. After this step the tin(II) precursor is introduced via a syringe. The resulting mixture showed exceptional stability at the injection temperature of 270°C and for at least 60 minutes no changes in the appearance are observed.

As a concluding remark, the addition of bis[bis(trimethylsilyl)amino] tin(II) results in the formation of SnO due to the formation of peptide bonds by insufficient purification of the reaction mixture. Nevertheless, the presence of the tin species affects the behavior of the cadmium oleate as it inhibits the formation of Cd^0. In relation to the mechanism of Yarema et al. Cd^0 is mandatory and hence the mechanism is excluded from the present synthesis. Further examinations of the reasons for the inhibited Cd^0 formation become less important, as analysis becomes difficult due to the complexity of the reaction mixture.

ii. Structural and crystallographic investigations

Transmission electron microscopy (TEM) allows investigations of the shape of the obtained quantum dots. As described by the particle-in-a-box model and applied to nanostructures, the electron wave function is confined within a potential well, the length of which is defined by the size of the particle. Therefore, the shape of nanostructures determines the three dimensional potential well of the confinement. Following on from this, quantum dots are confined in three, while quantum wires are confined only in two dimensions. Thus, variations in shape result in different widths of the potential wells and thus differences in the absorption spectra. As can be seen from the TEM images in fig. 3.3, the particles obtained by the standard hot injection method compared to those obtained by the *quasi*-seeded growth approach are both nearly spherical in shape. This implies, that the differences in the absorption spectra are not related to shape differences. However, estimating the arrangement of the particles, differences in the size distribution are obvious. A closer packed and well ordered assembly is associated with a narrower size distribution, as achieved within the *quasi*-seeded growth. This result also supports the observations in the optical profiles, as narrower size dispersions are achieved following the *quasi*-seeded growth approach.

Additionally, elemental analysis and crystallographic characterization eliminate the possibility of ion incorporation and alloying. An incorporation of tin ions into the lattice of CdSe crystals would result in a shift of the x-ray diffraction reflexes due to differences in the ion radii, as would be observed within x-ray diffraction patterns. Investigations of sample powders using x-ray diffraction, exclude any tin inclusion into the lattice, as no changes are obvious within fig. 3.2 d.

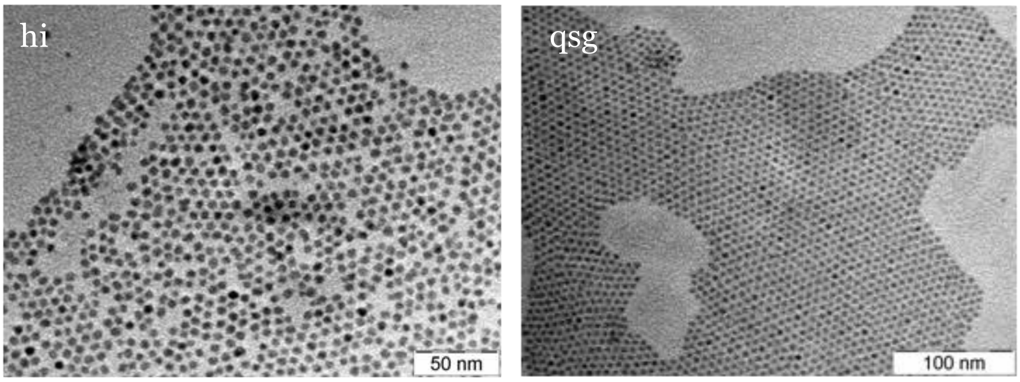

Figure 3. 4: TEM images of CdSe showing the increased monodispersity of the particles derived following the qsg approach in comparison to the standard hot injection (hi) procedure.

Table 3. 1: ICP-OES measurements of CdSe QDs prepared in the presence and the absence of 10% $[(Me_3Si)_2N]_2Sn$.

sample	analyte	mean concentration	standard deviation
CdSe	Cd 214.440	12.09 mg/l	0.257
	Sn 189.927	< LoQ (42 ppb)	1.0491
CdSe	Cd 214.440	12.18 mg/l	0.172
	Sn 189.927	< LoQ (42 ppb)	1.0059
$CdSe_{Sn}$	Cd 214.440	12.63 mg/l	0.237
	Sn 189.927	< LoQ (42 ppb)	0.675
$CdSe_{Sn}$	Cd 214.440	12.97 mg/l	0.114
	Sn 189.927	< LoQ (42 ppb)	1.3899
blank	Cd 214.440	< LoQ (1 ppb)	0.0002
	Sn 189.927	< LoQ (42 ppb)	0.366

$CdSe_{Sn}$ and CdSe denote QDs prepared in the presence and absence of 10% $[(Me_3Si)_2N]_2Sn$, respectively. Details for sample preparation are given within Appendix A. LoQ is the limit of quantification with its actual value in parenthesis.

However, doping of CdSe crystals by tin could not be detected with x-ray diffraction analysis. Therefore, multiple quantitative analyses using ICP-OES measurements have been undertaken and allow to exclude any tin incorporation or adsorption. Tab. 3.1 shows the results of ICP-OES measurements of small amounts CdSe digested in a mixture of hydrochloric and nitric acid. As a blank value, a dilution of the pure acids is used. The outcome of these investigations is that Sn^{2+} is not detectable within the limit of quantification and thus may be considered as absent within these samples.

iii. Influence on the nucleation

a) Indication by magic-sized clusters

A further proof of the validity of the *quasi*-seeded growth mechanism is an investigation of magic-sized clusters (MSCs). As will be shown in chapter 4, MSCs may occur within the synthesis of CdTe nanoparticles and thus a CdTe synthesis is used for this examination. Here the CdTe is used, because in any of the investigated CdSe synthesis no magic-sized clusters are observed. Magic-sized clusters are denoted as a kind of molecular like particles which are formed during the nucleation and exhibit a high degree of thermodynamic stability.[10] Although they are relatively inert towards monomer deposition, within the applied synthesis discontinuous

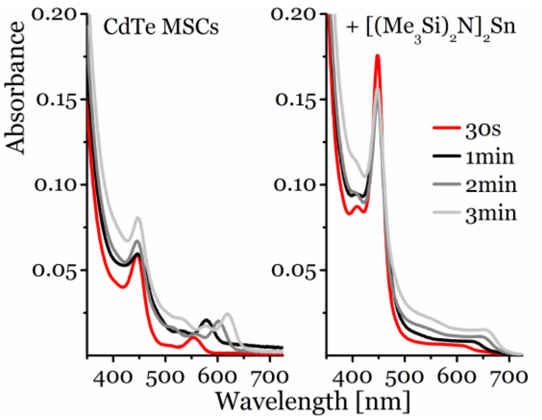

Figure 3. 5: Application of the qsg approach in the synthesis of CdTe QDs increases the number of magic-sized clusters and is therefore attributed to affect the nucleation.

growth of the MSCs is not obtained, but at a certain point during the growth stage the MSCs exhibit sizes smaller than the critical radius and start to dissolve and disappear. The most prominent feature of these MSCs is a very narrow and intense absorbance. The origin of this feature is ascribed to the nature of these clusters as they are considered as closed shell species with a defined number of atoms. Accordingly a single MSC family exhibits one size. Consequently, MSCs are easily detectable by optical spectroscopy and thus constitute good indicators for the reaction progression at the nucleation stage and any subsequent effects on it. Examining fig. 3.5 the concentration of magic-sized clusters with an absorbance at 445 nm is significantly increasing, if 5% of $[(Me_3Si)_2N]_2Sn$ is introduced to the synthesis of CdTe QDs. This can be adequately explained using the main ideas of the *quasi*-seeded growth mechanism: *quasi*-seeds nucleate more rapidly, undergo an instantaneous and entire cation exchange and hence an increased number of nuclei results. Additionally, MSC formation is considered to be involved in the nucleation but not the growth process[10], thus these results show that *quasi*-seeds can be used to influence the nucleation event.

b) Dependence on the nucleation rate

The degree of impact of the *quasi*-seed precursors on the nucleation event can be evaluated by investigation of the nucleation rate, as it is predicted to determine the number of nuclei and thus the size of the resulting particles. The dependence of nucleation rate $\frac{dc_N}{dt}$ on the precursor concentration as given within the framework of classical nucleation (cf. eq. 2.15 and 2.16):

$$ln\left(\frac{dc_N}{dt}\right) = ln(K_1) - A \cdot ln\left(\frac{c_c}{c_s}\right)^{-2} \tag{3. 3}$$

Herein, K_1 as a constant and $A = 16\pi\gamma^3 V_m^2 \cdot (3kT)^{-1}$.

Experimentally it is shown that the nucleation rate, investigated for different initial precursor concentrations, is inversely proportional to the final mean particle size.[11]

$$\frac{dc_N}{dt} \propto \frac{1}{r} \tag{3. 4}$$

In combination with eq. 2.12 the relation between the mean particle size r and the concentration of the *quasi*-seed precursor c_{qs} can be expressed as follows.

$$ln(r^{-1}) \propto \left(ln(c_{qs})\right)^{-2} \tag{3. 5}$$

Experimentally, the *quasi*-seeded growth is investigated using $[(Me_3Si)_2N]_2Sn$ concentrations in the range of 4 to 200 µmol (equal to 1 to 50% Sn^{2+} with respect to the amount of Cd^{2+}). Within experimental errors a linear behavior between *quasi*-seed concentration and mean particle size is obtained as predicted by eq. 3.5. Deviations are obtained for the highest and the lowest Sn^{2+} concentration, as

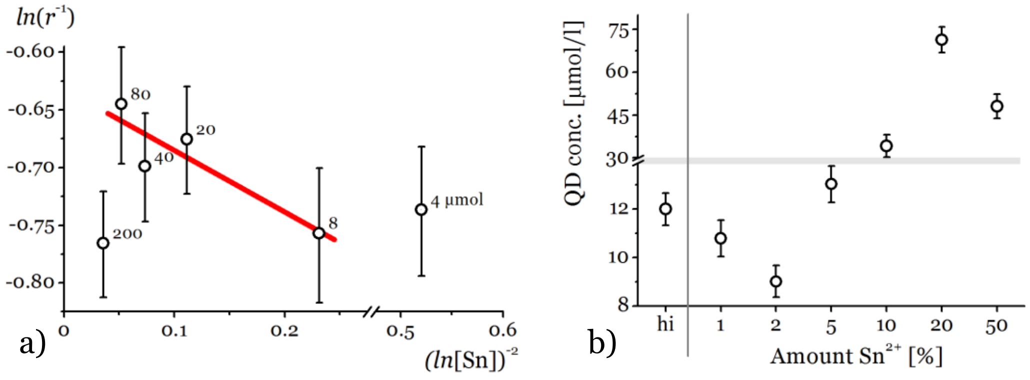

Figure 3. 6: Increasing concentrations of the *quasi*-seed species, [Sn], (a) decrease the final particle size, r and (b) increase the QD concentration.
The error bars derive from the size dispersion. The red line indicates the linear relationship according to eq. 3.2. QD concentrations are calculated using the method described according to eq. 3.1 and 3.2.

presented in fig. 3.6 a. Reasons for these deviations are a parallel nucleation of CdSe within the 1% study and a disturbed or retarded cation exchange reaction within the 50% study. Thus competing processes may occur, influencing the growth kinetics. Further evidence for an increased nucleation rate gives the number of resulting QDs. As the concentration of the most reactive species (here $[(Me_3Si)_2N]_2Sn$) within the reaction increases, the number of particles should also increase. This is confirmed from fig. 3.6 b: the higher the Sn^{2+} concentration becomes the greater the increase in the QD concentration.

In summary, as indicated by the appearance of magic-sized clusters it is shown that the nucleation event is influenced by the *quasi*-seed species. Additionally, the effects on the nucleation rate are enhanced with increasing *quasi*-seed concentration within a certain range. Consequently, with respect to these observations, the mechanism of the *quasi*-seeded growth may be said to be applicable for the present reaction and moreover has been optimized to obtain the most efficient *quasi*-seed concentration.

3.4. Optimization by means of *quasi*-seed concentration

To optimize the system, the mean particle sizes as well as the size dispersions are calculated, following the implementations above. In addition to this, the photoluminescence quantum yields are calculated with respect to Rhodamine 6G following standard protocols.[12] Finally, the importance of the nature of the *quasi*-seed precursor is examined by use of different *quasi*-seed precursors, related to the cation itself or the coordinating molecules.

In order to achieve this, aliquots are taken from the reaction across a certain time range and characterized using spectroscopic methods.

i. Growth kinetics

A synthesis optimization by means of varying the *quasi*-seed concentration is investigated by applying the *quasi*-seed precursor $[(Me_3Si)_2N]_2Sn$ in concentrations ranging from 4 to 200 µmol. This correlates to a molar amount of Sn^{2+} with respect to Cd^{2+} ranging from 1 to 50%. Finally, the results are compared to the standard hot injection synthesis.

The results are plotted as size and size dispersion as a function of the growth time and given in figs. 3.7 and 3.8 respectively. As seen from these results, particles obtained using tin concentrations of 1 and 2% (figs. 3.7 a and 3.8 a) possess larger sizes than those obtained from the standard hot injection. As already mentioned a

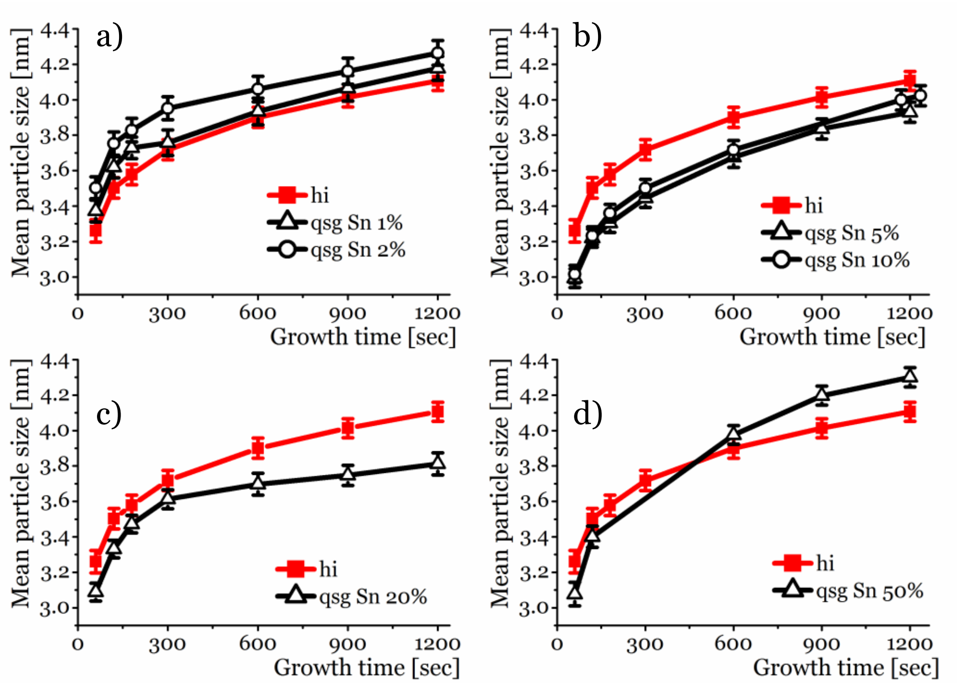

Figure 3. 7: Applying different quasi-seed concentrations smaller particle sizes than for the standard hot injection method derive from 5-20%, whereas lower or higher amounts result in larger sizes.

Various $[(Me_3Si)_2N]_2Sn$ concentrations (black, open symbols) in comparison to the standard hot injection method (red, filled symbols).

reason for this could be a parallel nucleation of SnSe and CdSe due to the low Sn^{2+} concentration. Consequently, two kinds of CdSe particles grow within the synthesis, those derived from cation exchange-mediated nucleation and those from homogeneous nucleation. Subsequently, the size distribution exceeds that of the standard hot injection synthesis and thus the synthesis results in a wider size distribution. The second extreme is represented by the highest Sn^{2+} concentration of 200 µmol (50%, figs. 3.7 d and 3.8 d). Applying this amount of *quasi*-seed species within the synthesis, first smaller sizes are obtained but whose sizes later on exceed those of the standard hot injection method. These observations are associated with decreasing and increasing size distributions, respectively. A possible reason for a retarded or disturbed cation exchange is assumed to be due to the high Sn^{2+} concentration. Consequently in the beginning of a synthesis a narrowing of the broad size distribution occurs, whereas at a certain point ripening processes start and the size distribution broadens again, resulting in slightly larger size distributions as compared to the standard hot injection procedure. However, the cation exchange succeeds completely, as shown in tab. 3.1 within ICP-OES measurements quantitatively no Sn^{2+} was determined.

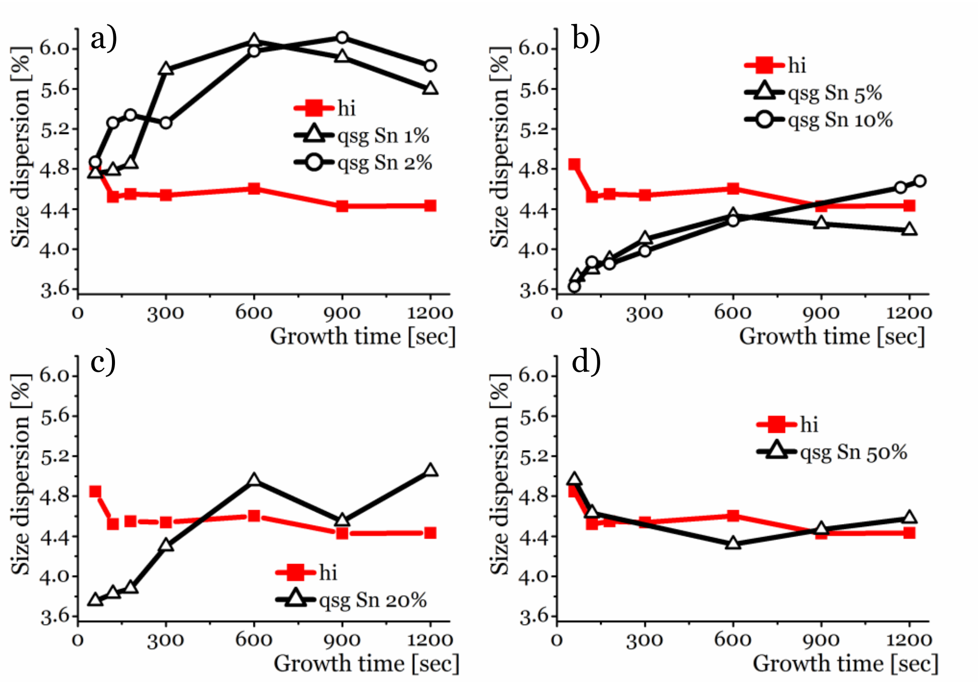

Figure 3. 8: Size dispersions as derived from Gaussian fits of the photoluminescence peaks show the narrowest values applying 5% of the tin species.
Comparison of various $[(Me_3Si)_2N]_2Sn$ concentrations (black, open symbols) to the standard hot injection method (red, filled symbols).

The smallest initial size distributions with values below 3.8% arise from tin concentrations between 5 and 20% (figs. 3.7 b,c and 3.8 b,c). This probably indicates the presence of a regime of a highly cation exchange-controlled nucleation. The subsequent growth in all these cases proceeds with a growth progression similar to that of the reference synthesis (hi), but always with smaller sizes. In contrast to the standard hot injection synthesis is the presence of the increasing size dispersions, which in principle indicates the process of Ostwald ripening. A later narrowing is achieved, only within the synthesis where 5% of tin was employed. Further support for the cation exchange-mediated nucleation and growth is provided in fig. 3.9 where the concentration of the QDs is given as function of the growth time. As nucleation and growth are controlled by *quasi*-seed formation with subsequent cation exchange, the number of QDs should be constant. For syntheses using 5 to 20% of $[(Me_3Si)_2N]_2Sn$, within experimental errors nearly constant QD concentrations are achieved. A controversial observation can be found for the use of 50% of the tin species, where the QD concentration decreases. This supports the suggestion of an occurring Ostwald ripening, which can be attended with a decrease in the particle concentration.

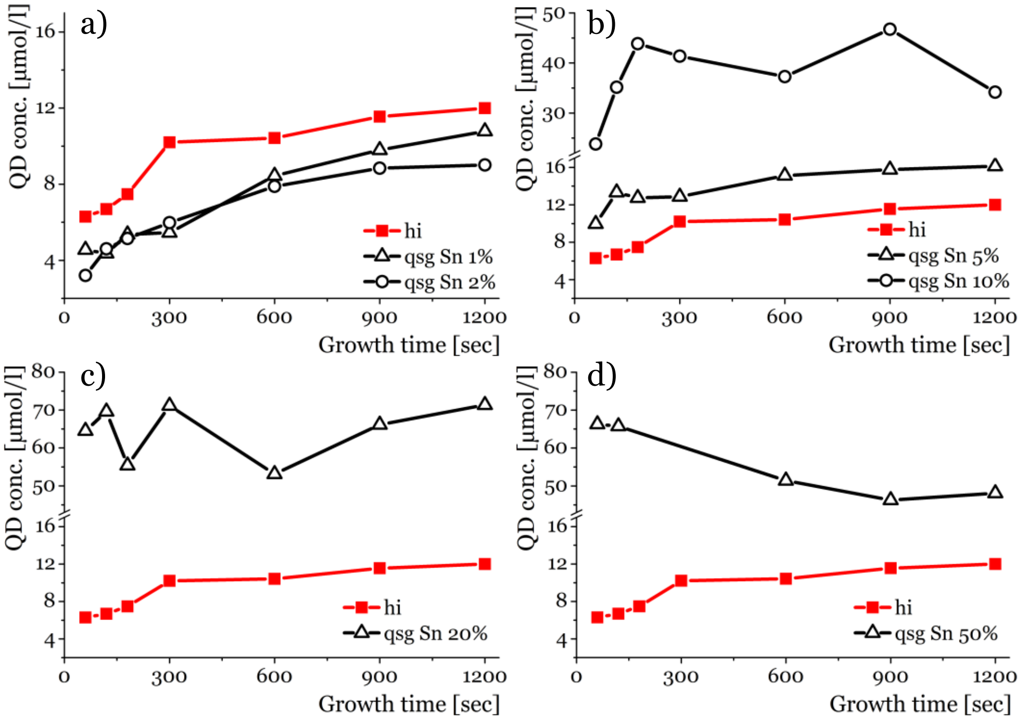

Figure 3. 9: QD concentrations increase with increasing *quasi*-seed concentrations according to the proposed mechanism.
Comparison of various $[(Me_3Si)_2N]_2Sn$ concentrations (black, open symbols) to the standard hot injection method (red, filled symbols). The QD concentration is calculated using the method described above following eq. 3.1 and 3.2.

ii. Quantum yield

A second parameter for judging the quality of obtained particles is the photoluminescence quantum yield. As the quantum yield (QY) is the ratio of emitted to absorbed photons within a QD ensemble it depends on many factors, amongst which are the electronic structure of the QDs, *off* periods within blinking effects as well as internal and surface defects of the QDs.[13] The latter is especially affected by the kinetics of crystal growth via the monomer deposition rate as well as surface coverage by stabilizing agents. Too fast a deposition rate may result in a greater concentration of internal defects and thus affect the emission properties of the material. Healing of these defects can be induced by ripening or annealing processes through the application of higher temperatures to induce diffusion processes.

Additionally, broad size distributions may also reduce the QY by means of re-absorption, whereby light emitted by smaller particles is absorbed by larger particles within the same particle ensemble. However, the latter effect is negligible as the optical density of the solutions is kept below 0.1 for the measurements.

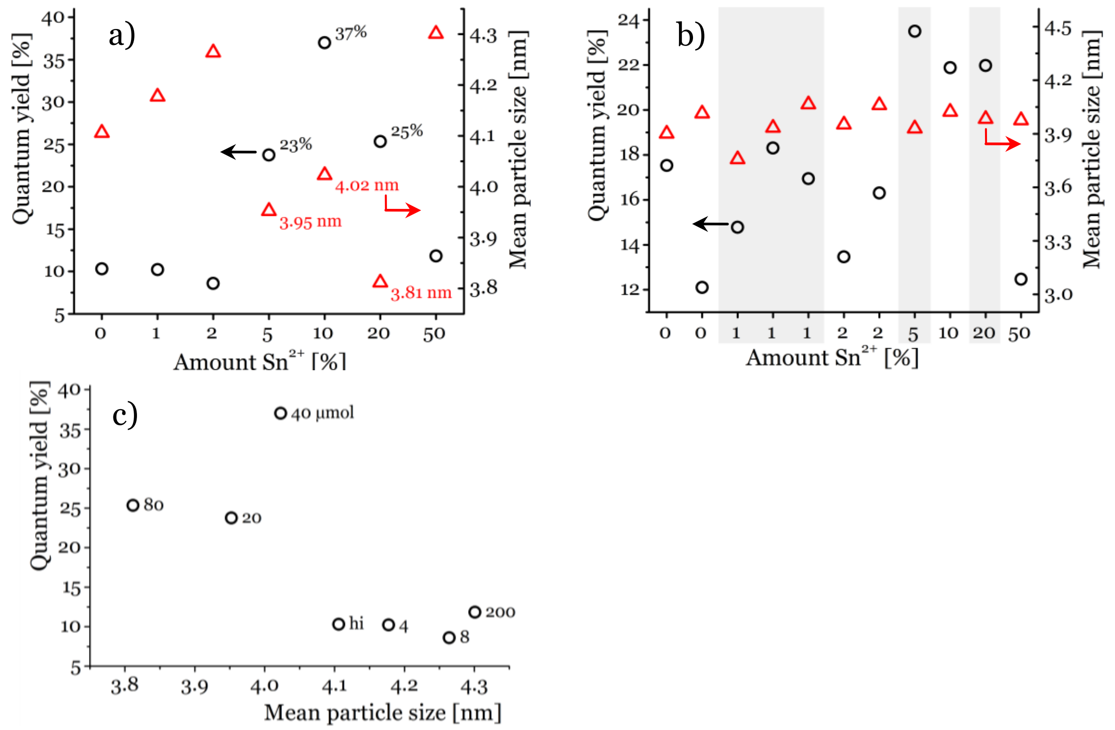

Figure 3. 10: Highest values for photoluminescence quantum yields (QY) are obtained utilizing 5 to 20% of the *quasi*-seed species.
Comparison of QY (black spheres) and mean particle size (red triangles) for different $[(Me_3Si)_2N]_2Sn$ concentrations: a) standard series investigated within this chapter, b) repeated syntheses with defined particle sizes between 3.8 and 4.2 nm. c) QY as a function of particle size with *quasi*-seed concentrations (in µmol) as label.

As is apparent in fig. 3.10 a, the highest quantum yields arise for the *quasi*- seeded growth approach using tin concentrations between 5 and 20%, with a maximum at 10%. Due to the differences in the size compared to the residual concentrations, a size dependence of the QY could be revealed (cf. fig. 3.10 c). Due to this observation, repeated syntheses were undertaken using different *quasi*-seed concentrations to obtain final particle sizes between 3.8 and 4.2 nm. The comparison of the particles obtained from these syntheses (shown in fig. 3.10 b) show the findings of the highest QYs to be for 5 to 20% of the *quasi*-seed material. An exception is the high value for 40 µmol $[(Me_3Si)_2N]_2Sn$ with a quantum yield of 37% in fig. 3.10 a (qsg Sn 10%), which could not be reproduced by the data shown in fig. 3.10 b.

iii. Summary

Following the size progression, indications for the *quasi*-seeded growth mechanism are given for Sn^{2+} concentrations from 20 up to 80 µmol (5 - 20% with respect to Cd^{2+}) as the sizes are smaller than those of particles obtained via the standard hot injection method. Below the threshold of 5%, the *quasi*-seed concentration is too low to control the nucleation via cation exchange. For concentrations around 50% difficulties in the reaction are found, which are attributed to competing processes due to the high tin concentration. However, upon investigating the size distributions, in all cases ripening processes are indicated by a slight broadening of the dispersions. In the case of the 200 µmol synthesis the occurrence of ripening processes is supported by a decrease in the particle concentration.

In this manner, increased QY values arise for reactions following the cation exchange controlled nucleation and growth mechanism (5 – 20% Sn^{2+}). Due to the presence of a narrow distribution of SnSe *quasi*-seeds and the subsequent cation exchange to CdSe, followed by the growth processes, approximately constant QD concentrations are obtained (cf. fig. 3.9). According to the slight broadening of the size dispersion (cf. fig. 3.8), ripening effects are revealed, similar to Ostwald ripening, and hence increased quantum yields are achieved presumably due to internal healing processes.

Combining these results, allows a mostly optimized synthesis regarding size and size distribution as well as quantum yield to be executed using 5% of the *quasi*-seed precursor.

3.5. Nature of the *quasi*-seed precursor

One of the main requirements for the success of the *quasi*-seeded growth approach is the high reactivity of the *quasi*-seed precursor. Hence the use of the highly reactive bis[bis(trimethylsilyl)amino] tin(II) within this approach was introduced by Kovalenko et al.[3b] This precursor species of silylamide coordinated metal is applied for many difficult to access nanoparticles, including chalcogenides of tin[11c, 14] and silver[8] as well as GeTe[15] and bare metal nanoparticles of Pb[16], Ge[15] and Bi[17].

Furthermore, within the experiments an exothermic reaction is observed when the tin silylamide is injected to the oleic acid containing solution. To further study this, defined amounts of $[(Me_3Si)_2N]_2Sn$ are added to oleic acid under argon atmosphere and the residues are removed by applying vacuum. Due to the high viscosity of the obtained solution, small amounts of 1-octadecene are added, the resulting mixture examined using FTIR spectroscopy, and the observed vibrations are assigned by

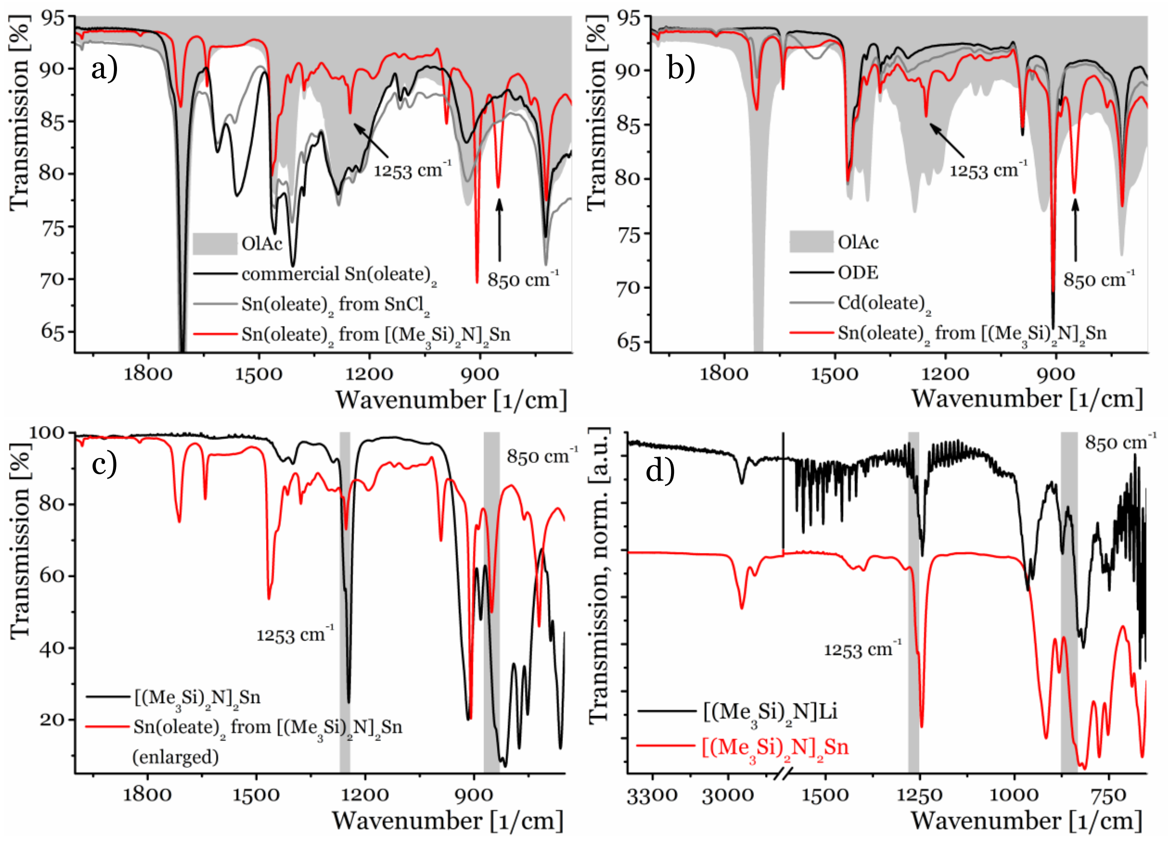

Figure 3. 11: FTIR spectra indicate features of tin oleate as well as silylamide for the structure of the *quasi*-seed tin species after reaction with oleic acid.
The *quasi*-seed tin species is denoted as $Sn(oleate)_2$ from $[(Me_3Si)_2N]_2Sn$ (red spectra). Comparison to a) oleic acid (grey area) and $Sn(oleate)_2$ from commercial sources (black line) and synthesized from $SnCl_2$ (grey line); b) oleic acid (grey area), ODE (black line) and the homologous oleate of Cd (grey line); c) $[(Me_3Si)_2N]_2Sn$ (black line) indicating the silylamide vibrations. d) Comparison of pure $[(Me_3Si)_2N]_2Sn$ (red) and $[(Me_3Si)_2N]Li$ (black). Both silylamide vibrations ($\nu_1 = 850\ cm^{-1}$, $\nu_2 = 1253\ cm^{-1}$) are present as a “shoulder”, highlighted with black arrows (a,b) and grey fields (c,d).

means of an overlay of reference data. The comparison of the obtained mixture, denoted as “$Sn(oleate)_2$ from $[(Me_3Si)_2N]_2Sn$”, with pure oleic acid, commercially available $Sn(oleate)_2$ and “$Sn(oleate)_2$ from $SnCl_2$” reveals a partial formation of $Sn(oleate)_2$ (fig. 3.11 a). Comparing the obtained FTIR spectrum with those of $Cd(oleate)_2$, a homologous oleate, as well as ODE as solvent (fig. 3.11 b), in addition to the oleate vibrations two important features ($\nu_1 = 850\ cm^{-1}$, $\nu_2 = 1253\ cm^{-1}$) remain unexplained. The direct comparison to bis[bis(trimethylsilyl)amino] tin(II) (fig. 3.11 c) assigns these vibrations to the trimethylsilylamid group as is also observed by the FTIR spectra for $[(Me_3Si)_2N]Li$ in fig. 3.11 d. In conclusion a complex coordination of the tin by oleate as well as silylamide ligands is observed.

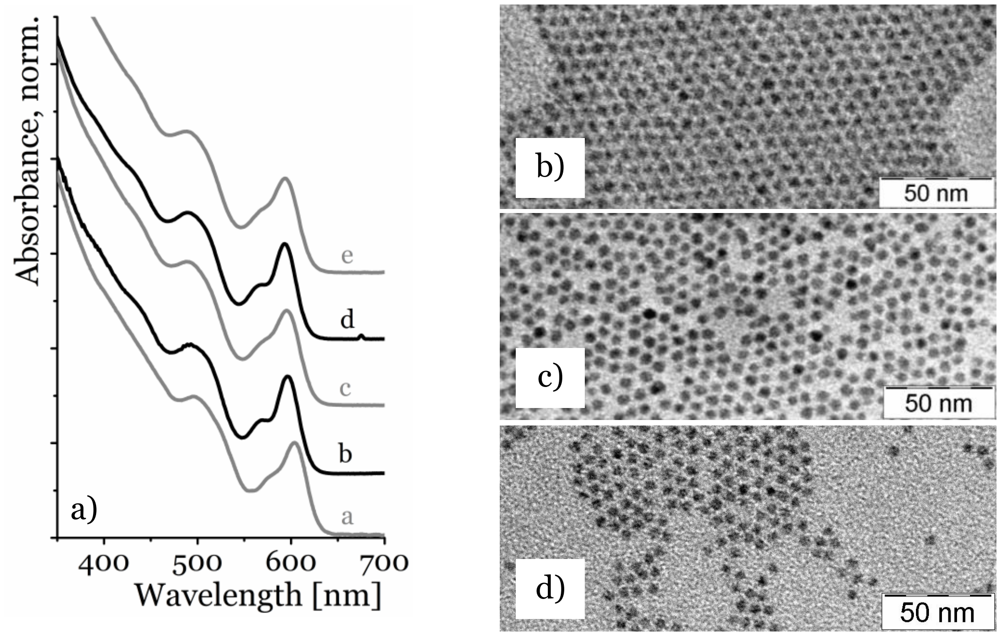

Figure 3. 12: Spectral improvement is also obtained utilizing lithium silylamide, whereas a mixture of lithium silylamide and tin oleate diminishes the effects.
a) Absorption spectra, assignment of spectra: a. standard hot injection without any *quasi*-seed; b. $[(Me_3Si)_2N]_2Sn$ (5%); c. $Sn(oleate)_2$ (5%); d. $[(Me_3Si)_2N]Li$ (10%); e. $Sn(oleate)_2$ (5%) + $[(Me_3Si)_2N]Li$ (10%). b-d) TEM images of particles corresponding to spectra c-e.

Due to this observation it was decided to examine the equivalent use of $Sn(oleate)_2$ synthesized from $SnCl_2$ as well as lithium silylamide and a combination of both as *quasi*-seed precursors. Judging from the absorption spectra (fig. 3.12), an improvement in spectral quality arises not only through the use of tin silylamide but also by using lithium silylamide as compared to the standard hot injection synthesis. To confirm this result, size dispersions (fig. 3.13 b) and quantum yields, QYs, (fig. 3.13 c) were compared as well as the mean particle diameter (fig. 3.13 a) and the QD concentration (fig. 3.13 d). QYs were calculated using the corresponding photoluminescence peak with respect to Rhodamine 6G following standard procedures.[12] As depicted in fig. 3.12 and 3.13, employing silylamides, $[(Me_3Si)_2N]_xM$ ($M^{x+} = Li^{1+}, Sn^{2+}$), as the *quasi*-seed precursor, results in the quality of the particles being increased with respect to their size distributions, as well as higher quantum yields. TEM images confirm these findings, (fig. 3.12 b-d) where a well ordered CdSe assembly is achieved only for particles synthesized in the presence of lithium silylamide.

However, worsening of particle quality results when using $Sn(oleate)_2$ synthesized from $SnCl_2$, which is attributed to its low reactivity. Only in combination with lithium silylamide, an improvement is observed. A comparable behavior is found for the synthesis of SnS nanoparticles[14] where large particulate materials (several tens

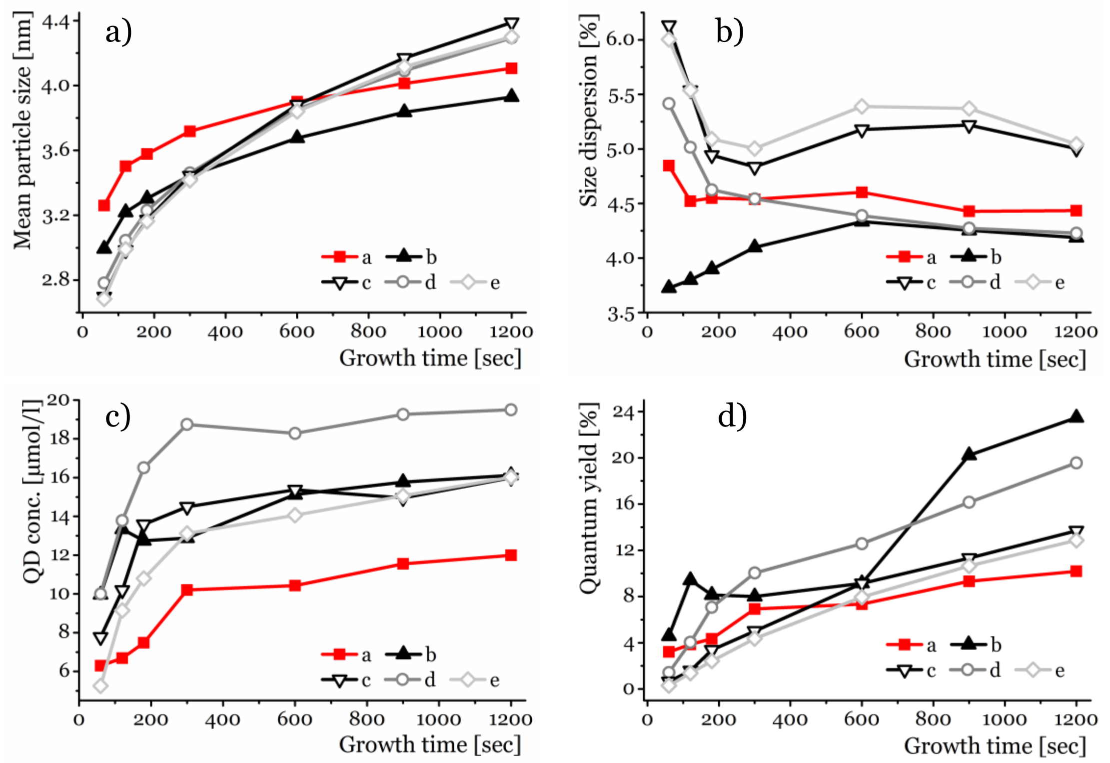

Figure 3. 13: Employing any tin species as well as lithium silylamide shows their activity in accordance with the qsg mechanism, although the evolution of size and size dispersion indicate diminishing effects.

(a) Mean particle sizes, (b) size dispersions, (c) QD concentrations and (d) quantum yields. Assignment of plots: a. standard hot injection without any *quasi*-seed; b. $[(Me_3Si)_2N]_2Sn$ (5%); c. $Sn(oleate)_2$ (5%); d. $[(Me_3Si)_2N]Li$ (10%); e. $Sn(oleate)_2$ (5%) + $[(Me_3Si)_2N]Li$ (10%).

of nanometers) are obtained via the use of $Sn(oleate)_2$ from $SnAc_2$, whereas narrow nanoparticle distributions consisting of small sizes (7 - 10 nm) are synthesized using tin silylamide. A reasonable explanation has not been found until now. However, a potential mechanism is a strong coordination of the Sn^{2+} by oleate molecules which may inhibit the access of hexadecylamine or *n*-trioctylphosphine oxide.

3.6. Laboratory batch up-scaling

Finally, the mechanism of the *quasi*-seeded growth is applied to the up-scaling of laboratory batches, to increase the number of resulting nanoparticles per synthesis. These efforts are necessary, as fundamental research often requires repeated experiments, which is material intensive, and consequently a large amount of particles of similar or even equal properties are needed. Furthermore, the syntheses of quantum dots is reproducible to just a certain degree and in addition to this, is time-consuming mainly due to pre- and post-synthetic cleaning steps. Therefore, large scale syntheses resulting in large amounts of QDs with equal properties could address those issues.

Considering the reaction environment (3-necked flask surrounded by a heating mantle and equipped with stirring bar and thermocouple), many parameters need to be optimized even if one simply increases the flask size and precursor concentrations. In a technical manner, the crucial parameters of a synthesis that change with respect to scaling-up are the heat transport from the heating mantle to the inner parts of the flask and homogenization of the solution involving the dispersion of the injected material. In accordance with the model of Sugimoto, a diffusion layer is suggested to exist around the particles within the diffusion controlled growth regime.[18] Furthermore, the growth rate of the particles within this regime is directly proportional to the diffusion constant and inversely proportional to particle size and diffusion layer width. The following relationship may be derived from eq. 2.7:

$$\frac{dr}{dt} \propto D\left(\frac{1}{r}+\frac{1}{d_L}\right) \tag{3.6}$$

This relationship suggests both the importance of the diffusion constants of the monomer species as well as the width of the diffusion layer. Hence, the stirrer significantly influences the whole reaction, as it controls the width of the diffusion layer (inverse proportionality of the material flow to the width of diffusion layer) as well as homogenizes temperature and concentration.

Regarding the chemical and economic aspects of a nanoparticle synthesis, temperature and concentrations of the starting materials as well as complexing agents play major roles. Considering a 10-fold scale-up of the synthesis of a colloidal material, at least 10-fold the amount of precursor must be utilized, whereas the stabilizer concentration is expected to be increased by a factor of 2 or less, as it is employed in excess within the “small-scale” synthesis. Consequently, the reaction volume increases and changes in viscosity are expected owing to differences in the complexing properties and the mixture composition.

Performing syntheses based on the standard hot injection method, all parameters mentioned need to be adjusted to prevent uncontrolled nucleation and growth. Therefore, the *quasi*-seeded growth approach is considered to be an aid in reducing those efforts to a minimum. As this method has already been shown to improve the synthesis of a small scale batch just by the addition of bis[bis(trimethylsilyl)amino] tin(II) without optimizing any parameter, it is suggested it may be helpful in simplifying up-scaling attempts.

Scale-up experiments were undertaken, by means of an increased flask size as well as precursor concentrations with respect to the batch scale. Therefore, 10-fold as well as 25-fold scale-up experiments are carried out, by increasing the Cd^{2+} concentrations from 0.4 to 4 and 10 mmol, which requires flask sizes of 50 and 100 ml, respectively. Due to the necessity of excess stabilizer by means of concentrations, comparative studies on reaction volume (V_R) vs. precursor concentration (c_{Prec}) were not possible, e.g. constant V_R + increasing c_{Prec} vs. constant c_{Prec} + increasing V_R.

As may be seen from fig. 3.14, applying the scale-up protocols, an increase in QD concentration is achieved with respect to the scaling factor. The improvements in particle quality due to the presence of tin silylamide are observed within the 10-fold experiments. Applying the qsg protocol smaller sizes and narrower size distributions are achieved with an increased number of particles as well as higher quantum

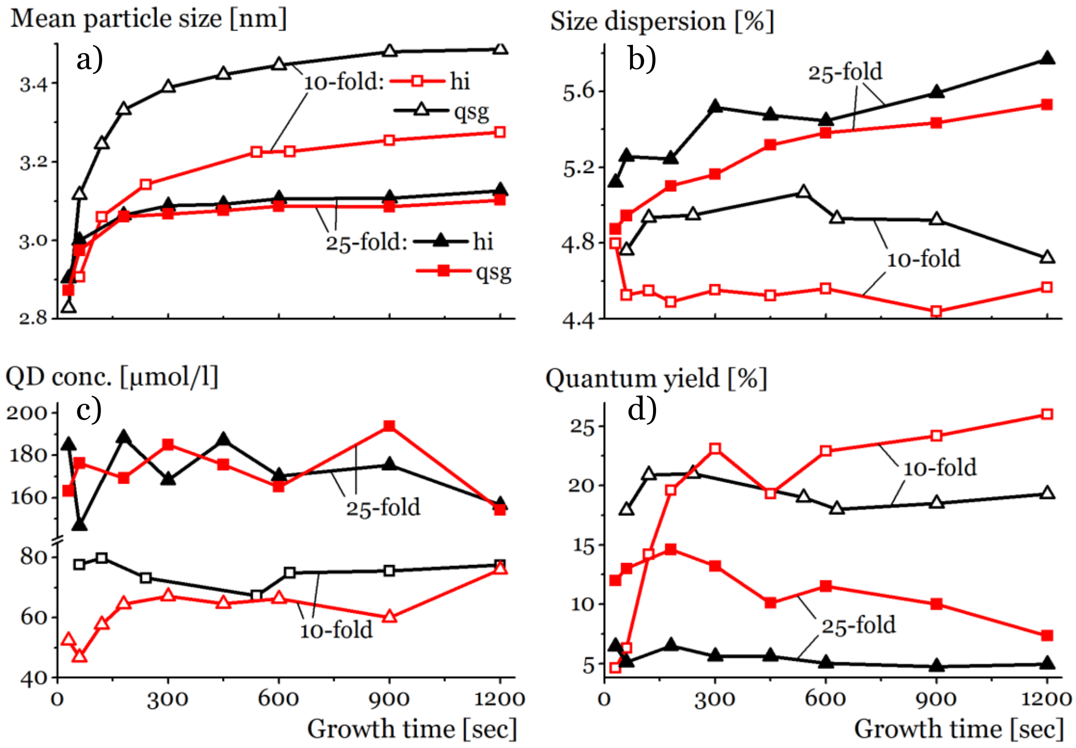

Figure 3. 14: The *quasi*-seeded growth mechanism allows for an easy 10-fold up-scaling, whereas a 25-fold protocol demands further optimization.
Data derived from standard hot injection (black lines and symbols) and *quasi*-seeded growth approach applying a 10-fold (open symbols) as well as 25-fold (filled symbols) protocol. Quantum yields are calculated with respect to Rhodamine 6G.[12] Synthesis details are given in the Appendix section A.3.

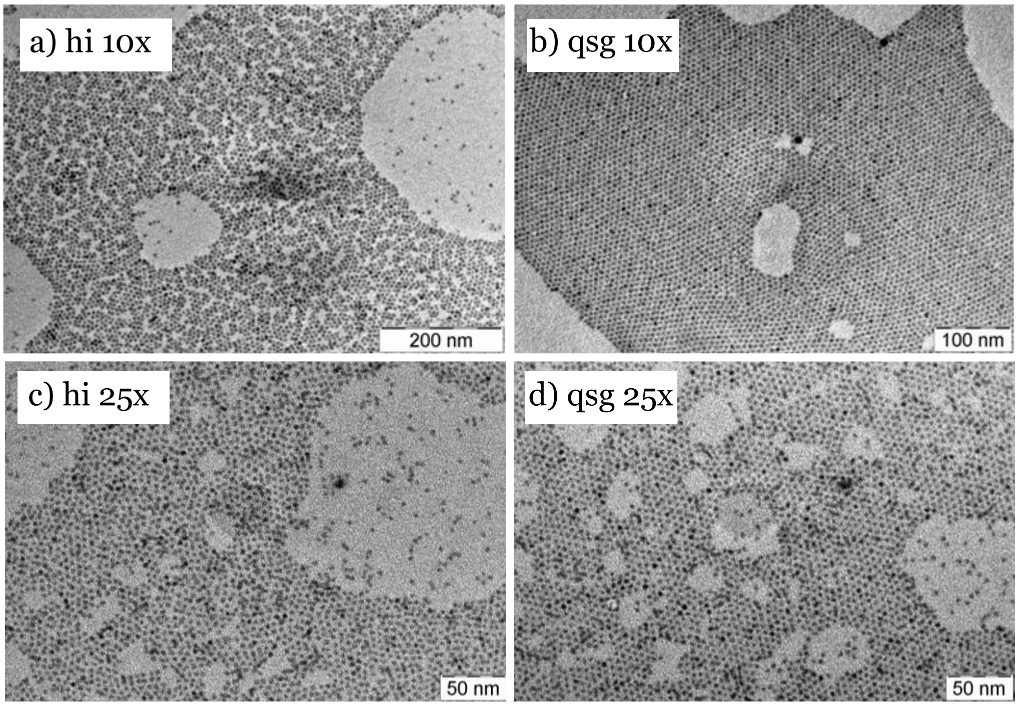

Figure 3. 15: TEM images for the up-scaled syntheses showing narrowest size dispersions for CdSe QDs obtained via the qsg approach for a 10-fold up-scaling.
10- and 25-fold scale-up in the absence (a,c) and presence of $[(Me_3Si)_2N]_2Sn$ (b,d), respectively.

efficiencies (fig. 3.14, open symbols). Very conspicuous is the QD concentration within the qsg protocol, which reaches a constant value, as expected from the cation exchange-mediated nucleation and growth mechanism.

However, less pronounced effects of the cation exchange-mediated nucleation are observed following the 25-fold scale-up protocols. Although the resulting sizes and associated QD concentrations are nearly similar, narrower size distributions and increased quantum yields are achieved with the *quasi*-seeded growth approach (fig. 3.14, filled symbols). These results indicate a less dominant effect of the cation exchange-mediated nucleation on the overall reaction within the 25-fold scale-up procedure. One reason for this is the large injection volume which must be increased to 10 ml for the 25-fold protocol, whereas it is possible to keep it constant at 4 ml for the 10-fold synthesis. The volume of the injection solution is defined by the solubility of the selenium in *n*-trioctylphosphine and hence the volume increase in the case of the 25-fold protocol is necessary. Due to the injection of this large volume, homogenization of the resulting mixture becomes a crucial factor and the cation exchange affects the system less. However, these effects are not eliminated completely, as the size dispersion is nevertheless narrower in comparison to the standard hot injection synthesis. From the size dispersions presented in fig. 3.14 b, the particles so obtained still possess a better ordering of the assemblies when applying the *quasi*-seeded growth approach, as seen in the TEM images in fig. 3.15.

3.7. Conclusion and outlook

In summary, an improvement in the hot injection synthesis for CdSe QDs is obtained by a simple addition of bis-(bis-trimethylsilyl)amino tin(II) in catalytic amounts. The suggested mechanism for cation exchange-mediated nucleation and growth is consistent with the data, whereas possibilities of alloying or incorporation are excluded by elemental analysis methods. Following this *quasi*-seeded growth approach, various *quasi*-seed concentrations and precursor species are investigated in a manner so as to optimize the reaction system. These examinations confirm the necessity of the high reactivity of the *quasi*-seed species. Thus the use of tin(II) or lithium(I) silylamides is required, as they form a complex coordinated species with oleic acid and hence keep their reactivity high. On the other hand, utilizing tin oleate as the *quasi*-seed species results in particles ensembles having larger polydispersities, which is attributed to the lower reactivity of the reactant species due to the complete coordination by oleate molecules. A further requirement for the success of the cation exchange-mediated nucleation and growth mechanism is the use of catalytic amounts of the *quasi*-seed species (5-10% of the Cd^{2+} concentration), as with higher concentrations (> 20%) competing effects are observed to occur. Although the completeness of the cation exchange reaction remains unaffected, the use of higher concentrations of tin silylamide results in an undefined or random reaction progression.

Finally, the implementation of applying these principles to up-scaling efforts is examined. The protocol can be successfully applied to a 10-fold concentration increase, whereas a further up-scaling is limited with respect to the optimization of the reaction conditions. Limitations are revealed by the volume one may swiftly inject and the reaction solution, as the homogenization of the resulting mixture then becomes a crucial parameter. Therefore, addressing these restrictions for i.e. a further laboratory up-scaling the method of injection as well as the stirring behavior requires additional consideration and optimization.

3.8. References

[1] M. Ethayaraja, R. Bandyopadhyaya, *Industrial & Engineering Chemistry Research* **2008**, *47*, 5982.

[2] a) H. Weller, U. Koch, et al., *Berichte Der Bunsen-Gesellschaft-Physical Chemistry Chemical Physics* **1984**, *88*, 649; b) H. S. Zhou, H. Sasahara, et al., *Chemistry of Materials* **1994**, *6*, 1534.

[3] a) D. H. Son, S. M. Hughes, et al., *Science* **2004**, *306*, 1009; b) M. V. Kovalenko, D. V. Talapin, et al., *Angewandte Chemie International Edition* **2008**, *47*, 3029.

[4] R. G. Pearson, *Journal of the American Chemical Society* **1963**, *85*, 3533.

[5] a) W. W. Yu, L. Qu, et al., *Chemistry of Materials* **2003**, *15*, 2854; b) C. de Mello Donegá , R. Koole, *The Journal of Physical Chemistry C* **2009**, *113*, 6511.

[6] V. C. S. Reynoso, Y. Liu, et al., *Journal of Materials Science Letters* **1996**, *15*, 1037.

[7] a) D. V. Talapin, J. H. Nelson, et al., *Nano Letters* **2007**, *7*, 2951; b) U. Woggon, F. Gindele, et al., *Physical Review B* **1996**, *54*, 1506; c) H. Htoon, M. Furis, et al., *Physical Review B* **2008**, *77*, 035328.

[8] M. Yarema, S. Pichler, et al., *ACS Nano* **2011**, *5*, 3758.

[9] a) V. Kloper, R. Osovsky, et al., *The Journal of Physical Chemistry C* **2007**, *111*, 10336; b) R. Osovsky, V. Kloper, et al., *The Journal of Physical Chemistry C* **2007**, *111*, 10841.

[10] K. Yu, M. Z. Hu, et al., *The Journal of Physical Chemistry C* **2010**, *114*, 3329.

[11] a) E. V. Shevchenko, D. V. Talapin, et al., *Journal of the American Chemical Society* **2003**, *125*, 9090; b) M. A. Hines, G. D. Scholes, *Advanced Materials* **2003**, *15*, 1844; c) M. V. Kovalenko, W. Heiss, et al., *Journal of the American Chemical Society* **2007**, *129*, 11354.

[12] M. Grabolle, M. Spieles, et al., *Analytical Chemistry* **2009**, *81*, 6285.

[13] a) A. L. Efros, M. Rosen, *Physical Review Letters* **1997**, *78*, 1110; b) Y. Zhu, S. McKernan, et al., *Journal of Applied Physics* **2010**, *108*, 123104.

[14] S. G. Hickey, C. Waurisch, et al., *Journal of the American Chemical Society* **2008**, *130*, 14978.

[15] M. J. Polking, H. Zheng, et al., *Journal of the American Chemical Society* **2011**, *133*, 2044.

[16] P. Zolotavin, P. Guyot-Sionnest, *ACS Nano* **2010**, *4*, 5599.

[17] M. Yarema, M. V. Kovalenko, et al., *Journal of the American Chemical Society* **2010**, *132*, 15158.

[18] T. Sugimoto, *Advances in Colloid and Interface Science* **1987**, *28*, 65.

4

Thermodynamic and kinetic effects on the synthesis of CdTe QDs

Precursor activation by altered injections

4.1. Introduction

Based on the fundamentals presented in chapter 2, from the point of view of classical crystallization theory the prime event in the formation of nanoparticles is the discrete nucleation of the monomer material formed upon precursor injection.[1] The event of nuclei formation is followed by subsequent processes in their growth which are slower and thus in principle provide a greater degree of control. Therefore, the overall growth process may be differentiated into two stages (a) monomer diffusion to the surface of the particles and (b) deposition of the monomers onto the particle surface.[2] Following this, the particle sizes increase continuously as a result of the deposition of monomeric material. These growth processes are described theoretically by the Ostwald theory and are mathematically explained within the Lifshitz-Slyozov-Wagner (LSW) theory.[3] The growth stage may begin within the reaction controlled regime, as the monomer concentration is supposed to be high enough to neglect diffusion processes. As the consumption of monomer proceeds a size focusing step follows[1b, 4] which occurs, in accordance with the LSW theory, within the diffusion limited regime resulting in larger particles growing more slowly than smaller ones. During the growth the concentration of the monomers, formed from precursor species, decreases reaching an equilibrium concentration, at which stage the critical radius approximates the mean radius of the particle ensemble.[3a] At this point the smallest particles begin to dissolve and provide free monomer for the growth of the larger particles; a process termed as Ostwald ripening and characterized by a defocusing of the size dispersion.[1b, 4-5]

In special cases very small quantum dots are formed, so called magic-sized clusters (MSCs).[6] These species possess a local minimum in their chemical potential and invalidate the Gibbs-Thomson equation, as depicted in fig. 4.1.[4] In the presence of these species discontinuous growth may occur whereby the size increases stepwise via different sizes of MSCs.[7] These highly stable MSC species are usually formed during nucleation and their growth is assumed to be discontinuous due to differences in the thermodynamic stability of the differently sized MSCs.[1c] This means that these differently sized MSCs represent various local minima in the chemical potential and hence a size increase is denoted as *forward-tunneling*.[4] Here, "tunneling" means a change in the chemical potential by overcoming a thermodynamic barrier (see fig. 4.1). The stability of the MSCs is attributed to a delicate balance between surface and intrinsic energy, as they exhibit a closed shell electronic structure.[8] In some cases, the growth of nanoparticles may involve MSCs

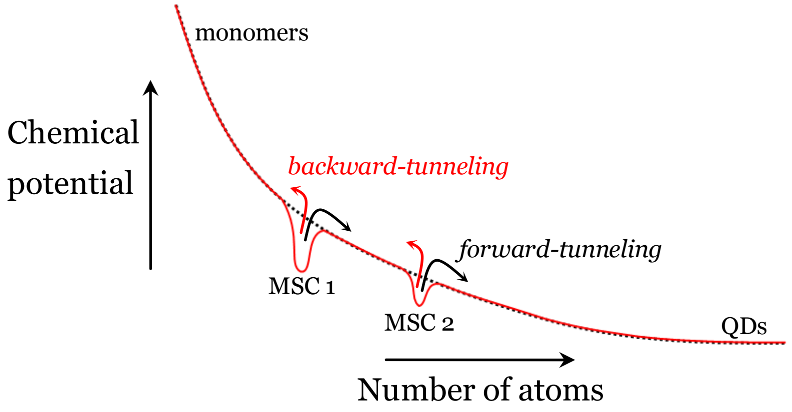

Figure 4. 1: Illustration of the size- and configuration-dependence of the chemical potential of MSCs and QDs.
Black dotted line: Gibbs-Thomson equation (size-dependence), red solid line: configuration-dependence. Arrows indicate backward- (red) and forward-tunneling (black) by overcoming the higher or lower thermodynamic barrier, respectively. Reproduced from Z. A. Peng.[4]

following a discontinuous mechanism segueing into a continuous.[7, 9] However, continuous growth of MSCs is found within two-phase systems for CdS QDs, wherein the particle growth is proposed to be initiated by MSCs acting as critical nuclei.[10] In a recent report from Jiang and Kelley an alternative growth mechanism was suggested for CdSe nanorod growth where, in the initial stages, an equilibrium between MSCs and CdSe monomers exists. The monomers form the nuclei which grow further either by deposition of free monomer or monomer released from MSCs due to their dissolution.[11] The fate of MSC dissolution is favored under conditions of low monomer concentrations, as this process succeeds via a tunneling through a high energy barrier. Hence it is understood as an increase in chemical potential and is denoted as *backward-tunneling*.[4]

From a chemical point of view, the growth of QDs is supposed to proceed via the deposition of monomeric material, which is stabilized in accordance with the initial composition of the precursor material. For the formation of cadmium chalcogenide monomers a reaction mechanism is proposed whereby the chalcogenide species is coordinated by alkylphospines, whereas the cation precursor contains long chained carboxylic or phosphonic acids. The proposed mechanism is shown in fig. 4.2, where the cation acts as a Lewis acid and coordinates the chalcogenide resulting in the phosphorus = chalcogenide double bond being weakened.[12] The formation of the monomer species involves the oxidation of the alkylphosphines to their respective phosphine oxides as well as the formation of anhydrides of the participating acids.[12-13] Following fig. 4.2 (i) *n*-trioctylphosphine (TOP) is oxidized to *n*-trioctylphosphine oxide (TOPO) and (ii) anhydrides are formed from carboxylic or phosphonic acids.

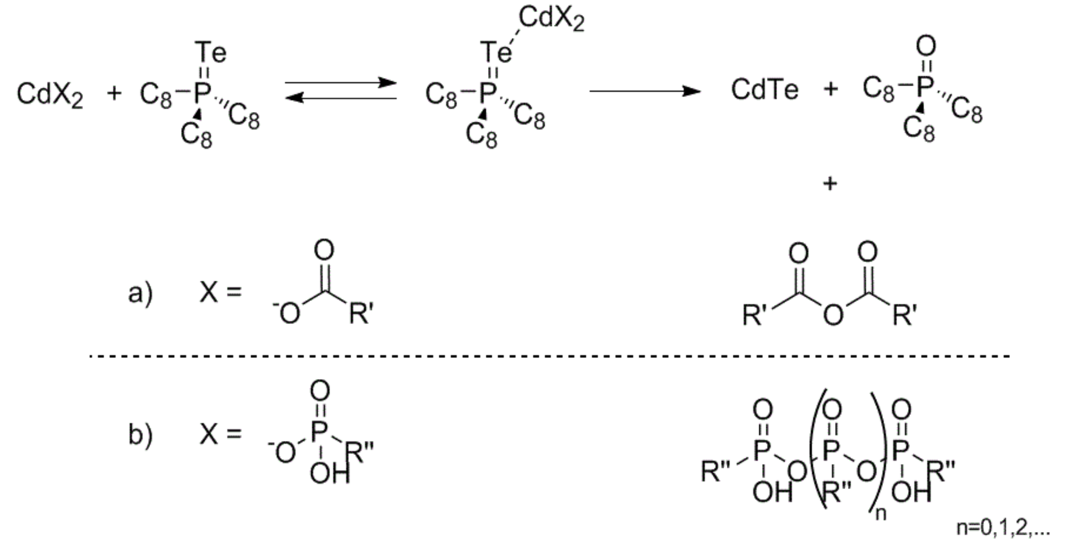

Figure 4. 2: General reaction mechanism for the precursor conversion towards CdTe. The cadmium precursor contains a) carboxylic or b) phosphonic acids, whereas the tellurium is complexed by *n*-trioctylphosphine (Te=P(C_8)$_3$).

As is suggested by this mechanism, the formation of monomer material is easily influenced by changes of stabilizer as well as ion precursor concentrations. Hence various side reactions need to be considered as, in the presence of an excess of either a precursor species or free stabilizer molecules, the reaction mechanism, as well as the stability/ reactivity of the monomers, is affected.[12-13]

4.2. Precursor activation by altered injections

For the standard hot injection method for the synthesis of CdTe QDs usually the cadmium source is placed inside the reaction vessel for heating and the tellurium species is injected or alternatively both may be simultaneously injected.[8b, 14] In this chapter the growth of CdTe QDs has been investigated in detail using a protocol based on altered injection pathways, i.e. injection of the cation precursor to the anion and vice versa. The growth kinetics of the particles at two different reaction temperatures was studied by means of optical spectroscopy. The observed differences are caused by the different complexes formed, which affect the stabilities and hence reactivities of the precursor species. Consequently, the choice of the precursor combination has a significant influence regarding homogeneous nucleation and controlled growth.

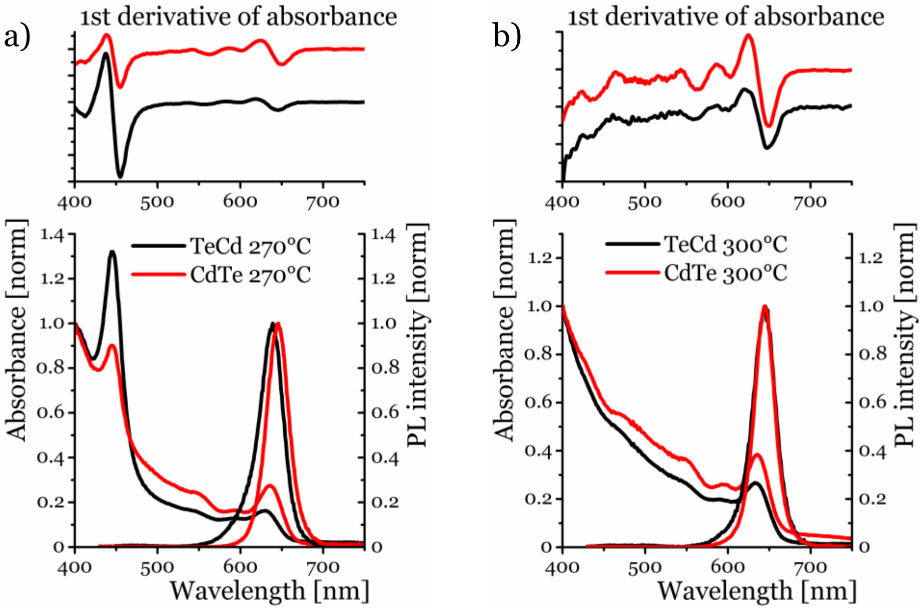

Figure 4. 3: Synthesis improvement by means of narrower size dispersions is achieved for cation injection as indicated by more intense and better separated excitonic transitions.

Black lines represent the anion and red lines the cation injection pathway. Injection temperatures of (a) 270°C and (b) 300°C were employed.

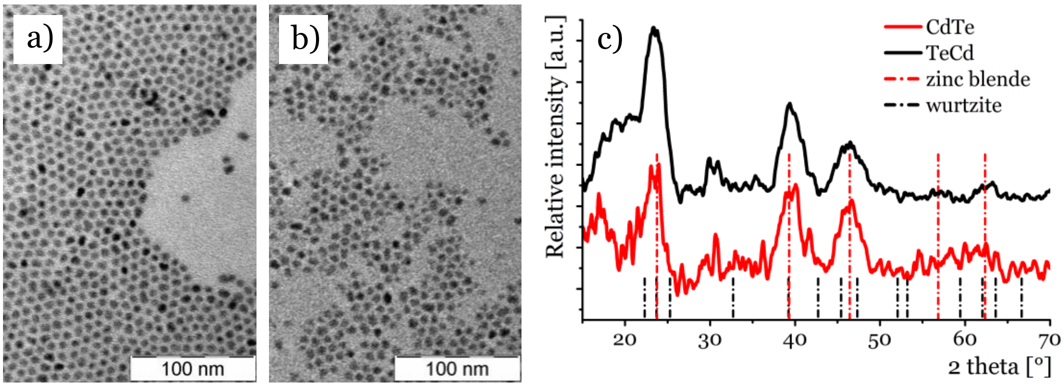

Figure 4. 4: TEM image and XRD patterns of CdTe QDs synthesized via two altered injection pathways result both in spherical shaped particles with cubic, zinc blende crystal structure.

Exemplarily chosen TEM images of CdTe QDs derived from a) cation and b) anion injection, additional TEM images are presented in the Appendix B. c) The XRD patterns of the cation (red, solid) and anion (black, solid) injection match the powder diffraction file number 15-770 for zinc blende (cubic) CdTe (red, broken) and show an expected broadening compared to bulk material. For comparison the theoretical reflexes of the wurtzite CdTe (black, broken) is shown and can be excluded.

Fig. 4.3 presents the absorption spectra with the corresponding first derivative and the photoluminescence (PL) spectra of CdTe nanoparticles (~ 4 nm) synthesized via two injection pathways at two different injection temperatures. From the absorption spectra it is clearly notable that several electronic transitions are present indicating the high quality of the nanocrystals obtained using both routes. However, as can be seen from the first derivative of the absorption spectra in fig. 4.3, the electronic transitions are more pronounced for the cation injection as they exhibit sharper peaks in the spectra of the resulting QDs. A further difference observed in the spectra are the absorption features associated with the formation of magic-sized clusters (MSCs)[4] present in the spectra of CdTe synthesized at an injection temperature of 270°C for both routes. These discrete absorption peaks at around 445 nm have been previously reported[6d, 14i] and are attributed to a stable CdTe cluster species with a diameter of approximately 1.8 nm.[8b, 15]

To find reasonable explanations for these significant differences the temporal evolution of the absorption spectra was further investigated. Therefore after injection of each particular precursor a sample series was taken at regular time intervals to ensure comparable data sets for the particle growth. However, to exclude morphological and crystallographic differences TEM imaging as well as x-ray diffraction analyses have been undertaken. As results, both pathways yield sphericalCdTe nanoparticles in zinc blende modification as may be seen from the TEM images and the X-ray diffraction patterns (shown in fig. 4.4).

i. Particle growth

In all experiments in this study a continuous red shift of the first absorbance maximum can be determined, indicating the growth of the QDs. The complete spectral evolution for particle ensemble measurements is presented in fig. 4.5. As depicted in this figure for injections at 270°C the QD growth is attended with a decrease in the MSC absorbance peak intensity indicating a decline in the MSC population. The mechanistic role of the magic-sized clusters as well as their formation and disappearance under the present reaction conditions are discussed below in section 4.3.

The following discussion focuses on the data derived from the first excitonic transitions of the QDs, whereas the features of the MSCs are disregarded. Therefore, the growth kinetics are evaluated by comparison of the particle sizes, the corresponding size dispersions as well as the concentrations of the QDs and the monomeric cadmium as a function of growth time. The monomeric cadmium represents all species that include cadmium which is not incorporated into the QDs, namely the cadmium precursor, the [Cd-Te] monomer as well as the MSCs. For details of determination and calculation of the mentioned values see section 4.5.

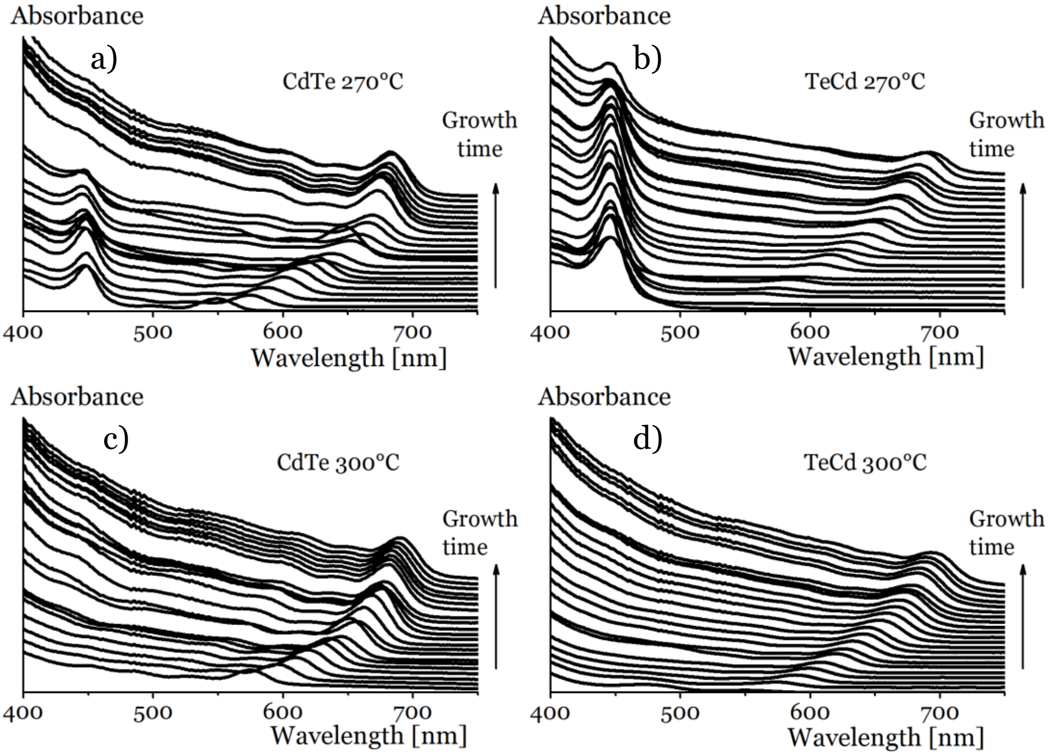

Figure 4. 5: Temporal evolutions in the absorbance of the raw data indicate the more pronounced excitonic transitions within the cation injection.
CdTe QDs derived from (a,c) cation and (b,d) anion injection at an injection temperature of (a,b) 270°C as well as (c,d) 300°C, respectively.

Considering the evolution of the particle sizes, for both reaction temperatures faster growth rates are obtained for the cation injection pathway in the beginning of the synthesis (see fig. 4.6 a). Furthermore, the first absorption spectra derived from cation injection, taken after 20 seconds of growth, clearly show the absorbance of the QDs, whereas for the anion pathway those features evolve with a certain delay. Additionally, while the reaction proceeds a significant alteration of the growth rate within the cation injection pathway is obvious. Likely reasons for such a change in the growth rate are the following:

- The consumption of a contributing species, i.e. the monomer species may be exhausted to an equilibrium value;
- A change in a growth mode, i.e. from reaction to diffusion control; or
- The passing from growth to ripening by reaching an equilibrium monomer concentration.

Those processes can be described by various characteristic parameters including the QD concentration and the monomeric cadmium concentration as well as the particle size dispersion (cf. fig. 4.6 b-d).

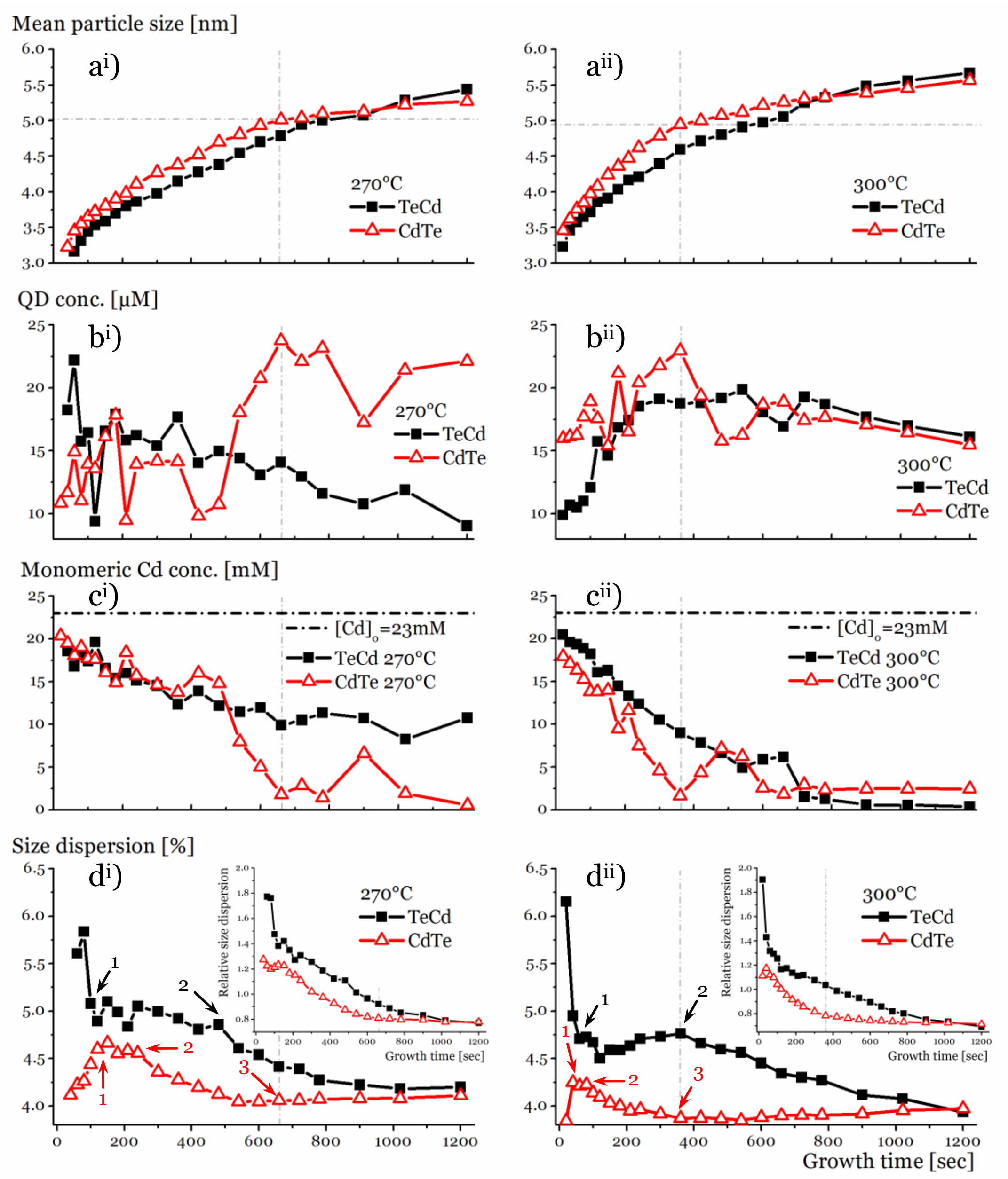

Figure 4. 6: Significant differences are achieved comparing characteristic parameters for the evaluation of the QD ensemble kinetics.
Details for the calculation of the data points are given in section 4.5. Anion injection: black, filled squares, cation injection: red, open triangles. The grey intermittent lines indicate the point in time and the corresponding particle size of the change in the growth rate within the cation injection. Numbers in superscript denote the injection temperature (i) 270°C and (ii) 300°C. Arrows indicate the beginning of the following modes: 1) reaction controlled growth; 2) diffusion controlled growth; 3) Ostwald ripening.

As already mentioned within the introduction section, the injection is followed by the nucleation process which timely may overlap with particle growth and dissolution, depending on the Gibbs free energy. Thus, in the present system the particle size dispersion during the nucleation event does not follow a defined trend by means of broadening or narrowing. However, the growth process can be differentiated mainly into three modes which, from classical crystallization theory, are characterized by strict evolutions of the size dispersion. Thus, the growth starts with the reaction controlled growth, which segues into the diffusion limit and finally ends up in ripening. These three growth modes are characterized in tab. 4.1.

Table 4. 1: Evolution of ensemble parameters characterizing the growth mode.

Parameter	**reaction limit**	**diffusion limit**	**ripening**
QD concentration	constant	constant	decreasing
monomeric Cd concentration	decreasing $c_0 > c_{react}$	decreasing $c_{react} > c_{diff}$	constant $c_{diff} > c_{ripe} \sim c_{equil}$
size dispersion, ξ	constant	decreasing	increasing
relative size dispersion, $\tilde{\xi}$	decreasing	decreasing	increasing

Details for the parameters including their definition and calculation are given in chapter 2 section “*Growth*” as well as section 4.5 within this chapter.

Applying these characteristic conditions to the different evolutions presented in fig. 4.6 the growth modes for the syntheses can be determined. As shown in fig. 4.6 c, the monomeric cadmium concentration more quickly depletes within the cation injection pathway, resulting in the observation of Ostwald ripening within the investigated time range. All three modes, as indicated by the arrows in fig. 4.6 d, reaction and diffusion limited growth as well as Ostwald ripening are only observed within the cation injection. Particle growth with its origin in the anion injection pathway proceeds slower and hence the monomer concentration depletes more slowly. Consequently only the reaction and diffusion limited growth regimes can be detected for the anion injection pathway, within the investigated time range.

Regarding reactivity differences between the two injection pathways the rate constants are determined from the size-time-plots (fig. 4.6 a). The results are shown in tab. 4.2. As expected within the classical crystallization theory the reaction limit possesses the largest rate constants, whereas the ripening represents the slowest process. Additionally, the growth rate increases with the reaction temperature and for equal reaction temperatures faster rates are obtained for the cation injection pathway.

However, recent publications retreat from the classical theory with regard to the differences in the reaction and diffusion limits. It has been suggested that a narrowing of the size distribution within the reaction controlled growth regime is

Table 4. 2: Rate constants as results of a linear fit of different growth regimes.

Linear fit equation: $d = d_{st} + k_{mode} \cdot t$		**Anion injection**		**Cation injection**	
		270°C	**300°C**	**270°C**	**300°C**
Regime of reaction control	k_{react}	$2.21\,\frac{pm}{s}$	$2.63\,\frac{pm}{s}$	$2.92\,\frac{pm}{s}$	$4.96\,\frac{pm}{s}$
	R^2	0.9906	0.9792	0.9809	0.9741
Regime of diffusion control	k_{diff}	$1.33\,\frac{pm}{s}$	$1.24\,\frac{pm}{s}$	$2.30\,\frac{pm}{s}$	$2.95\,\frac{pm}{s}$
	R^2	0.9366	0.9812	0.9961	0.9804
Regime of Ostwald ripening	k_{ripe}	—	—	$0.52\,\frac{pm}{s}$	$0.62\,\frac{pm}{s}$
	R^2	—	—	0.9544	0.9116

possible.[16] Intuitively this seems logical when one imagines that with a constant deposition rate smaller particles require less material to complete a monolayer. Hence, assuming a constant reaction rate, smaller particles grow faster than larger ones. Additionally, it is claimed that the influence of a diffusion limit is doubtful within the synthesis of QDs. One reason for this being the determination of smaller growth rates as theoretically expected for diffusion controlled regimes.[16] Following simulations by van Embden et al.[16b], rates of diffusion limited conditions are three orders of magnitude faster than those of the reaction limit. Although, similarities are found in the progression of mean particle sizes and size dispersions for diffusion and reaction limits, the results suggest that under diffusion control ripening occurs to a greater extent in a fraction of the reaction time.[16b] Nevertheless, under the present conditions only a slow ripening is observed within the cation injection pathway. Additionally, the differences of the growth rates are obvious, but the order of magnitude does not differ significantly. Consequently, the argumentation in favor of the classical theory is recommended here.

Finally, it is found that the change in the rate of the growth mode can be associated with the passing into Ostwald ripening. This is indicated by i) reaching an equilibrium monomer concentration, ii) the beginning of a decrease in the particle concentrations, and iii) a broadening of the respective size dispersions, as shown in fig. 4.6. The occurrence of Ostwald ripening within the cation injection pathway, is suggested to proceed due to the ability of phosphonic acids to reversibly ripen particles via the formation of cadmium phosphonates and hydrogen selenide.[17] Therefore, protonated phosphonic acids are required. Within the cation injection pathway higher TDPA concentrations in comparison to the anion pathway are expected, as within the anion pathway a kind of aging of the cadmium oleate by the TDPA is observed. This aging is manifested by the formation of coordinating polymers, where Cd^{2+} ions are bridged by de-/ protonated acids, either carboxylic or phosphonic acids.[17] In comparison to the fatty acid the deprotonation of TDPA is favored, hence the concentration of free phosphonic acid decreases. This argument is supported by theoretical calculations where higher binding energies are attributed to the cadmium-phosphonate bond.[18] However, within the cation injection the cadmium fatty acid complex is injected to initiate the reaction. Hence, the efficiency of TDPA protonolysis is expected to be lower and consequently the concentration of free phosphonic acid is higher.

ii. Photoluminescence properties

Finally the emission properties of the nanoparticles were studied in order to determine how they are affected by the different growth kinetics, particularly the full width at half maximum (fwhm) but also the photoluminescence quantum yields (QY). These parameters portray the optical quality of the nanoparticles and provide additional information about the condition of their surface.

As depicted in fig. 4.7, the evolutions of the photoluminescence (PL) spectra reflect the trends in the size evolution of the QDs. For the anion injection pathway a nearly linear red shift of the PL position is observed, whereas for the cation pathway a "bend" in the rate of the red shift is apparent. Within the cation injection it is obvious that the PL intensity increases after the bend in the growth rate occurs. Additionally, narrower size distributions, delineated by the fwhm, and much higher PL intensities are obtained following the cation injection pathway. Those effects are

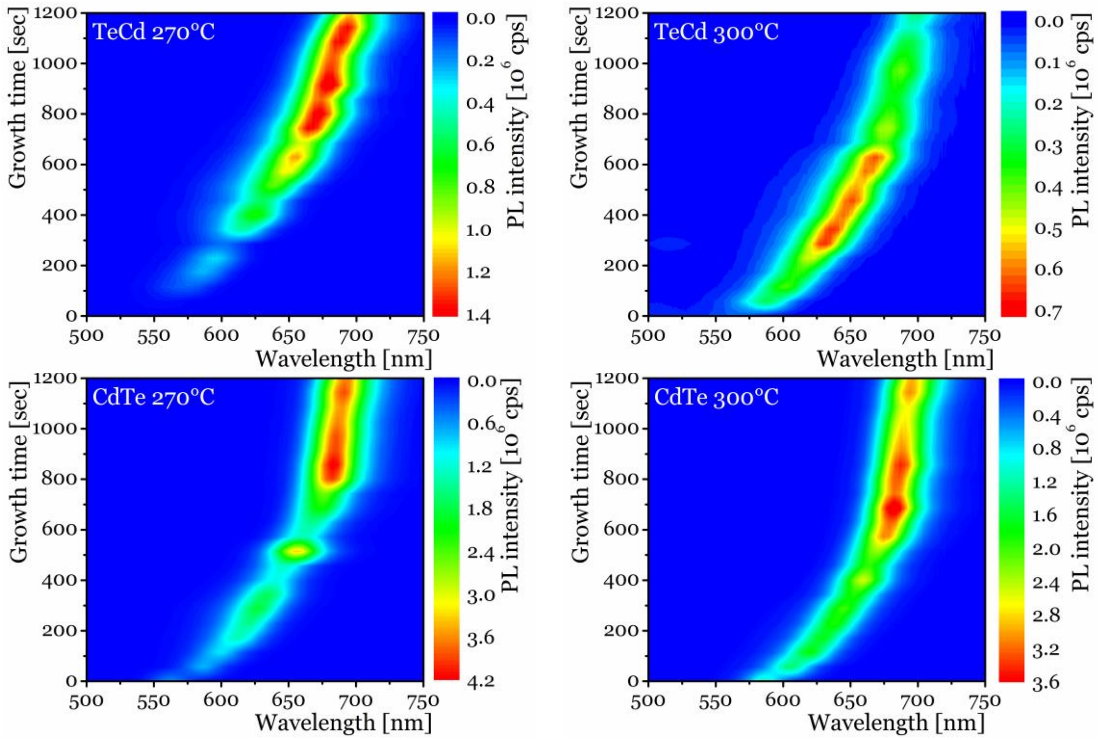

Figure 4. 7: Evolution of the photoluminescence raw data for CdTe QDs obtained via altered injections which reflect the observations obtained by the absorbance data.
Top (lower) panel shows the anion (cation) injection. Each line of the growth time (y-axis) represents a PL spectrum with an intensity profile corresponding to the color bar.

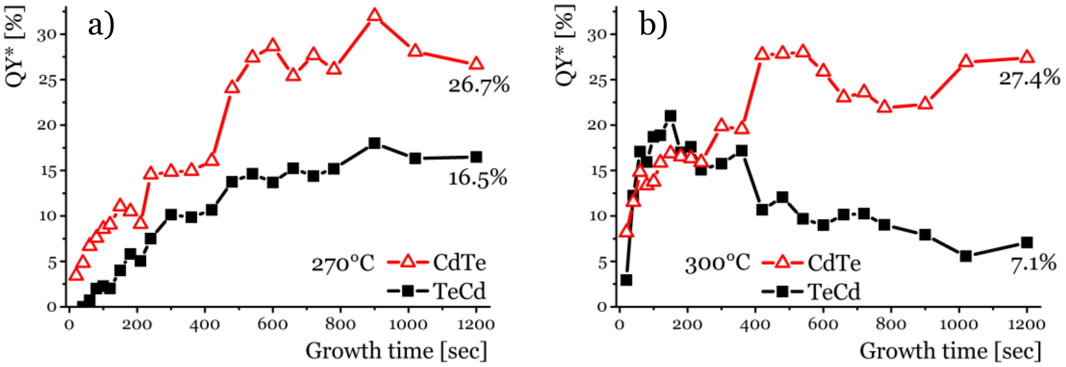

Figure 4. 8: Following the cation injection higher quantum yields are obtained. Comparison of different injection temperatures (a: 270°C, b: 300°C) for both injection pathways: anion (black squares) and cation injection (red triangles).
* Absolute QY values are determined for the last data points versus Rhodamine 6G, all other points are related to these values utilizing the absorbance at 400 nm and taking the particle concentrations into account.

reflected in the photoluminescence quantum yields, QYs, as they represent the ratio of emitted to absorbed photons within a QD ensemble. Thus these values give evidence for the electronic nature of the QDs regarding defect and surface states.[19] Therefore, the absolute QY is determined for each last data point of every data set. Following standard procedures, the integrated emission peaks are compared with a solution of Rhodamine 6G in ethanol.[20] Finally, the QYs of the associated points of the data set are calculated using the area underneath the PL peak (excitation at 400 nm) normalized to the QD concentration and related to the absolute value. The resulting QYs are presented in fig. 4.8, where the absolute values from comparison with Rhodamine 6G are given as values.

For both reaction temperatures higher QYs are obtained within the cation injection pathways. This especially is affected by the kinetics of crystal growth via the monomer deposition rate as well as the surface coverage by stabilizing agents. Too fast a deposition rate may result in a greater concentration of internal defects and thus affect the emission properties of the material. On the other hand, incomplete surface coverage introduces dangling bonds and hence additional recombination pathways, either of a radiative or non-radiative nature. In connection with this, in the present study higher efficiencies are revealed within the cation injection pathway, indicating the formation of crystals with fewer defects and/or a more efficient surface coverage. One reason for this is the decrease in the growth rate constant observed for both temperatures which, in combination with a decreased monomer deposition rate, allows for the etching of internal defects due to ion diffusion (annealing of nanocrystals).

iii. Conclusion

Within the present synthesis study, the injection pathway is altered. Therefore, the concentrations of stabilizers as well as the overall reaction volumes are kept constant.

Regarding the complexation of the participating ions initially TOP binds to tellurium and cadmium is coordinated by oleic acid. Furthermore, independent of the injection pathway the synthesis is undertaken using an excess of TOPO. These coordinating molecules compete for the cadmium ions with the original phosphonate or carboxylate ligands and as a weak binding ligand it increases the reactivity of the cadmium species.[21] Thus, the only difference between the syntheses pathways is related to the presence of TDPA: within the anion injection pathway it is present with the cadmium, whereas it is present with tellurium in the cation pathway.

A type of cation precursor deactivation is suggested for the anion injection pathway where the cadmium precursor (cadmium oleate) is present with the TDPA inside the reaction flask. By means of an aging process the cadmium species is estimated to become coordinated by TDPA (cf. fig. 4.9 a). This exchange of an oleic acid moiety for a phosphonic acid at the cadmium leads to higher precursor stability and hence decreases the reactivity. The driving force for the exchange of the stabilizing agent is a stronger complexation of cadmium ions by phosphonates. Experimentally this is obtained within the anion injection pathway during the evacuation step (to remove moisture, air and volatiles; cf. Appendix A) after addition of the cadmium oleate to the TDPA containing reaction mixture. The process of ligand exchange results in a highly viscous, white turbid solution, which is attributed to a polymeric structure of cadmium and TDPA in which the Lewis acid Cd^{2+} binds to adjacent phosphonate oxygens.[12, 17, 22]

However, in the cation injection pathway the tellurium is present with the TDPA inside the reaction flask. Here, an activation of the tellurium by the TDPA is suggested, although it does not coordinate to tellurium.[11] The activation is expected via the use of free phosphonic acids as it is proposed to nucleophilicly attack the phosphorous of TOP or TOP-Te with a net reaction as shown in fig 4.9 b.[12]

According to Jiang et al., within this reaction TOP is the better Lewis base and hence the formation of TOPO is favored.[11] The resulting molecules, namely monotetradecylphosphine $C_{14}P\text{-}H_2$, and TOPO as well as the intermediate species (monotetradecylphosphinic acid, and monotetradecylphosphine oxide) do not coordinate tellurium atoms. Hence, significant amounts of TOP are converted, whereas the reactivity of TOP-Te is increased by decreasing the stability of the complex. Under

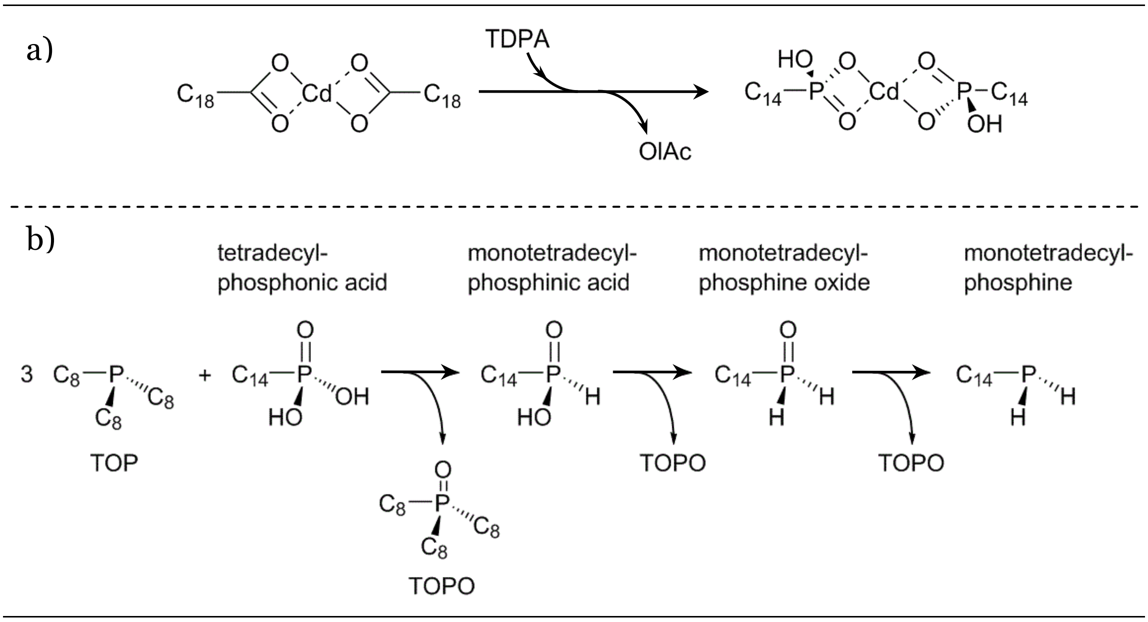

Figure 4. 9: Chemical reactions about the influence of TDPA on Cd(oleate)$_2$ as well as free TOP.

a) Deactivation reaction: substitution of the fatty acid ligand by the phosphonate ligand. b) Oxidation reaction of TOP to TOPO vie reduction of TDPA to monotetradecylphosphine.

the present reaction conditions, this reaction is expected to occur in both injection pathways, but to a greater extent within the cation injection due to the absence of the cadmium species.

Additional evidence for the proposed anion activation as well as the prevented cation deactivation is given by the increased nucleation reactivity within the cation injection. As oleic acid as ligand is known to inhibit the nucleation event[23], the hindered substitution of the oleate ligand by the phosphonates keeps the concentration of the free fatty acid relatively low. Hence, in combination with the activated tellurium the nucleation event is accelerated, as indicated by the narrower size distributions at the initial stages of the synthesis (< 4.5 %) following the cation injection pathway (cf. fig. 4.6 d). This fact is additionally indicated by the later appearance of the first absorbance maxima in the spectra for the anion injection (cf. fig. 4.5). By contrast, in the case of the cation injection a distinct first absorbance maximum appears in the initial stages of the reaction (20 s growth time), indicating a fast nucleation event with fast subsequent growth. This is possible as oleic acid is ascribed to facilitate a coordination that is labile with respect to attachment and detachment of monomers. Hence it promotes particle growth by increasing the rate of monomer deposition.[16b] However, the exchange of the complexing agent, from fatty to phosphonic acid, is also suggested to occur during the cation injection but may require some time and therefore does not affect the nucleation event.

iv. Supporting experiments

The made conclusions are underpinned by a study where the Cd-to-Te-ratio is varied. Significant effects of precursor activation are observed by utilizing cadmium in deficit (cf. fig. 4.10) or in excess (cf. fig. 4.11). Those effects are the well defined changes in the growth rate for the cation injection pathway as well as differences in the initial size distributions in comparison to the 1:1-ratio. It is observed, that the particle growth is affected by a deficiency of cadmium. There the TDPA-to-Cd- as well as the TDPA-to-OlAc-ratio is increased, resulting in a wider final size distribution for the cation injection (cf. fig. 4.10 b,d). A possible reason for this is the retardation of the subsequent nuclei growth due to enhanced interactions of the $Cd(oleate)_2$-complex with excess TDPA molecules as well as increased nuclei dissociation rates due to the stronger binding ligands.[16a] Additionally, this broadening is associated with ripening processes which are associated with an increased concentration of free phosphonic acid. On the other hand, due to the excess of the phosphonic acid within the anion injection the tellurium activation seems increased, which is indicated by narrower size dispersions. It is notable, that for effective Te activation by free TDPA molecules high temperatures are required, as may be seen for injection temperatures of 300°C where a high degree of anion

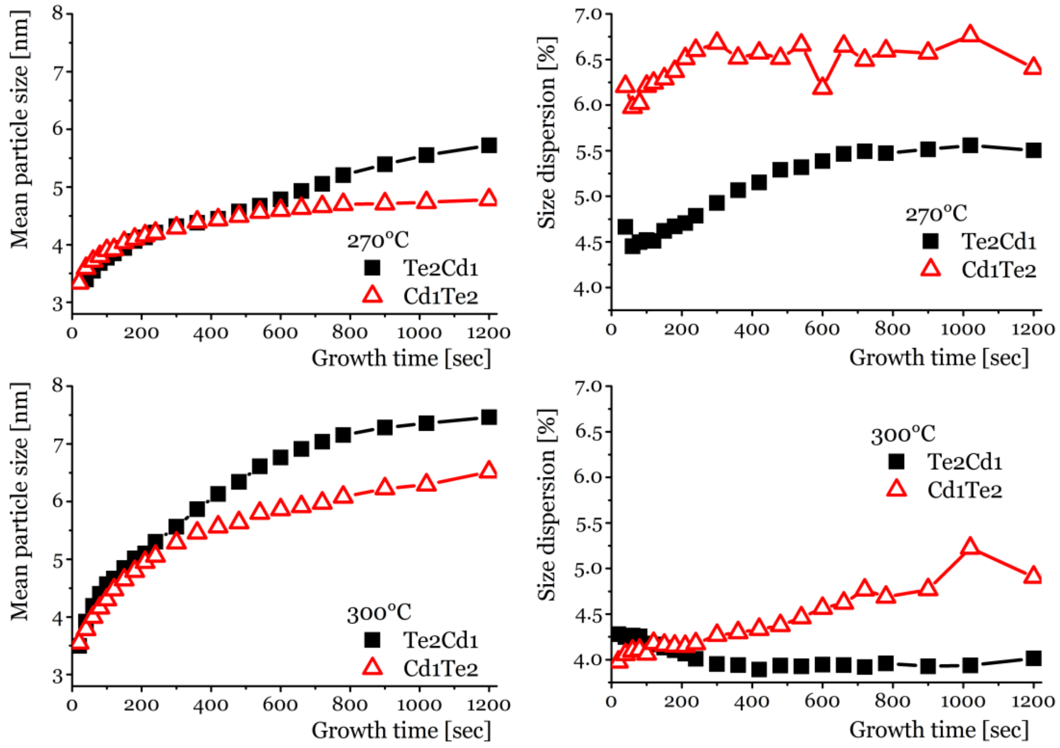

Figure 4. 10: CdTe growth kinetics and size dispersion under conditions of cadmium deficit.
Comparison of anion (black squares) and cation injection (red triangles) at injection temperatures of 270°C (upper panels) and 300°C (lower panels).

activation results in very narrow initial size distributions within the cation injection.

This is supported within syntheses utilizing deficiencies of tellurium (cf. fig. 4.11). There the TDPA-to-TOP-ratio is increased, by which the tellurium activation becomes enhanced. Following this, at injection temperatures of 270°C nearly no differences in the growth kinetics between anion and cation injection are observed. However, at temperatures of 300°C the bend in the growth rate as well as narrower size dispersions are observed utilizing the cation injection. On the other hand, a deficiency of tellurium increases the quantity of oleic acid, due to protonation by phosphonic acids, this shortens the growth period and ripening processes occur earlier.

Additional control experiments undertaken with the exclusion of TDPA at 270°C result in QDs of higher quality within the initial stages, as depicted in fig. 4.12. Although cadmium oleate is known to act as a nucleation inhibitor, it is found to be the more reactive cation species in comparison to the corresponding phosphonate. These reactivity differences are ascribed to differences in the binding energies of fatty and phosphonic acids to the cadmium. Employing ab-initio calculations, facets of $Cd_{15}Se_{15}$ clusters, such as the $(000\bar{1})$ Cd facet.[18a] Their results show a much higher binding energy for phosphonic acids (1.12 eV), than for carboxylic acids

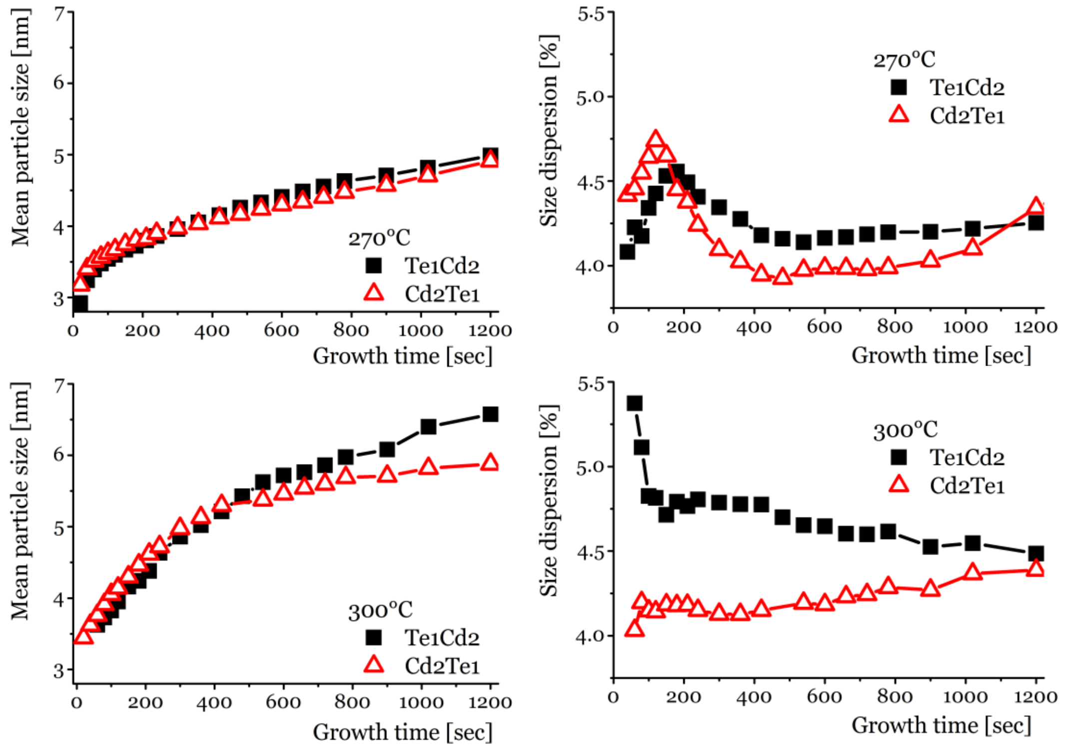

Figure 4. 11: CdTe growth kinetics and size dispersion under conditions of cadmium excess.

Comparison of anion (black squares) and cation injection (red triangles) at injection temperatures of 270°C (upper panels) and 300°C (lower panels).

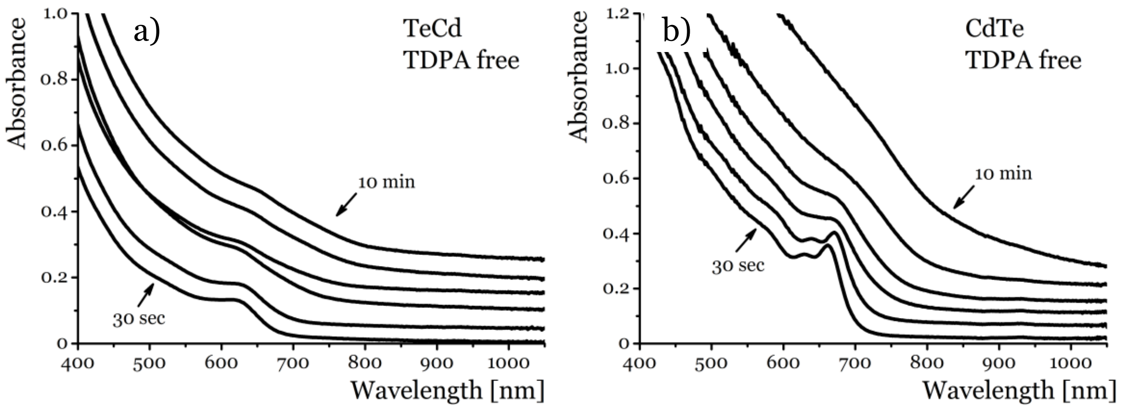

Figure 4. 12: Control experiments under exclusion of TDPA at 270°C.
TDPA free synthesis following the a) anion and b) cation injection pathway.

Puzder et al. studied the binding energies of fatty and phosphonic acids to different (0.68 eV) at the same Cd facet. These results have been further supported in a DFT study of ligand binding to different CdSe single crystal surfaces by Rempel et al. which revealed that phosphonic acids possess the highest binding strength to the non-polar (11$\bar{2}$0) CdSe and polar (0001) Cd facets.[18b]

Furthermore, the TDPA-free experiments (cf. fig. 4.12) suggest, that the small amounts of impurities of technical grade TOPO are sufficient to either deactivate the cadmium by increasing its stability (anion injection) or activate the tellurium (cation injection).

v. Summary

In summary, altering the injection pathway by means of the cation injection, under certain conditions nucleation and growth can be significantly affected. Thus, QD ensembles with narrow size distributions and improved emission properties are accessible, when utilizing the injection of a weakly stabilized cation species, e.g. by carboxylates, into a solution of activated anion species and the presence of strong cation stabilizers, e.g. phosphonates. Besides this defined combination of precursor species and stabilizing ligands, the reaction temperature influences the nucleation event. Under conditions of lowest reactivity, the smallest particle species are detected and identified as magic-sized clusters with a diameter of 1.8 nm.

4.3. CdTe magic-sized clusters and their mechanistic role

As mentioned above, at injection temperatures of 270°C magic-sized clusters are obtained and the QD growth is accompanied by a decline in the concentration of these MSCs. As those clusters are the smallest detectable particle species their influences on nucleation and QD growth require investigation.

However, mechanistic studies are intensively undertaken utilizing cadmium chalcogenide QDs. Therefore, different models for the contribution of the MSCs to nucleation as well as QD growth are to be considered here. As such, the MSCs may represent the critical size and the subsequent QD growth could proceed from these MSCs as nuclei either by a discontinuous mechanism which is characterized by additional red shifted MSC features, by monomer deposition or a combination of both. Finally, a further mechanism that may be applied here is that of MSC dissolution to form free monomers.

i. MSCs as critical nuclei

The mechanism suggests the MSCs to represent the smallest particle species and hence to exhibit a size which coincides with the critical radius. By means of the classical crystallization theory, all nuclei with sizes smaller then the MSCs dissolve and form free monomer, whereas all species with sizes equal to or larger than the MSCs start to grow.

This theory, *MSCs as criticl nuclei*, is proposed for CdS QDs obtained via a two-phase synthesis, where the precursors are provided in different phases.[10] There, the nucleation process is expected to proceed longer in comparison to one-phase syntheses and thus the MSCs are obtained with increasing population during the nucleation stage.[10a] Finally after reaching a maximum population, absorption features of the first excitonic transitions of QDs become obvious with decreasing MSC concentrations, indicating the growth stage. The MSCs are denoted as critical nuclei and their growth is proposed to progress by monomer deposition onto the surface following a forward-tunneling mechanism.[4, 10]

According to this, a continuous increase in the QD concentration is possible, whereas the MSC concentration declines. The main difficulty for the comparison of the data arises from the way in which the concentrations are obtained. The concentrations cannot be calculated following the procedure by de Mello Donegá,[24] as two particle species are present, namely MSCs and QDs. Additionally, the molar extinction coefficient of the MSCs is not known. However, the concentrations of CdTe MSCs and QDs are estimated using the absorbance at 445 nm, following a principle suggested by Jiang et al. as depicted in fig. 4.13 a. Comparing the obtained

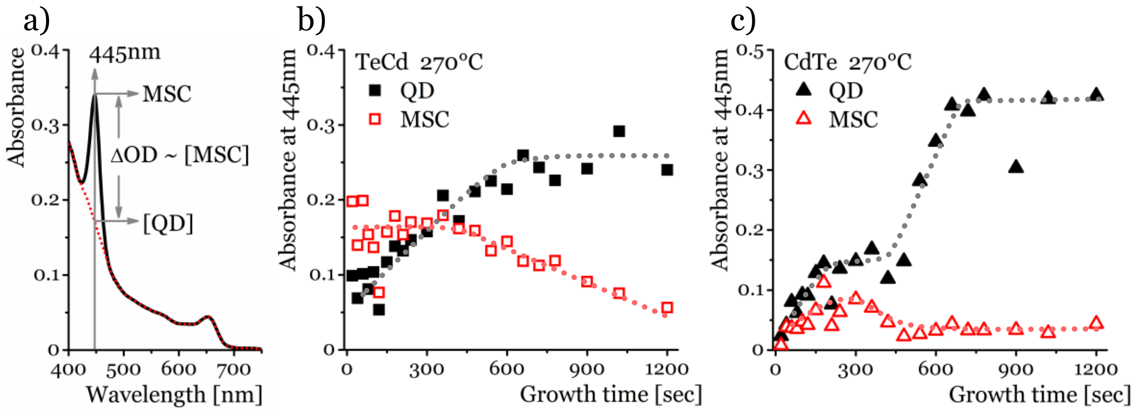

Figure 4. 13: Kinetics of the MSC and QD features for altered injection pathways indicate no direct association between MSCs and QDs.
a) Principle for determination of the MSC and QD concentrations at a wavelength of 445 nm. The obtained values are proportional to the corresponding MSC concentration.[11]
Concentration data for MSCs (red, open symbols) and QDs (black, filled symbols): comparison of (b) anion and (c) cation injection pathway.

concentration data shown in fig. 4.13 b and c, it is significant that MSCs and QDs are simultaneously detected from the beginning. This simultaneous occurrence of MSCs and QDs seems likely as during the one-phase hot injection synthesis a rapid nucleation burst occurs, while at these high temperatures an overlap of nucleation and growth is enabled.[10b] This is supported by the increasing number of QDs during the reaction, which is in contradiction to the typical observations for hot injection syntheses.[23a, 25]

Furthermore, the MSC concentration-related absorbance never exceeds that of the QDs by a factor larger than two and the rate of depletion of the MSCs is lower than the rate of QD formation. Consequently it can be assumed that the number of MSCs and their depletion rate is too low as the MSCs could represent the nuclei species of the present system. On the other hand, a continuous formation of MSCs and subsequent consumption due to QD growth could not be detected by the *aliquot technique* employed here, although the aliquots are subsequently quenched after sampling. Thus, it is assumed that the MSCs represent the critical size and QD formation is induced by either the fusion of multiple units of the MSCs or monomer deposition on the MSCs surface.[4, 10b, 26]

As the features of the CdS two-phase synthesis are somehow similar to the evolution of the absorption spectra presented in fig. 4.5, one could assume that the MSCs represent the critical size. However, the most striking discrepancy is the proposed delayed appearance of the QD feature, as within the study presented here it is already observed in the early stages of the reaction.

ii. Particle growth from MSCs as nuclei

There are two main possibilities for QDs to grow starting from MSCs. One is growth via MSC coalescence where MSCs form aggregates consisting of several MSCs. The further particle growth is then suggested to occur by the attachment of the smallest MSCs and their incorporation into the larger QD crystals. This mechanism is suggested for CdTe QDs made in aqueous solution, where complicated complexes of Cd and Te as precursors are formed and the growth proceeds slowly due to the limited reaction temperature.

A second possibility is a discontinuous growth mechanism. There, the MSCs grow via different stable sizes appropriate to fig. 4.1. Either by monomer deposition or MSC coalescence larger MSCs with a defined closed-shell structure are formed. Intermediate species with sizes between two successive MSCs are thermodynamically unstable and quickly dissolve or grow by reaching a size exhibiting a thermodynamically stable composition. This mechanism is found for different semiconductor materials at low reaction temperatures. It is important to mention that at a certain size the MSCs merge into continuous growth of QDs, indicated by the continuous red shift of the first absorbance maximum. As this growth mechanism represents a continuous decrease in chemical potential it is denoted as forward-tunneling.

The applicability of such a mechanism to the present study is doubtful as under the conditions employed here, only the absorbance of one cluster species localized at around 445 nm was determined, although a number of various clusters have been reported for CdTe. Clusters with absorbance peak positions (±5 nm deviation), at 445 or 450 nm as well as 315, 425, 460 and 500 nm have been reported for aqueous syntheses and 420, 435, 445, 485 and 505 nm for organic approaches.[7b, 8b, 14e, 14i, 27] Although only one cluster is visible within the absorption spectra, a discontinuous contribution of the MSCs to the overall QD growth cannot be excluded. If the initial growth period, with regard to MSC growth, follows a discontinuous mechanism one would expect a signature for the formation of a second cluster whose absorbance appears at longer wavelengths. Besides the “445 nm cluster” Zanella et al. found two additional cluster peaks at 488 nm and 506 nm which they refer to as a second and third species within a discontinuous growth process at 130°C.[7b] Due to the absence of these features in the present case one can assume that the growth process observed for the MSCs does not include a discontinuous period based on the fusion of the 445 nm clusters as during the reaction their concentration depletes but without the expected appearance of larger cluster families at longer wavelengths. Nevertheless, Zanella et al. attribute such a spectral evolution as depicted in fig. 4.5 to discontinuous growth. The most striking observation is the slow decrease in the MSC population in contrast to the quick particle growth as indicated by the decreasing peak intensity at 445 nm as well as the red shifted first absorbance maximum, respectively. For support of this theory, single particle studies need to be

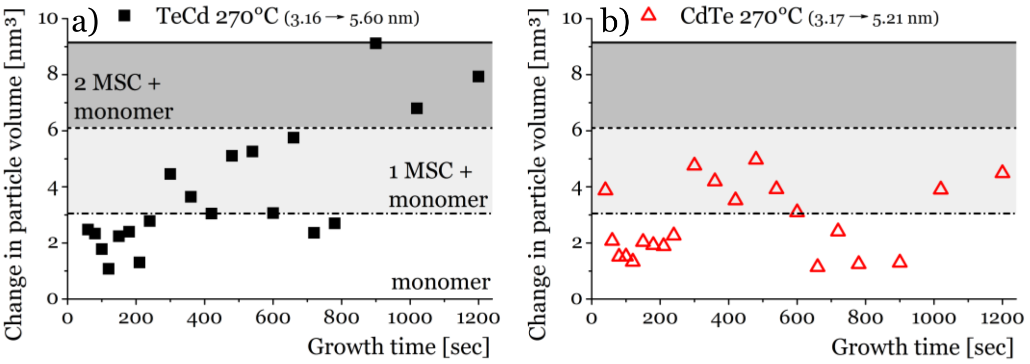

Figure 4. 14: Changes in particle volume indicate random monomer deposition. Calculated by subtraction of the consecutive particle volumes: $\Delta V_{ij} = V_j - V_i$; $i \geq 1$; $j = i + 1$; $i, j \in \mathbb{Z}$. The volume of the MSC species as well as its 2nd and 3rd multiple are shown as grey colored dash-dotted, dashed and solid line, respectively. First and final particle diameters as determined using the first absorbance maxima are given in brackets.

performed similar to the examinations by Zheng et al. for platinum NCs.[28] In the present study this was of necessity limited due to the small size of the MSCs with respect to the contrast of electron microscopes.[8c, 21]

However, simple evaluation of the volume changes for the given particle sizes results in random volume differences. Assuming an overall particle growth via coalescence of the cluster species as well as by monomer deposition the particle volume is expected to increase by at least one cluster unit with a theoretical volume of 3.05 nm³ (d = 1.8 nm). As presented in fig. 4.14, QD volume changes may occur via

- monomer deposition only: white area;
- coalescence of QDs and MSCs: dash-dotted, dashed and solid lines represent the volume of 1, 2 and 3 MSCs, respectively; and
- coalescence of QDs and MSCs accompanied with the deposition of monomers (light and dark grey areas).

The first data points within fig. 4.14 (growth time up to 300 s) show a volume change smaller than the unit cluster volume. Following these results, evidence for the exclusion of the particle growth via coalescence is assumed but not entirely ruled out. Therefore, within ensemble measurements each QD has to incorporate one MSC at the same time, otherwise single particle studies are required to definitely exclude discontinuous growth.

iii. MSCs dissolution to free monomer

A further mechanism that involves the appearance and disappearance of MSCs is that proposed by Jiang et al. for the synthesis of CdSe quantum rods.[11] Here the assumption is that the MSCs are not related to the stepwise formation of the quantum dots but are in equilibrium with the monomer species. This equilibrium is shifted in the direction of monomer formation due to a faster rate constant for the MSC dissolution. In accordance with fig. 4.1 this dissolution is attended with an increase in chemical potential and hence is denoted as backward-tunneling. As this increase in chemical potential is to be associated with the monomer concentration in solution, a decrease in the monomer concentration due to QD growth benefits the MSC dissolution. A crucial argument within this mechanism is the crystal structure of the MSCs and the resulting QDs. Following this, CdSe MSCs exhibit a zinc blende structure, whereas cadmium chalcogenide nanorods possess wurtzite modification.[4, 11] The preference of the zinc blende structure originates in the lower chemical potential in comparison to the wurtzite crystal structure.[8b, 26]

As the dissolution of the MSCs is an ongoing process, which is independent of the QD growth rate, the MSC species disappears with a sudden loss, as depicted in fig. 4.7 a. Therefore, absorbance values are considered as they exhibit direct proportionality to particle concentration. Hence, MSC concentrations [MSC], are estimated using the absorbance of the MSCs at the respective absorption wavelength. For correction the baseline absorbance of the QDs is subtracted, which itself is proportional to the QD concentration. The procedure to determine the absorbance value of the MSC feature as related to the concentration of MSCs and QDs is depicted in fig. 4.13 a.

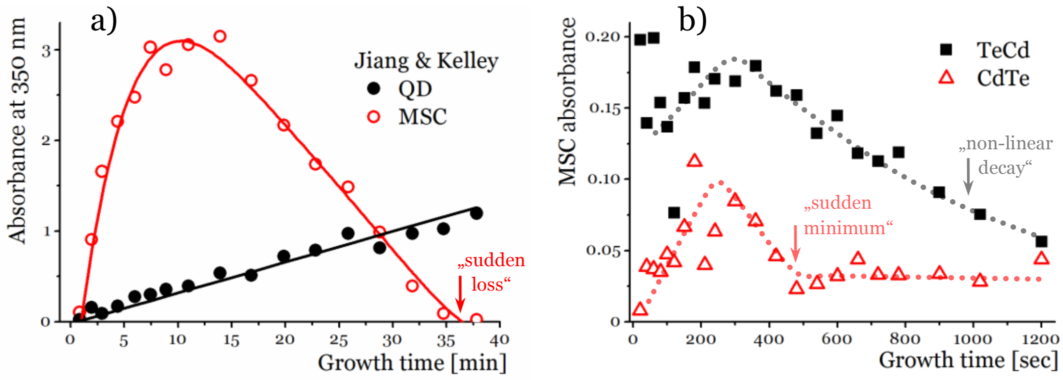

Figure 4. 15: Kinetics of the MSC population in accordance with the theory of Jiang & Kelley is not applicable to the present CdTe QD syntheses.
a) Evolution of the MSC peak (red, open circles) and the corresponding 350 nm baseline (black, filled circles) for CdSe nanorod synthesis and their simulated curves (lines). Reproduced from ref. [11] b) MSC concentration evolution as derived from the raw data absorbance feature at 445 nm.

Following the argumentation of Jiang et al., the MSC disappearance is primarily determined by their dissolution to form monomers. Otherwise, if the reaction of the MSCs with monomers were to control the rate of MSC depletion, the rate should slow as the concentration of one reactant species decreases. Experimentally higher monomer concentrations compared to that of MSCs are supposed and consequently the rate of MSC depletion would decrease with preceding MSC loss.

The data observed for an injection temperature of 270°C are shown in fig. 4.15 b. For both injection pathways an increase in MSC population is observed. In contrast to the mechanism of Jiang et al. the decrease in the MSC concentration does not end in a sudden loss. However, within the cation injection a "sudden minimum" is reached, whereas for the anion pathway a MSC depletion that follows a non-linear decay is observed. It is important to mention, that within the cation injection pathway the MSC minimum concentration is somehow related to the "bend" in the QD growth rate.

For further investigation of the backward-tunneling mechanism the MSC features derived from varied Cd-to-Te-ratio are considered. As shown in fig. 4.16, utilizing an excess of cadmium a second MSC feature at 365 nm (with a potential second transition at 346 nm) is obtained, whose evolution is related to that of the "445 nm species".

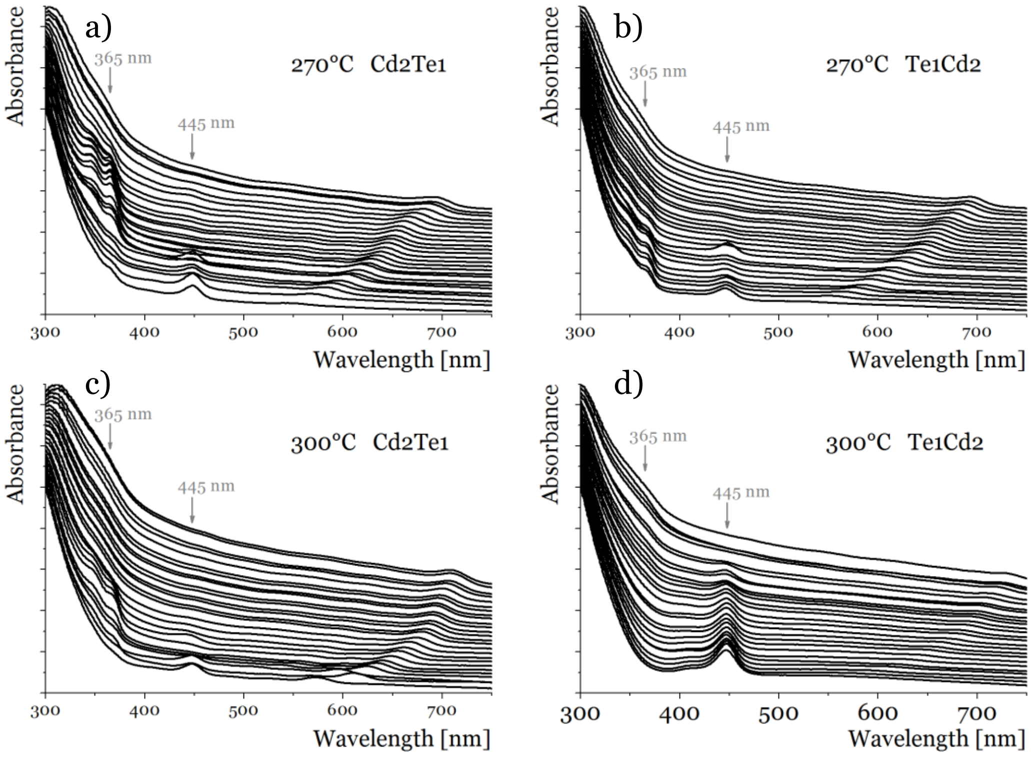

Figure 4. 16: The temporal evolutions of the raw data absorption spectra for syntheses utilizing an excess of cadmium indicate a second MSC species at 365 nm.

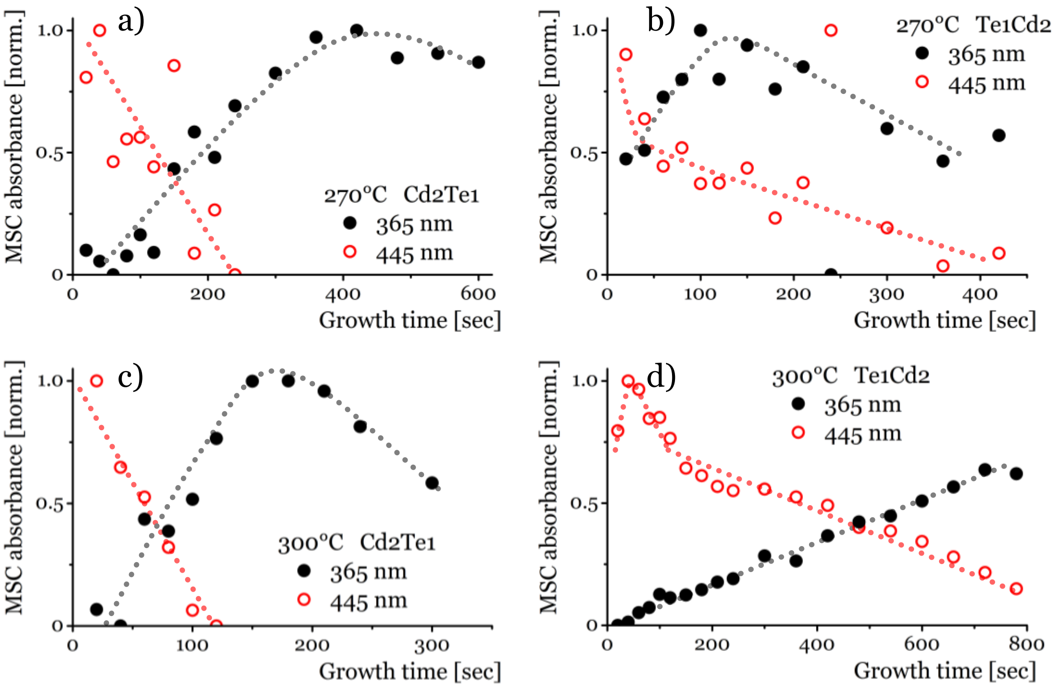

Figure 4. 17: The temporal evolutions of the MSC absorbance features reveal that the decline of the 445 nm species is attended with an increase of the 365 nm population.

From fig. 4.17 it is significant, that these smaller clusters form when the larger ones at 445 nm disappear. Furthermore, for the cation injection pathway it is obvious that the decrease of the 445 nm population and the increase of the 365 nm population occur with nearly similar rates. Subsequently, in the course of the reaction the smaller 365 nm clusters also disappear. This process indicates the possibility of a reverse discontinuous mode for the dissolution of the MSC species via an additional MSC family ($MSC_{445\,nm} \rightarrow MSC_{365\,nm} \rightarrow$ monomer). This would support the role of the MSCs following a backward-tunneling mechanism and hence acting as a monomer reservoir as proposed by Jiang et al.[11]

iv. Conclusion

Finally, it is apparent that MSCs have an unambiguous impact on the QD formation. However, their explicit role is not clearly identifiable within ensemble measurements. Therefore *in situ* spectroscopy or single particle studies are required in order to overcome these limitations and to get a deeper understanding.

Despite this, the findings presented here suggest the MSCs represent the critical nuclei as they exhibit the smallest detectable particle size, judging from the absorption spectra. The subsequent growth of the particles is attributed to be initiated by a forward-tunneling of the MSCs either by coalescence of the MSCs amongst each other, the deposition of monomer material onto the surface of the MSCs or a combination of both.[4, 10b] However, as quantum dots growth proceeds, the MSCs are suggested to disappear via their dissolution to monomer material.

v. Proposed mechanism for the MSC disappearance

As the MSCs are atomic ensembles, and may be considered as a closed shell species with a defined number of cadmium and tellurium atoms, they are considered to be relatively inert with respect to further monomer deposition. However, cluster dissolution is not strictly prohibited but rather strongly depends on kinetic parameters e.g. monomer concentrations. As suggested by Peng et al. with high monomer concentrations a forward-tunneling (MSC → QD) results, whereas with decreasing monomer concentrations a reverse pathway (backward-tunneling) is favored (MSC → monomer).[4] Following this theory, in the presence of a deficiency of cadmium the forward-tunneling process proceeds at faster rates. This is indicated by the nonappearance rather than the quick disappearance of the MSC features at 445 nm as depicted in fig. 4.18. On the other hand, under conditions of an excess of cadmium the MSC lifetime is prolonged and additional MSC features at shorter wavelengths appear, revealing the presence of backward-tunneling (cf. fig. 4.16).

Reasonable explanations for these effects are related to the MSC structure. The Cd atoms on the outer shell are assumed to be stabilized by phosphonic acid molecules. Thus, no MSC species are observed within syntheses that do not use phosphonic acids.[8b] This is supported within the present study by the TDPA-free experiments at injection temperatures of 270°C, as depicted in fig. 4.12. However, utilizing a deficiency of cadmium, which is related to an excess of the tellurium precursor, enables the possibility for an exchange of the surface ligands by the TOP-Te complex. This resembles the structural observations of magic-sized clusters obtained within aqueous syntheses.[15, 29] There the clusters exhibit an intrinsic excess of cadmium, whereas the anion content is balanced by respective chalcogenide containing stabilizing molecules on the outer shell. However, addition of tellurium to the outer shell using TOP-Te represents a deviation from the ideal cluster

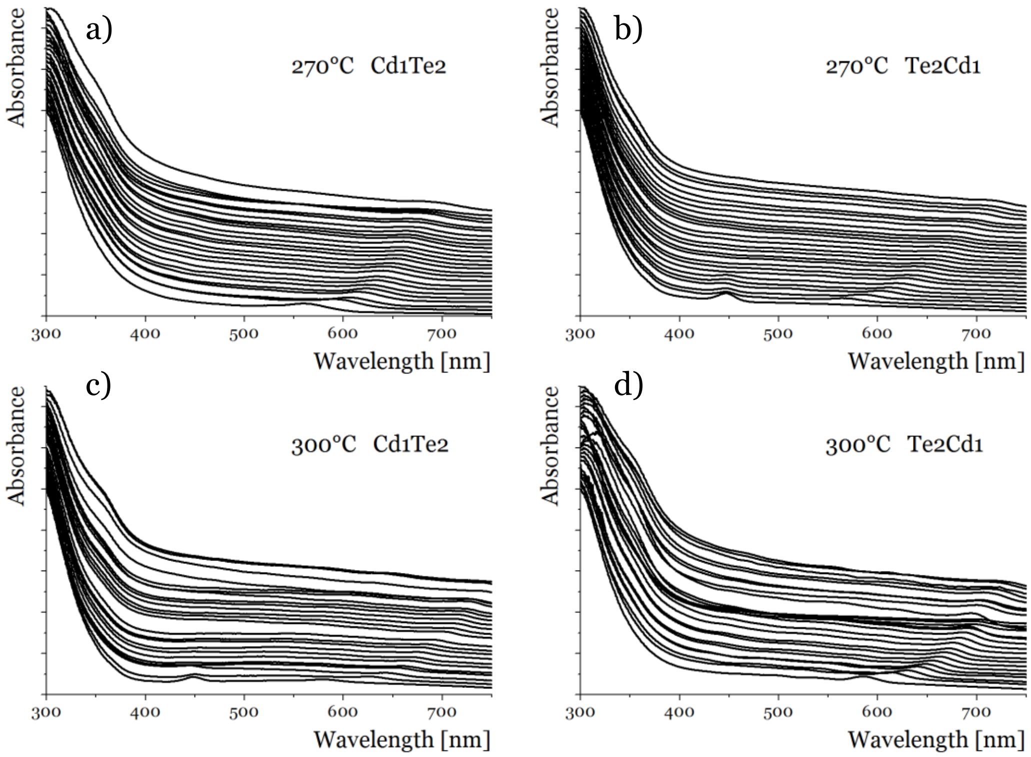

Figure 4. 18: The temporal evolutions of the raw data absorption spectra for syntheses utilizing a deficiency of cadmium indicate the nonappearance rather than the quick disappearance of the MSC species at 445 nm.

configuration attended with an increase in the chemical potential.[8c] Consequently, the thermodynamic stability of the MSCs is decreased and the possibility of forward-tunneling by means of further growth or coalescence is raised.

On the other hand, a deficiency of tellurium is suggested to be consumed within the formation of monomer material [Cd-Te] due to the excess of cadmium. Hence, there is no free TOP-Te present and thus a tackling of the MSCs by TOP-Te is prohibited and the clusters show prolonged thermodynamic stability. Similar observations are made by Dagtepe et al. for CdTe MSCs prepared from dimethyl cadmium.[26] Nevertheless, backward-tunneling is observed, indicated by a blue shifted, permanent absorbance feature representing MSCs of a smaller size (cf. fig. 4.16). This effect is attributed to the process of Ostwald ripening, which simply means that the QDs grow at the expense of the MSCs with an absorbance maximum at 445 nm. By means of a reverse discontinuous growth mode, the smaller, thermodynamically stable clusters (with an absorbance maximum at 365 nm) are formed by equilibrating the non-ideal configuration obtained due to the removal of surface atoms.

4.4. Summary

Within the present synthesis study, the injection pathway is altered and the growth kinetics are evaluated. Therefore, as a function of growth time the particle sizes with the corresponding size dispersions as well as the concentrations of the QDs and the monomeric cadmium are considered.

Thus, altering the injection pathway by means of the cation injection, under certain conditions nucleation and growth can be significantly affected. Therefore a reaction is utilized where a weakly stabilized cation species, e.g. by carboxylates, is injected into a solution of activated anion species and the presence of strong cation stabilizers, e.g. phosphonates. A kind of cation activation is proposed by the use of a relatively reactive cation species which initially is separated spatially from the strong binding phosphonic acid ligands. On the other hand anion activation is suggested to occur via the oxidation of the stabilizing ligands (TOP). Due to a nucleophilic attack by free phosphonic acid molecules the stability of the TOP-Te complex is decreased under formation of cation stabilizing species.

For this, a change in the growth mode is observed which can be associated with the passing into the Ostwald ripening regime. Evidence is given by i) reaching an equilibrium monomer concentration, ii) the beginning of a decrease in the particle concentrations, and iii) a broadening of the respective size dispersions. Mechanistically the process of Ostwald ripening is suggested to proceed via free phosphonic acids, as they are able to reversibly ripen particles. Furthermore this kind of injection is attended with increased nucleation reactivity. This is emphasized by distinct first absorbance maxima that appear in the initial stages of the reaction (20 s growth time), indicating a fast nucleation event with fast subsequent growth.

The obtained results are supported by a study where the Cd-to-Te-ratio is varied. There, utilizing a deficiency of cadmium increases the TDPA-to-Cd-ratio which results in a wider final size distribution by means of ripening. However, increasing the TDPA-to-TOP-ratio by using deficiencies of tellurium the tellurium activation becomes enhanced and due to increased quantities of oleic acid the growth period is shortened and ripening processes occur earlier.

In summary, CdTe QD ensembles with narrow size distributions and improved emission properties are accessible by injection of cadmium oleate into a solution of TOP-tellurium activated by phosphonic acid molecules. Besides this defined combination of precursor species and stabilizing ligands, it is found that the reaction temperature influences the nucleation event. Under conditions of lowest reactivity at injection temperatures of 270°C, within the beginning of the reaction the smallest particle species are detected and identified as magic-sized clusters with a diameter of 1.8 nm. During the proceeding growth smaller clusters appear utilizing an excess of cadmium. The formation of these smaller clusters is attributed to Ostwald ripening. However, the largest obtained MSCs with a distinct absorbance maximum at 445 nm are assumed to represent the critical size and subsequent QD formation is assumed to be induced by either the fusion of multiple units of the MSCs or monomer deposition on the MSCs surface. It is observed that the QD growth is attended with a decrease in the MSC absorbance peak intensity indicating a decline in the MSC population. However, a slow decrease in the MSC population in contrast to a quick particle growth leads to the result that the MSC disappearance is primarily determined by their dissolution to form monomers. Additionally, random volume changes smaller than the cluster volume for given particle sizes allow the exclusion of a discontinuous growth period.

Evidence for the proposed mechanisms derives from various Cd-to-Te-ratios. As mentioned above, utilizing an excess of cadmium a second MSC feature at 365 nm is obtained. Furthermore, it is observed that with nearly similar rates these smaller clusters form when the larger ones at 445 nm disappear. Later in the course of the reaction the smaller 365 nm clusters also disappear. The features of this process indicate a reverse discontinuous mode for the dissolution of the MSC species via an additional MSC family. Here, the smaller, thermodynamically stable clusters are formed by equilibrating a non-ideal configuration obtained due to the removal of surface atoms of the larger MSCs.

Mechanistically the disappearance of the MSCs either by growth or dissolution is explained by the structure of the MSCs. Therefore, these species that possess a closed-shell structure are assumed to be stabilized by phosphonic acid molecules. If an excess of tellurium is used within the synthesis, the phosphonic acid ligands are replaced by TOP-Te units. This addition of a tellurium layer forms a cluster which represents a deviation from the ideal cluster configuration and hence further growth is enabled. However, the dissolution is thermodynamically forced by the decreasing monomer concentration and can simply be explained by the process of Ostwald ripening.

4.5. Equations and calculations

i. Mean particle size

For determination of the mean particle size, d, an empirical formula is applied utilizing the first absorbance maximum, λ, as derived by Yu et al.[30] The applicability of this equation is validated in chapter A in the Appendix.

Accordingly the mean particle diameter is calculated from:

$$d = (9.8127 \cdot 10^{-7}) \cdot \lambda^3 - (1.7147 \cdot 10^{-3}) \cdot \lambda^2 + 1.0064 \cdot \lambda - 194.84$$

ii. QD concentration

For calculations of the QD concentrations the molar extinction coefficient is considered as is experimentally determined by Yu et al.[30] Therefore, the first absorbance peak is utilized to determine size as well as molar extinction coefficient. In combination with the Lambert-Beer law the particle concentration in the cuvette and the flask can be calculated.

(a) Lambert-Beer law:

$$Abs_{1^{\mathrm{st}}} = \varepsilon_{1^{\mathrm{st}}} \cdot c_{QD} \cdot L$$

With $Abs_{1^{\mathrm{st}}}$ the absorbance at the first absorbance maximum; L the pathlength of the light in the cuvette, $L = 1cm$; $\varepsilon_{1^{\mathrm{st}}}$ the molar extinction coefficient of the particular QDs; and c_{QD} the QD concentration.

(b) Molar extinction coefficient at the first absorbance maximum (in $\mathrm{M^{-1} \cdot cm^{-1}}$):[30]

$$\varepsilon_{1^{\mathrm{st}}} = 10043 \cdot \mathrm{d}^{2.12}$$

With d the particle diameter as determined following the procedure validated in Appendix B.

(c) mean QD concentration:

$$\langle c_{QD} \rangle = \frac{Abs_{1^{\mathrm{st}}}}{\varepsilon_{1^{\mathrm{st}}} \cdot L} \cdot \frac{V_{cuvette}}{V_{aliquot}}$$

iii. Monomeric cadmium concentration

The monomeric cadmium concentration, [Cd], includes the amount of Cd^{2+} free in solution and consumed for the MSC formation. Hence, it represents the difference between the starting concentration ($[Cd]_0$ = 23 µM) and the Cd^{2+} concentration consumed for the formation of the QD ensemble (c_{Cd}) inside the reaction flask.

(a) Cadmium concentration incorporated into the QD ensemble:

$$c_{Cd} = c_{QD} \cdot N_{Cd/QD} = \langle c_{QD} \rangle \cdot \frac{4 \cdot V_{QD}}{V_{UC}}$$

Where $N_{Cd/QD}$ is the number of Cd atoms per QD.

(b) Monomeric cadmium concentration:

$$[Cd] = [Cd]_0 - c_{Cd}$$

iv. Size dispersion

The size dispersion, ξ, is a measure of the particle size distribution and derives from a Gaussian fit of the first absorbance maximum, assuming a Gaussian distribution of the particle size. Finally the size dispersion is calculated using the resulting parameters, namely the standard deviation of the Gaussian distribution, w, and the position of the peak maximum, x_c, representing the average particle radius.[31] The relative size dispersion, $\tilde{\xi}$, considers the corresponding mean particle radius.

(a) Gaussian fit function:

$$y = y_0 + \frac{A}{w\sqrt{\pi/2}} exp\left(-2\frac{(x-x_c)^2}{w^2}\right)$$

(b) Size dispersion:

$$\xi = \frac{w}{x_c}$$

(c) Relative size dispersion:

$$\tilde{\xi} = \frac{\xi}{2 \cdot r} = \frac{\xi}{d}$$

4.6. References

[1] a) V. K. LaMer, R. H. Dinegar, *Journal of the American Chemical Society* **1950**, *72*, 4847; b) C. B. Murray, C. R. Kagan, et al., *Annual Review of Materials Science* **2000**, *30*, 545; c) K. Yu, M. Z. Hu, et al., *The Journal of Physical Chemistry C* **2010**, *114*, 3329.

[2] T. Sugimoto, *Advances in Colloid and Interface Science* **1987**, *28*, 65.

[3] a) I. M. Lifshitz, V. V. Slyozov, *Journal of Physics and Chemistry of Solids* **1961**, *19*, 35; b) C. Wagner, *Zeitschrift für Elektrochemie, Berichte der Bunsengesellschaft für physikalische Chemie* **1961**, *65*, 581; c) M. Kahlweit, *Advances in Colloid and Interface Science* **1975**, *5*, 1.

[4] Z. A. Peng, X. Peng, *Journal of the American Chemical Society* **2002**, *124*, 3343.

[5] a) X. Peng, J. Wickham, et al., *Journal of the American Chemical Society* **1998**, *120*, 5343; b) D. V. Talapin, A. L. Rogach, et al., *The Journal of Physical Chemistry B* **2001**, *105*, 12278.

[6] a) C. H. Fischer, H. Weller, et al., *Langmuir* **1989**, *5*, 429; b) N. Herron, J. C. Calabrese, et al., *Science* **1993**, *259*, 1426; c) T. Vossmeyer, L. Katsikas, et al., *The Journal of Physical Chemistry* **1994**, *98*, 7665; d) S. F. Wuister, F. v. Driel, et al., *Physical Chemistry Chemical Physics* **2003**, *5*, 1253; e) A. Kasuya, R. Sivamohan, et al., *Nature Materials* **2004**, *3*, 99.

[7] a) S. Kudera, M. Zanella, et al., *Advanced Materials* **2007**, *19*, 548; b) M. Zanella, A. Z. Abbasi, et al., *The Journal of Physical Chemistry C* **2010**, *114*, 6205.

[8] a) R. Xie, Z. Li, et al., *Journal of the American Chemical Society* **2009**, *131*, 15457; b) P. Dagtepe, V. Chikan, et al., *The Journal of Physical Chemistry C* **2007**, *111*, 14977; c) H. S. Chen, R. V. Kumar, *Crystal Growth & Design* **2009**, *9*, 4235.

[9] M. Sun, X. Yang, *The Journal of Physical Chemistry C* **2009**, *113*, 8701.

[10] a) D. Pan, X. Ji, et al., *Chemistry of Materials* **2008**, *20*, 3560; b) Q. Yu, C.-Y. Liu, *The Journal of Physical Chemistry C* **2009**, *113*, 12766.

[11] Z.-J. Jiang, D. F. Kelley, *ACS Nano* **2010**, *4*, 1561.

[12] H. Liu, J. S. Owen, et al., *Journal of the American Chemical Society* **2007**, *129*, 305.

[13] J. S. Steckel, B. K. H. Yen, et al., *Journal of the American Chemical Society* **2006**, *128*, 13032.

[14] a) Z. A. Peng, X. Peng, *Journal of the American Chemical Society* **2000**, *123*, 183; b) W. W. Yu, Y. A. Wang, et al., *Chemistry of Materials* **2003**, *15*, 4300; c) D. V. Talapin, S. Haubold, et al., *The Journal of Physical Chemistry B* **2001**, *105*, 2260; d) S. F. Wuister, I. Swart, et al., *Nano Letters* **2003**, *3*, 503; e) Q. Dai, D. Li, et al., *Nanotechnology* **2007**, *18*, 405603; f) J. Kolny-Olesiak, V. Kloper, et al., *Surface Science* **2007**, *601*, 2667; g) J.-Y. Chang, S.-R. Wang, et al., *Nanotechnology* **2007**, *18*, 345602; h) D. Dorfs, T. Franzl, et al., *Small* **2008**, *4*, 1148; i) X.-Y. Qi, K.-Y. Pu, et al., *NANO* **2008**, *3*, 109; j) H. Zhong, M. Nagy, et al., *The Journal of Physical Chemistry C* **2009**, *113*, 10465; k) J. Wang, Y. Long, et al., *ChemPhysChem* **2009**, *10*, 680.

[15] J. Rockenberger, L. Tröger, et al., *The Journal of Chemical Physics* **1998**, *108*, 7807.

[16] a) J. Y. Rempel, M. G. Bawendi, et al., *Journal of the American Chemical Society* **2009**, *131*, 4479; b) J. van Embden, J. E. Sader, et al., *The Journal of Physical Chemistry C* **2009**, *113*, 16342.

[17] J. S. Owen, E. M. Chan, et al., *Journal of the American Chemical Society* **2010**, *132*, 18206.

[18] a) A. Puzder, A. J. Williamson, et al., *Nano Letters* **2004**, *4*, 2361; b) J. Y. Rempel, B. L. Trout, et al., *The Journal of Physical Chemistry B* **2006**, *110*, 18007.

[19] a) A. L. Efros, M. Rosen, *Physical Review Letters* **1997**, *78*, 1110; b) Y. Zhu, S. McKernan, et al., *Journal of Applied Physics* **2010**, *108*, 123104.

[20] M. Grabolle, M. Spieles, et al., *Analytical Chemistry* **2009**, *81*, 6285.

[21] W. W. Yu, Y. A. Wang, et al., *Chemistry of Materials* **2003**, *15*, 4300.

[22] G. Cao, V. M. Lynch, et al., *Chemistry of Materials* **1993**, *5*, 1000.

[23] a) C. R. Bullen, P. Mulvaney, *Nano Letters* **2004**, *4*, 2303; b) W. W. Yu, X. Peng, *Angewandte Chemie International Edition* **2002**, *41*, 2368.

[24] C. de Mello Donegá , R. Koole, *The Journal of Physical Chemistry C* **2009**, *113*, 6511.

[25] C. de Mello Donegá, P. Liljeroth, et al., *Small* **2005**, *1*, 1152.

[26] P. Dagtepe, V. Chikan, *The Journal of Physical Chemistry A* **2008**, *112*, 9304.

[27] a) P. T. K. Chin, J. W. Stouwdam, et al., *Nanotechnology* **2008**, *19*, 205602; b) A. Rogach, L. Katsikas, et al., *Berichte der Bunsengesellschaft für Physikalische Chemie* **1996**, *100*, 1772; c) A. D. Dukes, J. R. McBride, et al., *Chemistry of Materials* **2010**, *22*, 6402.

[28] H. Zheng, R. K. Smith, et al., *Science* **2009**, *324*, 1309.

[29] T. Vossmeyer, G. Reck, et al., *Journal of the American Chemical Society* **1995**, *117*, 12881.

[30] W. W. Yu, L. Qu, et al., *Chemistry of Materials* **2003**, *15*, 2854.

[31] V. C. S. Reynoso, Y. Liu, et al., *Journal of Materials Science Letters* **1996**, *15*, 1037.

5

Inorganic coating of CdSe and CdTe QDs

Surface passivation by means of capping by organic molecules as well as coating by inorganic shells represents an important and necessary tool to control chemical and physical properties. As the core and its surrounding shell determine mainly the physical, in particular optical properties, the organic shell defines the chemical properties, i.e. the solubility and hence colloidal stability of the quantum dots. Within this chapter, strategies of surface passivation by means of an inorganic coating with either the same or a different material are discussed. According to the requirements of applications, opportunities to tune sizes as well as emission properties are demonstrated. As bare core materials the CdSe and CdTe QDs utilized are prepared via the optimized syntheses of chapters 3 and 4, respectively.

Coating of QDs with inorganic shells provides the possibility to prepare particles with a high quantum yield as well as a high stability against photo-bleaching. The shell material may be grown epitaxial onto the QDs to achieve an improvement in the surface passivation. To obtain a successful covering, several requirements need to be fulfilled. The most important of these concerns the crystallographic properties: both core and shell materials need to crystallize in the same structure and possess a small lattice mismatch. Otherwise non-epitaxial growth modes may occur, ending up in hybrid or island formation,[1] or in the worst cases defects are introduced in terms of strains and ruptures.[2] Further requirements concern the precursor species used for the shell material, which has to show a high reactivity as well as selectivity to perform the intended coating reactions without self-nucleation and hence the formation of undesired byproducts.[3]

Succeeding in the challenge of core/shell formation opens a wide range of opportunities depending on the choice of core and shell material. Therefore, within the following sections, different kinds of core/shell and multishell heterostructures are introduced and their particular properties as well as synthesis behavior are discussed.

5. 1. Extra precursor addition

In the synthesis of QDs following the standard hot injection method particle sizes are limited by the concentration of the precursors. Thus an opportunity to increase the final particle size is via the addition of extra precursor solution. By means of a so called one pot approach, additional monomer material is supplied by injections of precursor solutions during the growth of the particles after homogeneous nucleation.

As described in chapter 2, the nucleation event controls the number of particles, whereas in the growth regime the type of reaction is determined by the monomer concentration. Hence, a high monomer concentration represents the reaction controlled regime, whereas after partial monomer depletion diffusion processes become more important and those determine the reaction. Characteristic features of the reaction and diffusion controlled growth regimes are a constant ($d\xi/dt = 0$) as well as a decreasing size dispersion ($d\xi/dt < 0$) with proceeding growth time, respectively. Hence, theoretically the diffusion controlled growth regime represents an optimal time window for the addition of extra precursor solution. The main requirement is a very slow injection to prevent an increase in monomer concentration resulting in a return to the reaction controlled growth regime. On the other hand, it is necessary that the monomer or precursor concentration in the reaction solution is not depleted before an extra precursor injection, to prevent Ostwald ripening associated with a broadening of the size distribution.

As an indication the size dispersion may be determined from the full width at half maximum (fwhm) of the photoluminescence peak, it represents an easily accessible parameter to determine the kind of growth regime present. This assumes the equality in the emission properties of the particles within the ensemble, as the fwhm of the PL peak represents the emitting fraction of particles.

i. CdSe/CdSe

To verify the above, within the synthesis of CdSe an extra precursor addition is investigated performing a continuous precursor injection starting in the diffusion controlled growth regime. The addition of the precursor solution is undertaken using a syringe pump to guarantee a constant precursor addition. The drawback of this method is the occurrence of occasional breaks in the addition of the precursor due to replacements of the precursor reservoirs. In addition, the influence of an intermittency in the growth process by a temperature decrease from 300 to 25°C and a temperature recovery after 10 hours is examined. For the injection a mixture of 0.08 mol/l cadmium oleate in ODE as well as 1 mol/l selenium in n-trioctylphosphine is utilized.

Fig. 5.1 presents TEM images of CdSe QDs after specific time intervals where, besides an increase in particle size, a broadening of the size dispersion is also observed. Experimentally, the injection of the extra precursor solution is started during a narrowing stage indicating the presence of the diffusion controlled growth regime, as depicted in fig. 5.2 b. Furthermore, to ensure a continuous monomer deposition the reaction temperature is increased in two steps, as monomer deposition requires a certain size dependent activation energy.[4] This slightly affects the size distribution, as well as the rate of deposition, whereas the overall growth rate is kept nearly constant (cf. fig. 5.2 a). The reason for these effects is the enhancement of the diffusion processes due to the temperature increase. As a result, ripening processes are induced, represented as a broadening in the size dispersion, as well as faster deposition rates due to an increased number of monomers at the surface of the particles.

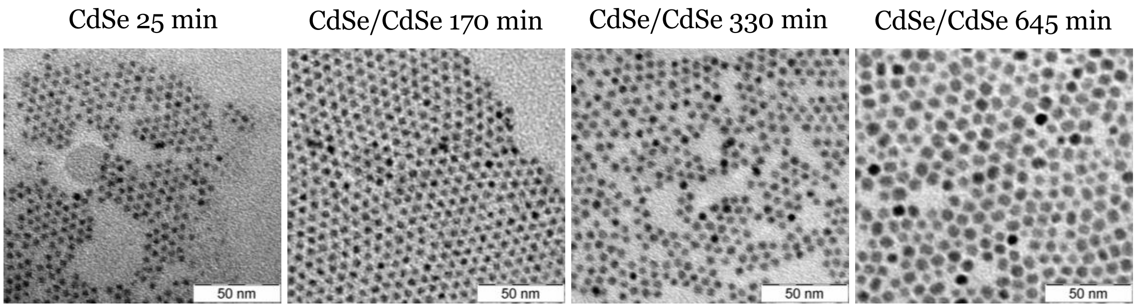

Figure 5. 1: TEM images of CdSe QDs obtained via extra precursor addition.
Different samples are taken during the growth process: core particles before an extra precursor injection (CdSe 25 min), as well as CdSe/CdSe core/shell particles at given times.

Furthermore, the constant deposition rate, indicated by the particle size evolution as well as PL position, overcomes a quick drop of the reaction temperature to 25°C and recovery after 10 hours (see fig. 5.2 a, c). This behavior opens the possibility to fine tune emission properties defined by particle sizes. Considering this opportunity, experimentally an iterative approach towards the final size is feasible by alternating quenching and reheating steps. Additionally, utilizing an intermediate cleaning step for precursor and monomer removal, those particles can be introduced into a similarly comprised reaction mixture followed by the addition of shell precursor material.

Beside significant broadening of the size dispersion (cf. fig. 5.2 b), the main disadvantage of this kind of seeded growth method is the huge decrease in the photoluminescence quantum yield, although the concentration of the precursor solution was very dilute (0.09 mol/l) and the addition proceeded slowly with 5.5 ml/h. As indicated by the intensity of the PL peak in fig. 5.2 d, contemporary with injection of additional Cd(oleate)$_2$ and TOP-Se, the PL intensity drops. Very at the end of the reaction, the temperature was lowered to about 190°C by the injection of 5 ml oleylamine. The aim of this temperature decrease was to induce annealing processes to achieve a recovery of the quantum yield. Actually, a slight increase of the PL intensity is observed in a short term annealing period. Consequently, the decrease in the reaction temperature, in contrast to the 2-step increase, is intended to decrease the growth rate due to smaller diffusion coefficients of the monomeric material. A weaker decrease in the quantum yield is observed by applying a deposition temperature of 270°C. For comparison of the two reaction temperatures 270°C and 300°C, the changes in mean particle size and PL intensity with reaction times are shown in fig. 5.3. These results derive from a fitting of the experimentally obtained data utilizing a linear increase as well as an exponential decay, respectively. The obtained differences in final PL intensity are attributed to the slower deposition rate, by which fewer defects are introduced.

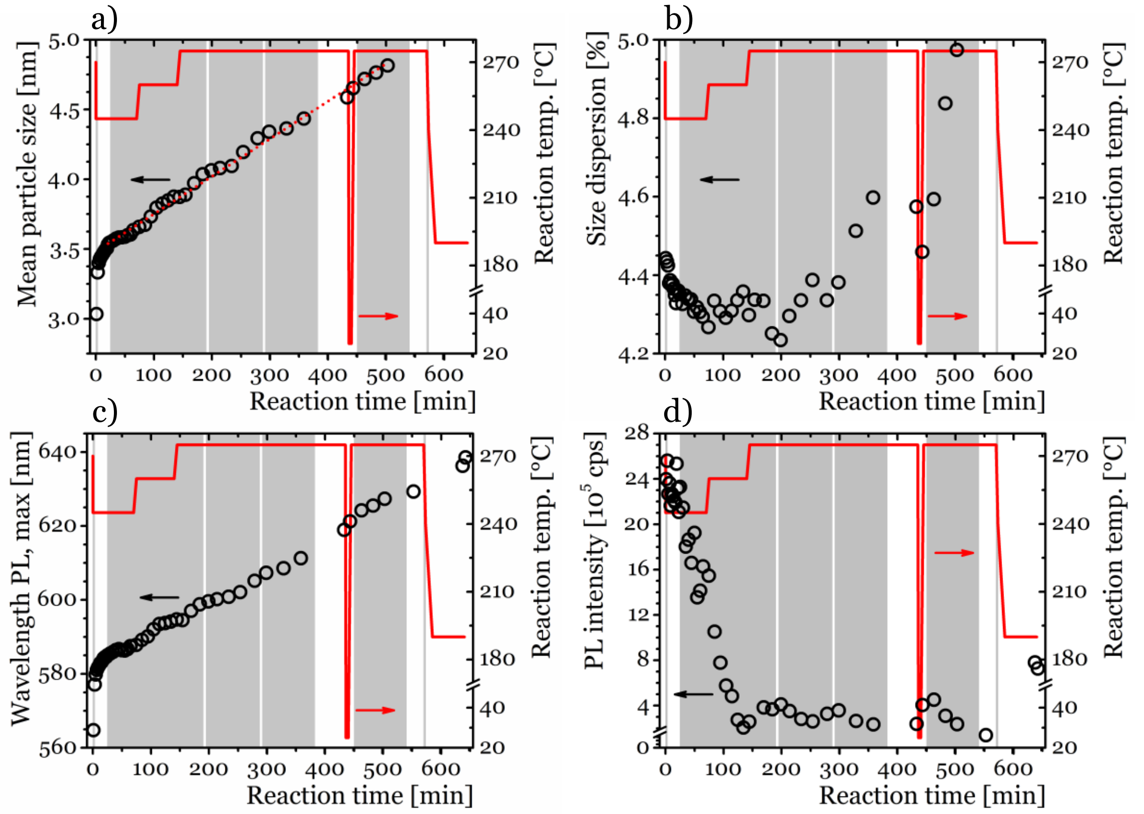

Figure 5. 2: By constant precursor addition a linear growth rate is suggested (size, PL), whereas the quality of the CdSe QDs gets worsened (dispersion, PL intensity).
Reaction temperature is shown as function of growth time (red solid line). Within its progression the minimum point at 25°C represents a reaction intermittency of approx. 10 hours, which is not taken into account on the time axis. Precursor injection is indicated as gray area.

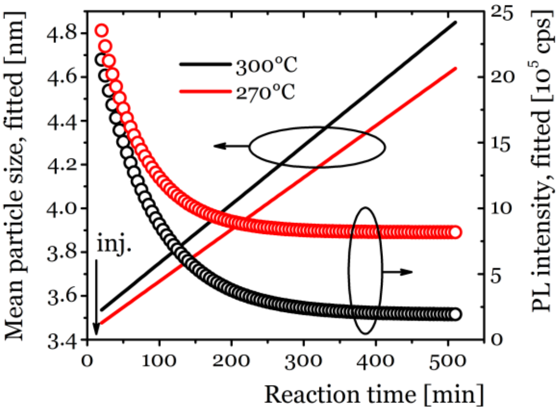

Figure 5. 3: Lowering the reaction temperature decreases the growth rate as well as results in higher PL intensities.
Comparison of reaction temperatures of 270°C (red) and 300°C (black). Data obtained by a linear fit (solid line, particle size) as well as an exponential decay fit (open circles, PL intensity).

ii. CdTe/CdTe

In contrast to the above mentioned slow injection of extra precursor solution, within the syntheses of CdTe QDs an additional precursor injection is investigated whereby quick injections of predetermined volumes are performed. In terms of this, the total amount of injection solution is kept constant, whereas the injection portions are varied and hence a single precursor injection is compared to a multiple precursor injection, independent of the growth regime. Experimentally, for the injection a mixture of 2 ml Cd-stock (0.09 mol/l) and 0.2 ml TOP-Te (1 mol/l) solutions are employed. The comparison is performed either as an injection of the total amount (1 x 2.2 ml) or as four injections (4 x 0.55 ml) with 5 minute intermittencies.

One main difference between both of these injection pathways is the appearance of a second particle ensemble for the one portion injection, shown within the contour plots in fig. 5.4. This second particle ensemble arises from homogeneous nucleation and due to the present diffusion controlled growth regime it results from a fast growth rate and hence runs into the main particle ensemble. Further differences become obvious upon examination of the progression of the mean particle sizes, the corresponding size dispersions as well as the height of the PL maxima associated with the quantum yield, as depicted in fig. 5.5. From these it is apparent that subsequent to a one portion injection, the mean particle size significantly and quickly increases, whereas following the four portion injection, no distinct changes are obvious. Additionally, during the single precursor addition parallel nucleation occurs, which leads to a large broadening of the size dispersion and a quick decrease in the PL intensity. Although the PL efficiency is also decreasing within the four portion pathway, it seems to be unaffected by each subsequent injection. Contrastingly, a significant effect is observed in the size dispersion: subsequent to

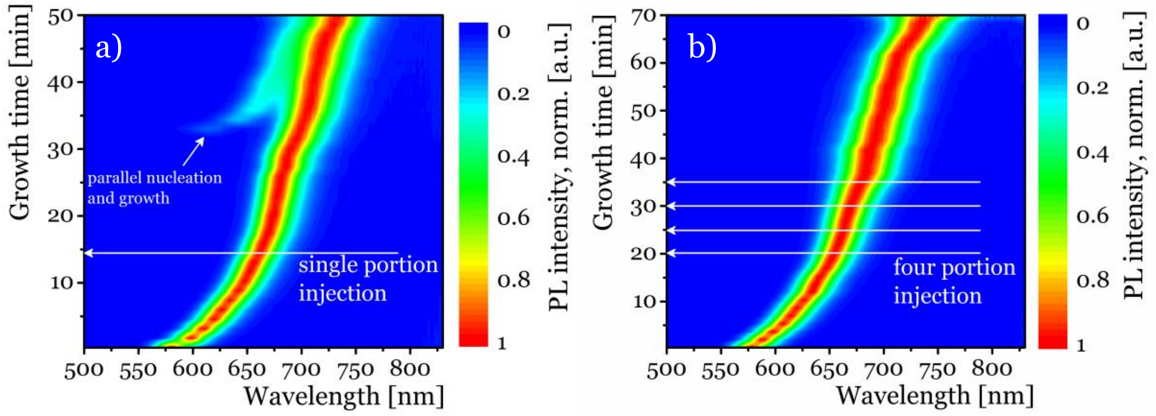

Figure 5. 4: Parallel nucleation may occur by quick injection of large amounts of precursor solutions, whereas small quantities prevent this process.
In total 2.2 ml of a Cd-Te-precursor mixture is introduced by quick injections: a) one and b) four injections. The points in time of the particular injection are indicated by arrows.

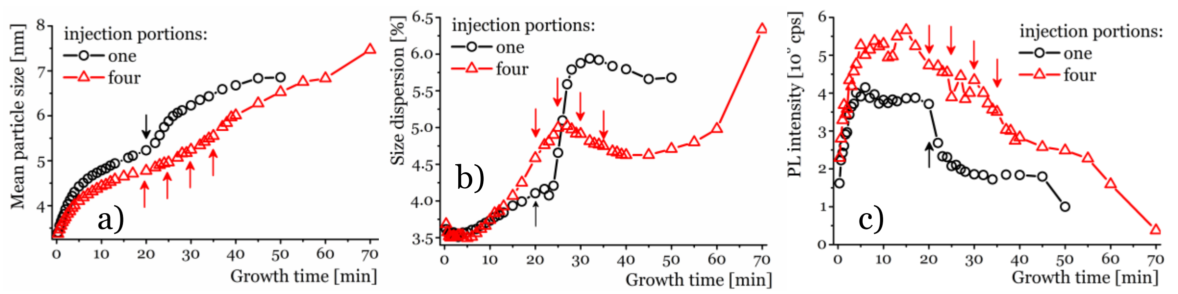

Figure 5. 5: Single injections of a large amount of extra precursor results in a decrease in the ensemble properties to a wider extent in comparison to multiple injections of small quantities.
a) Mean particle sizes, b) size dispersions, c) PL intensity for the two kinds of injection: one (black circles) and four portion (red triangles) injection. The points in time of the particular injection are indicated by arrows.

the second precursor addition, the size dispersion changes from a broadening into a narrowing regime (cf. fig. 5.5 b, red). The broadening regime is attributed to ripening processes due to fast monomer consumption. The effect of the change to a narrowing regime only when a second portion of precursors is introduced, indicates the necessity of a specific amount of monomer material, to facilitate passing into diffusion controlled growth.[5]

In conclusion, the addition of extra precursor material does not require gentle and continuous injections. However, the injected volume is important to exclude effects on the growth rate of the particles. Furthermore, by an exact adjustment of this parameter, diffusion controlled growth can be favored resulting in a narrowing of the size dispersion.

5. 2. Type I core/shell heterostructures

As shown in fig. 2.7, type I core/shell nanoheterostructures, which will be discussed here, possess an energetic band alignment whereby the band gap of the core material is located within that of the shell material. In comparison to the bare core material this coating results in an entire surface passivation by the shell material. Finally, due to this passivation, an improvement in the optical properties is achieved.

i. CdSe/CdS/ZnS

Utilizing materials of equal crystal structure, the coating possibilities are determined by the differences in the lattice constants. Hence, too high a mismatch (> 12-15%) would result in a limitation to the shell thickness even perhaps in non-epitaxial growth. Nevertheless, an opportunity to succeed in coating with a material on demand is by the introduction of a buffer layer. However, to keep type I alignment, the band gap of the buffer shell has to fit inbetween that of core and outer shell material. If zinc blende CdSe QDs were to be coated with ZnS, the interface would experience a lattice mismatch of nearly 11%, whereas CdSe/CdS and CdS/ZnS possess a mismatch of only 4 and 7%, respectively. Hence, CdS can be introduced as an intermediate shell layer.[6]

Contrary to the method of additional precursor injection, within heteroepitaxial coating, usually a method involving successive ion injection is undergone. Following a method with alternating injections, either cations or anions are introduced with subsequent intermittencies to allow for ion adsorption or reaction processes. This well established technique, originally developed for the deposition of thin films on solid substrates from solution baths, is called SILAR for *successive ion layer adsorption and reaction*. In early studies published in 1992/1993, this principle has been applied within syntheses of HgS-CdS[7] nanoheterostructures. However, a detailed description and deeper explanation has been published in 2003 by Li et al. and.[8]

Applying the SILAR protocol for CdSe QDs, as depicted in fig. 5.6, one can see that the absorption spectra are changing. According to the shell material, the high energy tail as well as the core absorbance, with its significant first absorbance maximum, is bathochromicly shifted, while the core absorbance is vanishing with increasing shell thickness. However, the emission properties are improved in terms of an increase in the height of the PL peak, indicating the success of the coating. A drawback of the coating is the red shift in the PL peak with proceeding of the coating (fig. 5.6 c). This has two reasons. One is represented by the possibility of tunneling of the CdSe electron wavefunction into the CdS shell material and as result the system is less

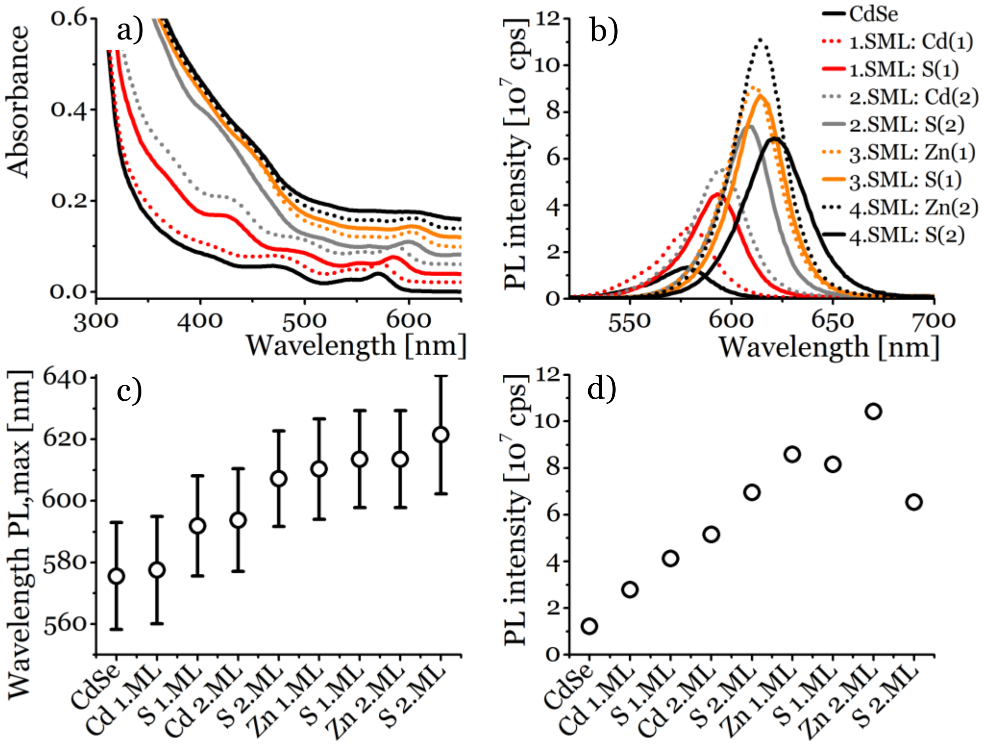

Figure 5. 6: Evaluating a type I coating to CdSe/CdS/ZnS QDs the wavelength of the first absorption transition as well as the PL are red shifted and the PL is intensified.
(a) Absorbance and (b) emission spectra represent CdSe cores as well as different shell phases within the deposition of CdS as well as ZnS as shell material. (c) Extracted values of PL maximum wavelength with corresponding fwhm (error bars) and (d) PL intensity.

confined, hence the PL behaves as if the core particle were larger i.e. the emission peak is red shifted. However, the main reason lies in the preparative method itself. Due to the high temperature required for the deposition of the shell material, diffusion processes are induced. Consequently two additional intermediate layers are formed consisting of $CdSe_{1-x}S_x$ and $Cd_{1-y}Zn_yS$, wherein x and y are determined by the reaction temperature as well as its duration. Additionally, within fig. 5.6 d significant data dispersion occurs as a ZnS shell is utilized. A decrease in the PL intensity is obtained by the addition of a sulfur layer, whereas the injection of the zinc precursor increases the PL intensity. The effect of intensity decrease is attributed to an incomplete passivation of the sulfur sites, whereby the number of dangling bonds increases and hence non-radiative recombination pathways are introduced.[9] However, the addition of $Zn(oleate)_2$ is envisaged as an additional stabilization of the sulfur sites due to the saturation of dangling bonds, whereas included free oleic acid molecules are proposed to stabilize zinc sites.[10]

ii. Gradated alloy structure: CdSe/ZnSe

A second combination of semiconductor materials to achieve type I heterostructures is represented by CdSe/ZnSe core/shell QDs with a gradated alloyed interface. Therefore, a simultaneous and slow injection of highly reactive shell precursors is performed, using diethylzinc, Et_2Zn, and hexamethyldisilthiane, $(Me_3Si)_2S$. The injection temperature was set to 190°C with subsequent growth at 180°C for 60 minutes to allow complete shell formation. Furthermore, an additional temperature increase to 300°C is undertaken to induce internal diffusion processes and hence to achieve a gradated alloyed interfacial region. This is done to examine the possibility to vary the photoluminescence wavelength due to shrinkage of the bare core material and consequently growth of the resulting intermediate alloyed layer. Finally QDs with a gradated quasi core/shell structure are obtained with CdSe rich core and ZnSe rich shell.[11]

The typical absorbance evolution is shown in fig. 5.7 a. During the initial stage of the reaction the first absorption transition is instantaneously red shifted (cf. fig. 5.7 a/1),

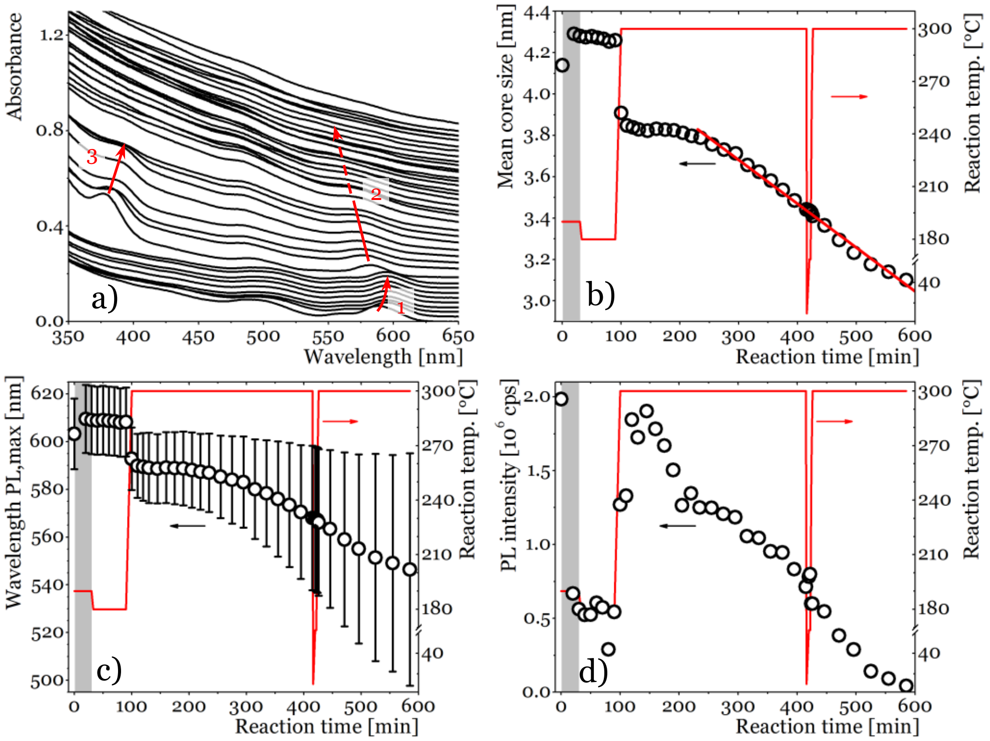

Figure 5. 7: Coating and annealing of initially bare CdSe QDs with a ZnSe shell, resulting in a blue shifted absorbance and emission maxima and decreased PL intensities due to ion diffusion processes and increased shell thicknesses.
(a) Absorption spectra (inset numbers are explained in the main text); (b) mean particle size as derived from (c) PL position; and corresponding PL intensity. For details of core particle size calculation see main text. Additionally, the temperature profile is presented as the red line. Grey area represents injection for coating.

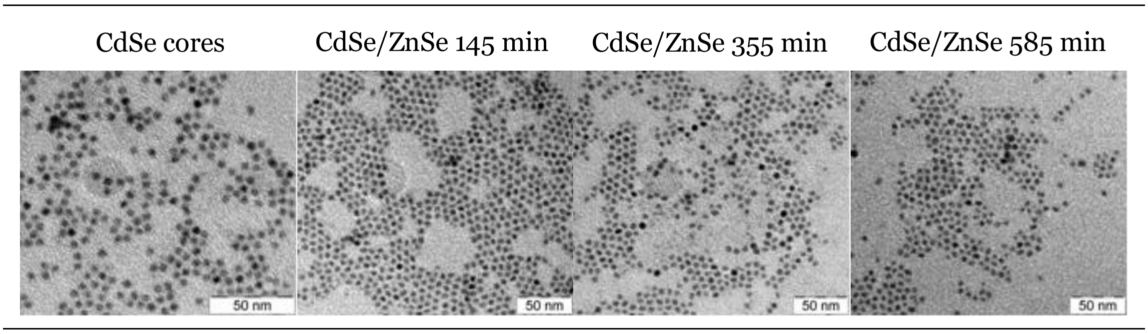

Figure 5. 8: TEM images of CdSe and CdSe/ZnSe QDs after given reaction times.

Table 5. 1: Sizes of CdSe and CdSe/ZnSe QDs after specific reaction times estimated from TEM images given in fig. 5.8.

Composition	CdSe	CdSe/ZnSe	CdSe/ZnSe	CdSe/ZnSe
Sampling time	—	145 min	355 min	585 min
TEM size	4.78±0.57 nm	5.63±0.77 nm	5.34±0.92 nm	5.34±0.54 nm

indicating a less confined system due to the presence of the shell and hence the particle PL makes it seem as if they are larger (cf. fig. 5.7 a-c). The instantaneous increase in the PL wavelength is associated with a fast shell growth attributed to the high reactivity of the shell precursors. By raising the temperature to 300°C a quick shift in the PL position towards higher energies is observed (cf. fig. 5.7 a/2). This indicates alloying processes at the interface between both materials, resulting in the formation of a ternary CdZnSe mixed crystal. This reveals as a blue shift of the first absorbance maximum as well as the PL maximum due to a decrease in the size of the bare core material. An annealing at 300°C induces further diffusion processes to achieve a gradated quasi core/shell structure with CdSe core, ZnSe shell and a $Cd_{1-x}Zn_xSe$ intermediate layer with increasing x in the direction from core to shell The evolution of the core size in fig. 5.7 a, derives from calculations following an equation of Čapek et al. and the approximation that the PL maximum correlates to the band gap energy.[12] As depicted in this plot, the core size systematically decreases after a certain equilibration time. This intermediate annealing time indicates ripening processes with a decreasing of the overall particle size, as stated by TEM images given in fig. 5.8 and tab. 5.1. Therein it is shown, that the core particles used here possess a diameter of 4.78 nm and the core/shell QDs at a reaction time of 145 min posses a diameter of 5.63 nm. As a result of a following shrinkage the diameter of the particles shrinks to an equilibrium size of 5.34 nm as obtained after 355 and 585 minutes reaction time. Within this reaction stage, no significant changes of the inner core size are observed. However, as may be seen in the absorption spectra in fig. 5.7 a, after reaching the equilibrium size a further

Table 5. 2: Ion diffusion within CdSe/ZnSe core/shell structures as a function of time: linear fit.

Linear fit – fitting parameters	**fitting results**
time range	230-600 min
coefficient of regression: R^2	0.9923
intercept: d (t = 0 min)	4.31664 nm
slope: d(d)/dt	$-0.00212\ \frac{nm}{min} \cong -1.272\ \frac{Å}{h}$

excitonic transition gets obvious. With proceeding annealing time this absorbance maximum at around 375 nm is red shifting to 400 nm (fig. 5.7 a/3), which indicates the formation and the growth of additional QDs, most probably ZnSe, due to ripening processes. This observation would explain the loss in material of the core/shell QDs as shown in tab. 5.1 (CdSe/ZnSe 145 to 355 min). However, shorter reaction times during the coating process leads to incomplete conversion of shell material. Subsequently during the annealing stage the particle size increases corresponding to the size expected for the amount of zinc precursor added (cf. ref. 11).

After a final equilibration, internal diffusion processes begin, indicated by a blue shift of the PL peak and hence a size decrease of the bare CdSe core. The change of the mean particle size (fig. 5.7 b) predicts a constant rate for the diffusion of Cd^{2+} and Zn^{2+}, although three different stages need to be considered Assuming an intermediate alloyed shell possessing an equilibrated Cd:Zn-ratio, one stage is the diffusion of Cd^{2+} and Zn^{2+} through this intermediate shell. Consequently the two remaining processes represent the substitution of Cd^{2+} by Zn^{2+} at the grain boundary close to core as well as a Zn^{2+} replacement by Cd^{2+} close to the shell. Consequently the alloyed region becomes larger as diffusion proceeds. Due to the constant behavior, a linear fit allows to determine the rate of the diffusion processes. Tab. 5.2 presents the results of this fit, where the speed of diffusion is represented by the slope. Thus a diffusion rate of 1.272 Å/h is obtained, which allows a precise control of the emission properties on demand for the presented system at an annealing temperature of 300°C.

5.3. Conclusion

In summary it is shown, that the inorganic coating represents an opportunity to improve the optical properties of QDs. One has to differentiate between the *in situ* or one pot as well as the two pot coating procedure. The *in situ* procedure is preferred for homoepitaxial growth and hence is employed to overcome the limit in particle size by introducing an additional monomer supply. It is shown, that the diffusion controlled growth regime (following classical theories) is suitable for the addition of extra precursor material due to its characteristic narrowing of the size dispersion. Following a slow injection of diluted precursor solutions, a fine tuning of the final particle size is possible, as an intermittency in the whole reaction nevertheless keeps the deposition rate unaffected. However, a gentle and continuous injection is not mandatory, if the amount of injected volume is exactly adjusted. Therefore, several single injections at certain times allow the diffusion controlled regime to be favored. On the other hand too big a volume involves large concentrations and may result in additional homogeneous nucleation as well as a favoring of the reaction controlled growth regime. A homoepitaxial coating procedure may involve PL quenching due to the introduction of internal defects. This can be avoided by a gentle deposition rate, which is adjusted by the reaction temperature, as well as a final annealing stage, which induces internal "self-healing" diffusion processes.

However heteroepitaxial growth of a different material onto the bare core usually results in an improvement in the optical properties allowing several kinds of core/shell structures to be possible. Besides this, gradated quasi core/shell structures are conceivable, where diffusion processes, which are induced by temperature increases, enable shrinkage of the bare core material, which results in a blue shift of the PL peak. Applying this method, a precise control of the emission properties on demand is possible due to defined diffusion rates which depend on the reaction temperature.

5.4. References

[1] a) E. Khon, N. N. Hewa-Kasakarage, et al., *Chemistry of Materials* **2010**, *22*, 5929; b) K. P. Acharya, N. N. Hewa-Kasakarage, et al., *The Journal of Physical Chemistry C* **2010**, *114*, 12496.

[2] I. V. Markov, *Crystal Growth for Beginners*, 2nd ed., World Scientific, Singapore, **2003**.

[3] P. Reiss, (Ed.: A. L. Rogach), *Semiconductor Nanocrystal Quantum Dots*, Springer Vienna, **2008**, pp. 35.

[4] C. B. Murray, D. J. Norris, et al., *Journal of the American Chemical Society* **1993**, *115*, 8706.

[5] X. Peng, J. Wickham, et al., *Journal of the American Chemical Society* **1998**, *120*, 5343.

[6] R. Xie, U. Kolb, et al., *Journal of the American Chemical Society* **2005**, *127*, 7480.

[7] a) A. Eychmüller, A. Hässelbarth, et al., *Journal of Luminescence* **1992**, *53*, 113; b) A. Hässelbarth, A. Eychmüller, et al., *The Journal of Physical Chemistry* **1993**, *97*, 5333.

[8] J. J. Li, Y. A. Wang, et al., *Journal of the American Chemical Society* **2003**, *125*, 12567.

[9] L. Spanhel, M. Haase, et al., *Journal of the American Chemical Society* **1987**, *109*, 5649.

[10] a) S. Datta, M. Kabir, et al., *The Journal of Physical Chemistry C* **2008**, *112*, 8206; b) U. Soni, S. Sapra, *The Journal of Physical Chemistry C* **2010**, *114*, 22514.

[11] S. K. Panda, S. G. Hickey, et al., *Journal of Materials Chemistry* **2011**, *21*, 11550.

[12] R. K. Čapek, I. Moreels, et al., *The Journal of Physical Chemistry C* **2010**, *114*, 6371.

6

Summary and conclusion

The objectives of this thesis were to improve the hot injection synthesis of CdSe and CdTe nanoparticles and their further processing. Therefore, conditions for reproducible syntheses with respect to narrow size distributions and improved optical properties were established. The resulting improvements were analyzed regarding their thermodynamic and/ or kinetic influence on the particular system. Additionally, the further processing of the resulting core materials is investigated by means of an inorganic coating.

In the following sections the main results obtained in this work will be summarized and the key points highlighted.

Quasi-seeded growth approach: CdSe QDs

The applicability of highly reactive tin$^{(II)}$ or lithium$^{(I)}$ species as *quasi*-seed precursors has been investigated for the improvement of CdSe syntheses (chapter 3).

It has been shown, that by introducing *bis*-(*bis*-trimethylsilyl)amino tin$^{(II)}$ or (*bis*-trimethylsilyl)amino lithium$^{(I)}$ into the reaction it is possible to decrease the ensemble size dispersion as well as to increase quantum yield and particle yield. These highly reactive species have been identified to act as *quasi*-seed precursor following a proposed mechanism of cation-exchange mediated nucleation. By means of a cation exchange mediated nucleation, *quasi*-seeds of either SnSe or Li_2Se are formed, which subsequently undergo a cation exchange with Cd^{2+} resulting in highly monodisperse CdSe QDs. Due to increased reactivity the nucleation is accelerated and the number of nuclei is increased, which leads to improved reaction yields regarding the particle concentrations. The optimal amount of the *quasi*-seed precursor has been determined as to 5-10 % Sn (SnSe; or 10-20 % Li, Li_2Se) to the deployed cadmium concentration.

Within detailed characterization, the reactive *quasi*-seed precursor of tin$^{(II)}$ has been identified to exhibit a complex coordinating structure including carboxylate as well as silylamide ligands. The necessity of the sensitive $[(Me_3Si)_2N]_2Sn$ has been examined, as the replacement for compounds of less prices and easier handling failed due to their too low reactivity. Nevertheless, utilizing a similar species, namely [(Me3Si)2N]Li, the advantages of the investigated mechanism have been recovered.

Finally, the investigated mechanism has been successfully implemented to a 10-fold laboratory batch up-scaling. Due to the simple application of the *quasi*-seed precursor, complicated optimization steps are avoided.

Precursor activation by altered injections: CdTe QDs

The synthesis of CdTe nanoparticles has been kinetically investigated by altered injection pathways. Detailed examinations have led to the results of a precursor activation following the cation injection pathway. Therein, the cation, stabilized by weak binding ligands, is injected to the anion species, which is aged in the presence of suitable ligands that strongly bind to the cation.

Explicitly, optimized conditions in the present case of CdTe QDs have been found to comprise of the injection of cadmium oleate to a solution of tellurium in *n*-trioctylphosphine (TOP) in the presence of *n*-tetradecylphosphonic acid (TDPA). Therein, cadmium oleate is the more reactive cation species in comparison to the corresponding phosphonate. However, the phosphonic acid is responsible for tellurium activation by oxidation of free TOP molecules under formation of molecules, which do not stabilize tellurium.

Support of the obtained results is given by a study of varied Cd-to-Te-ratios. Thus, utilizing deficiencies of cadmium, the concentration of free phosphonic acid is increased, which significantly affects the growth stage by means of Ostwald ripening. On the other hand using deficiencies of tellurium the anion activation becomes enhanced due to an increased TDPA-to-TOP-ratio.

Furthermore, it is shown that the reaction temperature has significant influence on the nucleation event. Thus, at injection temperatures of 270°C the critical size has been attributed to the obtained magic-sized clusters with an absorbance maximum at 445 nm and a diameter of approximately 1.8 nm. Although, the mechanism of the overall particle growth has not been entirely resolved, it has been suggested to be initiated either by coalescence of MSCs among each other, by deposition of monomer material onto the MSCs surface or a combination of both. The subsequent QD growth with proceeding monomer consumption is attended with a slow disappearance of the MSC features. Within the studies of varied Cd-to-Te-ratios a second cluster at 365 nm is obtained utilizing an excess of cadmium. This species itself disappears in the course of the reaction. Hence the disappearance of the MSCs is attributed to a kind of a reverse discontinuous mode under formation of monomer material and is explained by configurational deviations from the ideal closed-shell structure of the MSCs.

Inorganic coating: core/shell QDs

With regard to the opportunity for an improvement of the optical properties of QDs strategies of inorganic coatings have been investigated. Therein it has been differentiated between *in situ* or one pot as well as two pot coatings. The *in situ* procedures are preferred for homoepitaxial growth and hence are devoted to overcome the limit particle size by additional monomer supply. It has been shown, that the diffusion controlled growth regime (following classical theories) is suitable for the addition of extra precursor material due to its characteristic narrowing of the size dispersion. Following slow injections of diluted precursor solutions, a fine tuning of the final particle size is possible, as an intermittency of the whole reaction keeps the deposition rate unaffected. However, gentle and continuous injections are not mandatory, if the amount of injected volume is exactly adjusted. Therefore, several single injections at certain times allow the diffusion controlled regime to be favored. On the other hand, a too large volume involves huge concentrations and may result in additional homogeneous nucleation as well as favoring of the reaction controlled growth regime. It has been shown, that homoepitaxial coating procedures attend PL quenching due to the introduction of internal defects. This can be avoided by gentle deposition rates, which are adjusted by the reaction temperature, as well as a final annealing stage, inducing internal “self-healing” diffusion processes.

However heteroepitaxial growth of a different material onto the bare core usually results in an improvement of the optical properties. Therefore, type I nanoheterostructures are considered, which are defined by a confinement of the charge carriers within one material (e.g. CdSe/CdS/ZnSe). Beside this, gradated quasi core/shell structures (CdSe/ZnSe) have been investigated. Due to temperature increases diffusion processes have been induced, which enable shrinkage of the bare core material resulting in a blue shift of the PL peak. Applying this method, a precise control of the emission properties on demand is possible due to defined diffusion rates depending on reaction temperature.

Appendix

A

Experimental

A.1. Reagents

The following listed reagents are used as received with the exception of *n*-trioctylphosphine, which was distilled under vacuum and stored inside a glove box. All solvents were obtained from commercial sources and used as received.

Supplier	Acronym	Purity
Acros		
oleylamine	OlAm	80-90%
Aldrich		
1-octadecene	ODE	90%
bis[bis(trimethylsilyl)amino] tin(II)	$[(Me_3Si)_2N]_2Sn$	no information
cadmium(II) acetate	$CdAc_2$	≥ 99%
cadmium(II) oxide	CdO	99.5%
diethyl zinc(II)	$ZnEt_2$	Zn 52 wt% (min.)
lithium(I) bis(trimethylsilyl)amide	$[Me_3SiN]Li$	97%
n- trioctylphosphine oxide	TOPO	99%
octadecylamine	ODA	> 90%
oleic acid	OlAc	90%
sulfur, powder	S	99.98%
tin(II) chloride dihydrate	$SnCl_2$	98%
zinc(II) acetate	$ZnAc_2$	99.99%
zinc(II) oxide	ZnO	99.99%
ChemPur		
selenium, powder 325 mesh	Se	99.99+%
tellurium, powder	Te	99.999%
Fluka		
hexadecylamine	HDA	≥ 99%
n-trioctylphosphine	TOP	90%
Plasma Chem		
n-tetradecylphosphonic acid	TDPA	97%
Riedel de-Häen		
sodium oleate	Na(oleate)	no information

A.2. Precursor solutions

i. Cadmium(II) oleate in 1-octadecene

Cd-Stock

In a 50 ml flask 4 mmol (513.6 mg) CdO are cracked in 40 ml ODE and 20 mmol (6.35 ml) OlAc (final concentration of Cd^{2+}: 0.086 molar). Therefore the reagents are heated to 100°C under vacuum for 60 minutes. Subsequently this solution was blanketed with an argon atmosphere and the temperature further raised to 300°C until the brown turbid solution turned colorless and clear. The resulting solution is allowed to cool to ambient temperature.

Storage under inert atmosphere is not required, but the solution should be exhausted within 3 weeks.

ii. Selenium in *n*-trioctylphosphine

TOP-Se

A 1 molar solution is prepared by dissolution of 20 mmol (1.579 g) selenium powder in 20 ml TOP at 120-150°C applying vigorous stirring under inert atmosphere in a nitrogen filled glove box.

Storage under inert atmosphere is required to prevent the oxidation of TOP and should be exhausted within 3 months.

iii. Tellurium in *n*-trioctylphosphine

TOP-Te

A 1 molar solution is prepared by dissolution of 20 mmol (2.552 g) tellurium powder in 20 ml TOP at 120-150°C applying vigorous stirring under inert atmosphere in a nitrogen filled glove box.

Storage under inert atmosphere is required to prevent the oxidation of TOP. The solution is in good condition if it stays clear, but should be replaced if a white precipitate occurs.

iv. Bis[(bis(trimethylsilyl)amino]tin(II) in 1-octadecene

$[(Me_3Si)_2N]_2Sn$

A 0.02 molar solution is prepared diluting 0.2 mmol (77 µl) $[(Me_3Si)_2N]_2Sn$ to 1 ml ODE under inert atmosphere in a nitrogen filled glove box.

The solution has to be prepared freshly and exhausted within one day. It requires to be stored under inert atmosphere to prevent the decomposition of $[(Me_3Si)_2N]_2Sn$.

v. Lithium(I) bis(trimethylsilyl)amide in 1-octadecene

$[Me_3SiN]Li$

A 0.01 molar solution is prepared dissolving 0.06 mmol (10 mg) $[Me_3SiN]Li$ in 6 ml ODE under inert atmosphere in a nitrogen filled glove box.

The solution should be exhausted within one month and should be stored under inert atmosphere.

vi. Tin(II) oleate from bis[(bis(trimethylsilyl)amino]tin(II) in 1-octadecene

$Sn(oleate)_2/0.1$

A 0.1 molar solution is prepared diluting 0.4 mmol (154.6 µl) $[(Me_3Si)_2N]_2Sn$ and 1.0 mmol (317.4 µl) OlAc to 4 ml with ODE *in vacuo*.

Storage under inert atmosphere is not required, but the solution should be exhausted within one week.

vii. Tin(II) oleate from tin(II) chloride

$Sn(oleate)_2$

Following a procedure of Park et al.[1] tin(II) oleate is prepared using 2 mmol (379.2 mg) $SnCl_2$ and 4 mmol (1.22 g) Na(oleate) in a 2-phase mixture of 10 ml hexane, 7 ml ethanol and 6 ml de-ionized water. The mixture is refluxed under argon at 70°C for at least 4 hours. The hexane phase is separated from the aqueous phase using a separating funnel and washed 5 times with de-ionized water. Pure tin(II) oleate is obtained removing hexane under vacuum at 30°C.

Storage under inert atmosphere is not required and the oleate is stable for weeks. An obtained infusible solid indicates the crystallized tin(II) oleate and can be dissolved in ODE.

viii. Coating solutions

$Cd(oleate)_2$, $Zn(oleate)_2/0.04$

A 0.04 molar solution of either $Cd(oleate)_2$ or $Zn(oleate)_2$ is prepared by dispersing and cracking 0.8 mmol CdO (102.75 mg) or ZnO (65.11 mg) in 2.5 ml OlAc and 17.5 ml ODE, evacuating at 100°C for 60 minutes and heating to 320°C under argon atmosphere until a colorless and clear solution is obtained.

ODE-S

A 0.04 molar solution of sulfur in ODE is prepared inside a glove box dissolving 0.8 mmol (25.65 mg) S in 20 ml ODE at 100°C under vigorous stirring.

$ZnEt_2$

A 1 molar solution in TOP is prepared inside a nitrogen filled glove box by diluting 1 mmol (103 µl) $ZnEt_2$ to 1 ml with TOP.

The solution should be exhausted within 2 days.

The solutions need to be kept under inert atmosphere (glove box) and are stable for months, unless noted otherwise.

A.3. Synthesis of QDs

The synthesis is undertaken following optimized procedures of Talapin et al.[2] and Peng and co-workers[3] as published.[4] All reactions are performed under inert argon atmosphere on a Schlenk line using a three-necked flask fitted with rubber septum and condenser and connected to a temperature controller.

i. Synthesis of CdSe QDs

a) Hot injection synthesis

A 25 ml flask is loaded with 8 ml ODE, 4 ml $Cd(oleate)_2$ as Cd-Stock, 5.2 mmol (2 g) TOPO and 8.3 mmol (2 g) HDA, degassed at 100°C for 60 minutes. Subsequently, the mixture is heated under argon to the desired injection temperature (T_{inj}; 230, 250, 270 or 300°C) with a fast heating rate of approximately 30°C/minute. Into this hot solution a mixture of 2 ml 1-octadecene, 1.6 ml TOP and 0.4 ml (1 M) TOP-Se is quickly injected. The nanoparticles are allowed to grow for an appropriate duration at a growth temperature of $T_{gr} = T_{inj} - 25$ K. To stop the reaction after the desired particle size is reached, 6 ml of toluene are injected with simultaneous cooling the reaction flask by cold water.

b) *Quasi*-seeded growth synthesis

The synthesis recipe follows that of the *Hot Injection Synthesis* with the following changes and additions:

The amount of ODE used in the evacuation step is diminished by the amount of solvent necessary to dissolve the precursor species. Immediately after the evacuation step at 100°C, the flask is blanketed with an argon atmosphere and the desired amount of the *quasi*-seed precursor is introduced via the rubber septum. As *quasi*-seed precursor different species are investigated which are given in tab. 3.1.

Table A. 1: Investigated *quasi* seed precursor species.

***quasi*-seed precursor**		**investigated amounts**
bis[bis(trimethylsilyl)amino] tin(II)	$[(Me_3Si)_2N]_2Sn$	4, 8, 20, 40, 80 µmol
SnOleate from $SnCl_2$ in ODE	SnOleate^2	20 µmol
lithium(I) bis(trimethylsilyl)amide in ODE	$[Me_3SiN]Li$	20 µmol

c) Laboratory batch up-scaling

The up-scaling of the CdSe syntheses is undergone in two increasing steps, first using a 50 ml flask and 4 mmol [Cd-Se] and second a 100 ml flask and 10 mmol [Cd-Se]. The stoichiometric amounts of precursors, stabilizers and solvents are given in Tab. 3.2. The experimental procedure is following the standard *Hot Injection* or *Quasi Seeded Growth Syntheses* protocol with the exception that CdO is cracked by oleic acid in ODE before the addition of TOPO, HDA and $[(Me_3Si)_2N]_2Sn$.

Table A. 2: Synthesis details (stoichiometric amounts) for the up-scaling process.

batch scale	**flask**	**injection solution (syringe)**
50 ml	4 mmol (513.6 mg) CdO 20 mmol (6.34 ml) OlAc 0.2 mmol (77.5 µl) $[(Me_3Si)_2N]_2Sn$	4 mmol Se (4 ml, 1M TOP-Se)
	14 ml ODE	
	10.4 mmol (4 g) TOPO 16.6 mmol (4 g) HDA	
100 ml	10 mmol (1284 mg) CdO 50.4 mmol (16 ml) OlAc 0.5 mmol (193.5 µl) $[(Me_3Si)_2N]_2Sn$	10 mmol Se (5 ml, 2 M TOP-Se)
	29 ml ODE	
	20.8 mmol (8 g) TOPO 33.2 mmol (8 g) HDA	

ii. Synthesis of CdTe QDs

a) Anion injection

A 25 ml flask is loaded with 6 ml ODE, 4.7 mmol (1.8 g) TOPO, 8.3 mmol (2.0 g) HDA, 0.7 mmol (200 mg) TDPA and Cd(oleate)$_2$ (4 ml Cd-stock solution). This mixture is heated to 120°C under vacuum with vigorous stirring and maintained at this temperature for 60 minutes. Subsequently this solution is blanketed with an argon atmosphere and the temperature further raised to 300°C. Meanwhile the injection solution of 2 ml ODE, 1.6 ml TOP and 0.4 ml (1 M) TOP-Te is prepared under inert atmosphere and transferred to a 10 ml-glass syringe. This solution is then quickly injected into the Cd-containing flask at the desired injection temperature of 270°C or 300°C and the growth temperature is set to be 25 K below the injection temperature. To stop the reaction once the desired particle size is reached, 6 ml of toluene are injected into the reaction mixture with simultaneous cooling the reaction flask by cold water.

b) Cation injection

A 25 ml flask is loaded with 8 ml ODE, 4.7 mmol (1.8 g) TOPO, 8.3 mmol (2.0 g) HDA, 0.7 mmol (200 mg) TDPA, 1.6 ml TOP and 0.4 ml (1 M) TOP-Te. This mixture is heated to 120°C under vacuum with vigorous stirring and the temperature maintained for 60 minutes. Subsequently this solution is blanketed with an argon atmosphere and the temperature further raised to 300°C. Meanwhile the injection solution of Cd(oleate)$_2$ (4 ml Cd-stock) is transferred to a 10 ml-glass syringe. This solution is then quickly injected into the Se-containing flask at the desired temperature of 270°C or 300°C and for the growth the temperature was set to be 25 K below the injection temperature. The reaction is stopped similar to protocol of the anion injection.

A.4. Inorganic coating of QDs

i. Seeded growth: extra precursor addition

CdSe/CdSe, CdTe/CdTe

To obtain particles with larger sizes, extra precursor solution (Cd-Stock, as well as TOP-Te or TOP-Se) is added dropwise to the standard core synthesis. For small amounts the classic injection by hand is possible, but for larger volumes a syringe pump is recommended. Starting time of the precursor addition is approximately between 20 and 30 minutes after the injection that induces the nucleation burst.

ii. Type I core/shell heterostructures

CdSe/CdS/ZnS core/shell/shell QDs

Adapting the successive ion layer adsorption and reaction technique (SILAR), developed for QDs by Li *et al.*[3b], in 25 ml flask $5 \cdot 10^{-8}$ mol of the purified CdSe QDs in hexane are dispersed in a mixture of 6 ml ODE and 5.6 mmol (1.5 g) octadecylamine. This mixture is heated to 60°C under vacuum to remove the hexane and further heated to 100°C for 60 minutes to remove any residue of oxygen and moisture. This solution is then blanketed with an argon atmosphere and heated to 240°C for the slow injection of $Cd(oleate)_2$ in ODE (0.04 M). After 10 minutes growth the anion precursor S in ODE (0.04 M) is slowly injected and allowed to grow for 20 minutes. This alternating successive precursor injection is also used for the zinc sulfide layers at a reaction temperature of 220°C and is repeated until the desired shell thickness is obtained. Optionally, this procedure can be applied for the binary core/shell system CdSe/ZnS.[4]

Gradated CdSe/ZnSe core/shell QDs

A seeded growth approach towards the coating of CdSe QDs with a ZnSe shell is undertaken using a procedure following Panda et al.[5] A third of the obtained CdSe QDs are dispersed in a mixture of 5.2 mmol (2 g) TOPO and 6.2 mmol (1.5 g) HDA. After evacuation at 100°C for 60 minutes, 1.5 ml TOP are added and this solution is heated to 190°C under argon atmosphere. Meanwhile, an injection mixture of 300 µl (1 M) $ZnEt_2$ in TOP, 300 µl (1 M) TOP-Se, and 2 ml TOP is prepared inside of a glove box. This solution is then added dropwise to the CdSe core solution at a rate of 5 ml/hour. After the complete addition, the temperature was lowered to 180°C and the mixture annealed for another 60 minutes to form the ZnSe shell over the CdSe QDs. Finally the solution is cooled to room temperature. To synthesize the ternary alloyed QDs containing a gradated alloy composition the obtained solution is again annealed at 300°C for 3 hours without previous cleaning.

A.5. Purification of core and core/shell QDs

To purify the QDs from the crude solution, the quenched solution is transferred into a centrifuge glass, the QDs are dissolved with an excess of toluene, until a clear non-turbid solution is obtained. After addition of 2-propanol/methanol the particles are separated by centrifugation at 4800 rpm (RCF: 4170 × g) for 5-10 minutes and the supernatant decanted. The particles obtained are further purified by repeated precipitation from toluene with an excess of methanol.

As the particle growth is monitored spectroscopically, during the syntheses 100 µl-aliquots were taken at different times and dissolved in toluene. No further cleaning or centrifugation steps were undertaken to ensure a complete surface coverage of the ligands.

A.6. Characterization methods and apparatus

i. Optical characterization

a) UV/Vis absorption spectroscopy

Absorption spectra were recorded using a CARY 50 spectrophotometer (Varian Inc., Palo Alto CA). All spectra were measured at room temperature with an average integration time of 0.2 s/nm and spanning a spectral region of 300-900 nm. Sample aliquots are dissolved in toluene within a 4 ml-quartz cuvette with 1 cm path length of the light with pure toluene as reference/ background.

b) Fluorescence spectroscopy

Fluorescence measurements were performed using a FluoroMax-4 spectrofluorometer (HORIBA Jobin Yvon Inc., Edison, NJ) with an excitation wavelength of 400 nm. All spectra were recorded at room temperature with an average integration time of 0.1 s/nm and spanning a spectral region of 420-750 nm. The gap widths of excitation and emission monochromator are set to be 2 nm. The spectra are corrected according to monochromater characteristics as well as lamp intensity.

ii. Crystallographic characterization

a) Transmission electron microscopy (TEM)

TEM imaging was carried out on a Philips EM208S microscope with an acceleration voltage of 100 kV. Samples for TEM were prepared by dropping diluted QD solutions in toluene onto copper grids coated with a Formvar-carbon film and subsequent evaporation of the solvent.

b) X-ray powder diffraction (XRD)

X-ray powder diffraction was performed with a STOE STADI-P (IP) diffractometer with Cu-K_α radiation in transmission mode. Samples for XRD were prepared via repeated washing of precipitated QDs with an excess of acetone to ensure a complete ligand removal and subsequent vacuum drying to achieve dry powders.

iii. Elemental analysis

a) Fourier transform infrared spectroscopy (FTIR)

FTIR measurements were performed using a Nicolet 8700 FTIR spectrometer (ThermoScientific) equipped with diamond ATR crystal. The data were collected via 32 scans with a resolution of 4 (data spacing of 0.482 cm^{-1}).

b) Optical emission spectroscopy (ICP-OES)

Cation detection was perfomed using an Optima 7000DV optical emission spectrometer (Perkin-Elmer) equipped with inductively coupled plasma vaporizer. The spectrometer spans a spectral range from 160-900 nm and is equipped with high resolution Echelle optics with 30°-CaF_2 prism and SCD detector.

For sample preparation the required 10 ml-volumetric flasks are thoroughly cleaned with a solution containing 5 mol/l KOH as well as pure mQ water. Within this flask a 10 µl-aliquot is dried by heat and subsequent digested using 100 µl of a solution containing nitric and hydrochloric acid (1:3). To ensure entire dissolution of the QDs, this solution is heated to 150°C in the closed flask. Finally the flask is filled with mQ water. A blank sample is prepared following the same procedure without using QDs.

A.7. References

[1] J. Park, K. An, et al., *Nature Materials* **2004**, *3*, 891.

[2] D. V. Talapin, A. L. Rogach, et al., *Nano Letters* **2001**, *1*, 207.

[3] a) L. Qu, X. Peng, *Journal of the American Chemical Society* **2002**, *124*, 2049; b) J. J. Li, Y. A. Wang, et al., *Journal of the American Chemical Society* **2003**, *125*, 12567.

[4] M. Chursanova, V. Dzhagan, et al., *Nanoscale Research Letters* **2010**, *5*, 403.

[5] S. K. Panda, S. G. Hickey, et al., *Journal of Materials Chemistry* **2011**, *21*, 11550.

B

Validation of Yu's sizing equations

B.1. Yu's sizing equations

In 2003, W. William Yu and co-workers published an article with the title "Experimental Determination of the Extinction Coefficient of CdTe, CdSe and CdS nanocrystals".[1] Within this work Yu examined the extinction coefficient of cadmium chalcogenide nanocrystals obtained via the hot injection method using absorption measurements. Following Lambert-Beer's law, an important variable to calculate the extinction coefficient is the concentration of the analyte. The concentration of nanoparticles can be determined from their sizes and its corresponding concentrations of cadmium ions. This requires huge efforts on TEM measurements and a careful elemental analytic. Finally Yu's work resulted in empirical fitting functions for extinction coefficient as well as particle size calculated from the first absorbance maximum for the $1S_e$-$1S_h$ transition using UV/Vis absorption spectroscopy.

As absorption spectra somehow represent the quantum confinement of electrons within nanocrystals, many parameters have influence including the shape of the particles. Thus, the sizing equation (eq. B.1) obtained by Yu et al. for CdTe nanoparticles is subject of the following validation.

$$d = (9.8127 \cdot 10^{-7}) \cdot \lambda^3 - (1.7147 \cdot 10^{-3}) \cdot \lambda^2 + 1.0064 \cdot \lambda - 194.84 \qquad \text{(B. 1)}$$

As mentioned above, this equation is based on results supported by a TEM study and therefore may be accepted as being valid for CdTe nanoparticles whose $1S_e$-$1S_h$ absorbance maxima are in the wavelength range from 570 to 745 nm as suggested by the authors.

Similar to CdTe an equation for CdSe nanoparticles is given by Yu et al. (eq. B.2). This equation is also applied within this work and is suggested to be valid in a wavelength range from 320 to 660 nm, consequently it is equally controlled by TEM measurements.

$$\begin{aligned} d = {} & (1.6122 \cdot 10^{-9}) \cdot \lambda^4 - (2.6575 \cdot 10^{-6}) \cdot \lambda^3 \\ & + (1.6242 \cdot 10^{-3}) \cdot \lambda^2 - 0.4277 \cdot \lambda + 41.57 \qquad \text{(B. 2)} \end{aligned}$$

B.2. Validation using TEM measurements

i. CdTe QDs

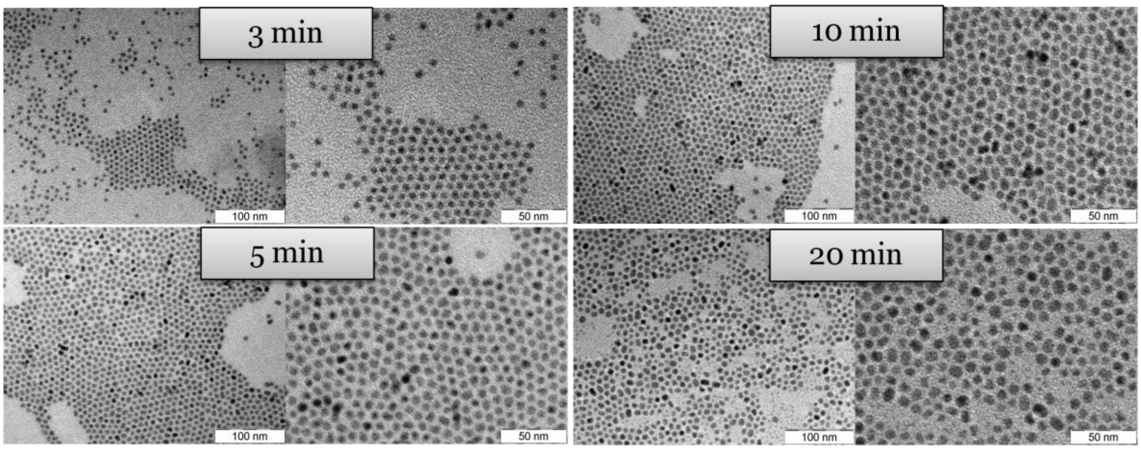

Figure B. 1: TEM images of a selection of CdTe particles synthesized at 300°C following the cation injection pathway.

For the kinetic study in chapter 4 a comparison of experimentally obtained and theoretically calculated sizes is undertaken. Therefore sizes obtained by TEM investigation undertaken in-house of at least 100 particles per synthesis (cf. fig. B.1 and B.2) are compared with the sizes calculated by the above mentioned equation for a selection of particles (cf. tab. B.1). This investigation leads to the result that the equation is valid for the syntheses protocol and hence the growth study of CdTe QDs underwent here.

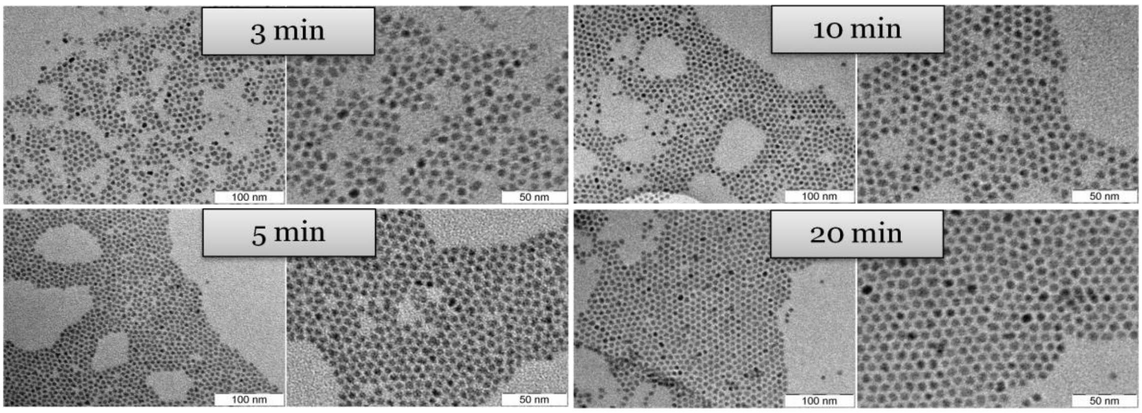

Figure B. 2: TEM images of a selection of CdTe particles synthesized at 300°C following the anion injection pathway.

Table B. 1: Comparison of particle sizes derived from calculations using data from the absorption spectra and TEM investigations.

Growth time	**Cation injection - CdTe**		
	1st absorbance maximum	**Lit. eq.**	**TEM**
3 min	652.98 nm	4.39 nm	4.69±0.37 nm
5 min	676.31 nm	5.05 nm	4.90±0.41 nm
10 min	688.29 nm	5.49 nm	5.81±0.39 nm
20 min	702.68 nm	6.15 nm	6.11±0.48 nm
	Anion injection - TeCd		
3 min	623.75 nm	3.91 nm	4.12±0.60 nm
5 min	651.33 nm	4.37 nm	4.49±0.66 nm
10 min	680.33 nm	5.18 nm	5.26±0.56 nm
20 min	705.28 nm	6.28 nm	6.37±0.68 nm

“Lit. eq.” refers to the sizes as derived from Yu’s equation taken a literature source.[1]

ii. CdSe QDs

While a precise validation study was undertaken for CdTe and resulted in a good agreement between theoretical and experimental data, equation B.2 for CdSe is tested for random samples derived following the hot injection method as well as the *quasi*-seeded growth approach. Comparing the values in tab. B.2, within an experimental error, the sizing equation for CdSe by Yu et al. is validated and can be applied for the present investigations.

Table B. 2: Comparison of particle sizes derived from calculations using data from the absorption spectra and TEM investigations.

Sample	**Standard hot injection - CdSe**		
	1st absorbance maximum	**Lit. eq.**	**TEM**
#1	560.72 nm	3.28 nm	3.42±0.48 nm
#2	584.46 nm	3.97 nm	4.08±0.57 nm
#3	626.31 nm	5.99 nm	6.16±0.53 nm
	***Quasi*-seeded growth approach - $CdSe_{Sn}$**		
#1	558.31 nm	3.22 nm	3.58±0.49 nm
#2	585.79 nm	4.02 nm	4.177±0.48 nm
#3	595.20 nm	4.38 nm	4.78±0.57 nm

“Lit. eq.” refers to the sizes as derived from Yu’s equation taken a literature source.[1]

B.3. References

[1] W. W. Yu, L. Qu, et al., *Chemistry of Materials* **2003**, *15*, 2854.

C

Constants

C.1. Natural constants

Avogadro's number	$N_A = 6.02214 \cdot 10^{23}\ \text{mol}^{-1}$
universal gas constant	$R = 8.31451\ \frac{\text{J}}{\text{K}\cdot\text{mol}}$
dielectric constant of vacuum	$\varepsilon_0 = 8.85419 \cdot 10^{-12}\ \frac{\text{A}\cdot\text{s}}{\text{V}\cdot\text{m}}$
electron mass	$m_0 = 9.10939 \cdot 10^{-31}\ \text{kg}$
Boltzman's constant	$k_B = 1.38066 \cdot 10^{-23}\ \frac{\text{J}}{\text{K}}$

C.2. Element and compound specific constants

i. Ionic radii in crystals

Cd^{2+}	0.78 Å (CN = 4)	[1]
Li^{+}	0.59 Å (CN = 4)	[1]
Sn^{2+}	1.12 Å	[2]

ii. Ionization potential

Cd	8.99382 eV	[1]
Li	5.391719 eV	[1]
Sn	7.34392 eV	[1]

iii. Band gap energy

CdS	zb, $E_g = 2.4$ eV	[3]
CdSe	zb, $E_g = 1.66/1.74$ eV	[3]
CdTe	zb, $E_g = 1.49$ eV	[3]
ZnS	zb, $E_g = 3.7$ eV	[3]
ZnSe	zb, $E_g = 2.8$ eV	[3]
$Cd_{1-x}Zn_xSe$	zb, $E_g(x) = x\, E_{0,ZnSe} + (1-x)\, E_{0,CdSe} - b\, x\, (1-x)$	[3]
SnSe	$E_{g,ind} = 0.9$ eV	[4]
SnTe	zb, $E_g = 2.07$ eV	[4]

iv. Effective masses at 300 K

zinc blende modifications [3]

CdSe	$m_e = 0.12\ m_0$	$m_h = 0.16/0.18\ m_0$
CdTe	$m_e = 0.11\ m_0$	$m_h = 0.63\ m_0$

v. Dielectric constant

CdSe	$\varepsilon_\infty = 5.8$	[3]
CdTe	$\varepsilon_\infty = 7.1$	[3]

vi. Lattice constant

CdS	zb, a = 5.818 Å	[5]
CdSe	zb, a = 6.05 Å	[5]
CdTe	zb, a = 6.482 Å	[5]
Li_2Se	fcc, a = 6.0014 Å	[6]
Li_2Te	fcc, a = 6.504 Å	[7]
ZnS	zb, a = 5.4093 Å	[5]
ZnSe	zb, a = 5.6676 Å	[5]
SnSe	a = 11.57 Å, b = 4.19 Å, c = 4.46 Å	[4]
SnTe	fcc, a = 6.313 Å	[5]

vii. Unit cell volume

CdSe	zb, $2.217 \cdot 10^{-22}$ cm^3	[8]
CdTe	zb, $2.723 \cdot 10^{-22}$ cm^3	[8]

C.3. References

[1] D. R. Lide, p. 9-49/10-203/12-11/12-91, 89. ed., 2008/2009 ed., CRC Press, Boca Raton, Fla. [u.a.], **2008**.

[2] L. Pauling, *Die Natur der chemischen Bindung*, p. 475/479, 3. ed., Verlag Chemie, Weinheim/B., **1968**.

[3] O. Madelung, U. Rössler, et al., *Landolt-Börnstein - Group III Condensed Matter, Numerical Data and Functional Relationships in Science and Technology, Vol. 41B: II-VI and I-VII Compounds; Semimagnetic Compounds*, Springer-Verlag, **1999**.

[4] O. Madelung, U. Rössler, et al., *Landolt-Börnstein - Group III Condensed Matter, Numerical Data and Functional Relationships in Science and Technology, Vol. 41C: Non-Tetrahedrally Bonded Elements and Binary Compounds I*, Springer-Verlag, **1998**.

[5] G. Chiarotti, *Landolt-Börnstein - Group III Condensed Matter, Numerical Data and Functional Relationships in Science and Technology, Vol. 24C: Interaction of Charged Particles and Atoms with Surfaces*, Springer-Verlag, **1995**.

[6] P. T. Cunningham, S. A. Johnson, et al., *Journal of The Electrochemical Society* **1971**, *118*, 1941.

[7] E. Zintl, A. Harder, et al., *Zeitschrift für Elektrochemie und angewandte physikalische Chemie* **1934**, *40*, 588.

[8] C. de Mello Donegá , R. Koole, *The Journal of Physical Chemistry C* **2009**, *113*, 6511.

D

Figures and tables

List of figures

Figure 1. 1: Appropriate the LCAO theory the energetic structure from single atom to bulk semiconductor pass discrete energy levels to merge into continuous bands.... 4

Figure 1. 2: Increasing particle sizes result in red shifted first absorbance maxima and decreased band gap energies. 4

Figure 2. 1: General reaction scheme of the processes present in a standard hot injection synthesis. 13

Figure 2. 2: Nuclei radius *r* as function of Gibbs free energy ΔG in supersaturated solutions. 15

Figure 2. 3: Model of a diffusion layer around a spherical particle of radius r.......... 16

Figure 2. 4: LaMer-Dinegar-plot: development of monomer concentration with proceeding reaction. 20

Figure 2. 5: Illustration of the *quasi*-seeded growth approach........ 22

Figure 2. 6: Model of a core/shell QD in a solvent droplet. 23

Figure 2. 7: Types of core/shell nanoheterostructures. 24

Figure 3. 1: CdSe quantum dots prepared via the *quasi*-seeded growth (qsg) approach result in optical spectra (Abs: a, PL: b) of improved quality, with respect to their size distribution, in comparison to the standard hot injection method (hi)....... 32

Figure 3. 2: CdSe QDs obtained utilizing the qsg approach result (a) in a smaller final particle size with (b) increased particle concentrations and (c) narrower size dispersion. d) The zinc-blende crystal structure remains uneffected. 33

Figure 3. 3: Precipitated products after thermal decomposition of Cd(oleate)$_2$ in absence (a) and presence of $[(Me_3Si)_2N]_2Sn$ (b) which result in Cd^0 and SnO, respectively........ 35

Figure 3. 4: TEM images of CdSe showing the increased monodispersity of the particles derived following the qsg approach in comparison to the standard hot injection (hi) procedure. 36

Figure 3. 5: Application of the qsg approach in the synthesis of CdTe QDs increases the number of magic-sized clusters and is therefore attributed to affect the nucleation........ 38

Figure 3. 6: Increasing concentrations of the *quasi*-seed species, [Sn] decrease the final particle size, r (a) and increase the QD concentration (b). 39

Figure 3. 7: Applying different quasi-seed concentrations smaller particle sizes than for the standard hot injection method derive from 5-20%, whereas lower or higher amounts result in larger sizes. 41

Figure 3. 8: Size dispersions as derived from Gaussian fits of the photoluminescence peaks show the narrowest values applying 5% of the tin species. 42

Figure 3. 9: QD concentrations increase with increasing *quasi*-seed concentrations according to the proposed mechanism. 43

Figure 3. 10: Highest values for photoluminescence quantum yields (QY) are obtained utilizing 5 to 20% of the *quasi*-seed species. 44

Figure 3. 11: FTIR spectra indicate features of tin oleate as well as silylamide for the structure of the *quasi*-seed tin species after reaction with oleic acid. 46

Figure 3. 12: Spectral improvement is also obtained utilizing lithium silylamide, whereas a mixture of lithium silylamide and tin oleate diminishes the effects. 47

Figure 3. 13: Employing any tin species as well as lithium silylamide shows their activity in accordance with the qsg mechanism, although the evolution of size and size dispersion indicate diminishing effects. 48

Figure 3. 14: The *quasi*-seeded growth mechanism allows for an easy 10-fold up-scaling, whereas a 25-fold protocol demands further optimization. 50

Figure 3. 15: TEM images for the up-scaled syntheses showing narrowest size dispersions for CdSe QDs obtained via the qsg approach for a 10-fold up-scaling. 51

Figure 4. 1: Illustration of the size- and configuration-dependence of the chemical potential of MSCs and QDs. 58

Figure 4. 2: General reaction mechanism for the precursor conversion towards CdTe. 59

Figure 4. 3: Synthesis improvement by means of narrower size dispersions is achieved for cation injection as indicated by more intense and better separated excitonic transitions. 60

Figure 4. 4: TEM image and XRD patterns of CdTe QDs synthesized via two altered injection pathways result both in spherical shaped particles with cubic, zinc blende crystal structure. 60

Figure 4. 5: Temporal evolutions in the absorbance of the raw data indicate the more pronounced excitonic transitions within the cation injection. 62

Figure 4. 6: Significant differences are achieved comparing characteristic parameters for the evaluation of the QD ensemble kinetics. 63

Figure 4. 7: Evolution of the photoluminescence raw data for CdTe QDs obtained via altered injections which reflect the observations obtained by the absorbance data. 66

Figure 4. 8: Following the cation injection higher quantum yields are obtained. ... 67

Figure 4. 9: Chemical reactions about the influence of TDPA on $Cd(oleate)_2$ as well as free TOP. 69

Figure 4. 10: CdTe growth kinetics and size dispersion under conditions of cadmium deficit. 70

Figure 4. 11: CdTe growth kinetics and size dispersion under conditions of cadmium excess. 71

Figure 4. 12: Control experiments under exclusion of TDPA at 270°C. 72

Figure 4. 13: Kinetics of the MSC and QD features for altered injection pathways indicate no direct association between MSCs and QDs. 74

Figure 4. 14: Changes in particle volume indicate random monomer deposition. .. 76

Figure 4. 15: Kinetics of MSC population in accordance with the theory of Jiang & Kelley is not applicable to the present CdTe QD syntheses. 77

Figure 4. 16: The temporal evolutions of the raw data absorption spectra for syntheses utilizing an excess of cadmium indicate a second MSC species at 365 nm. 78

Figure 4. 17: The temporal evolutions of the MSC absorbance features reveal that the decline of the 445 nm species is attended with an increase of the 365 nm population. 79

Figure 4. 18: The temporal evolutions of the raw data absorption spectra for syntheses utilizing a deficiency of cadmium indicate the nonappearance rather than the quick disappearance of the MSC species at 445 nm. 81

Figure 5. 1: TEM images of CdSe QDs obtained via extra precursor addition.......... 93

Figure 5. 2: By constant precursor addition a linear growth rate is suggested (size, PL), whereas the quality of the CdSe QDs gets worsened (dispersion, PL intensity). 94

Figure 5. 3: Lowering the reaction temperature decreases the growth rate as well as results in higher PL intensities. 94

Figure 5. 4: Parallel nucleation may occur by quick injection of large amounts of precursor solutions, whereas small quantities prevent this process. 95

Figure 5. 5: Single injections of a large amount of extra precursor results in a decrease in the ensemble properties to a wider extent in comparison to multiple injections of small quantities. 96

Figure 5. 6: Evaluating a type I coating to CdSe/CdS/ZnS QDs the wavelength of the first absorption transition as well as the PL are red shifted and the PL is intensified. 98

Figure 5. 7: Coating and annealing of initially bare CdSe QDs with a ZnSe shell, resulting in a blue shifted absorbance and emission maxima and decreased PL intensities due to ion diffusion processes and increased shell thicknesses. 99

Figure 5. 8: TEM images of CdSe and CdSe/ZnSe QDs after given reaction times. 100

Figure B. 1: TEM images of a selection of CdTe particles synthesized at 300°C following the cation injection pathway. 128

Figure B. 2: TEM images of a selection of CdTe particles synthesized at 300°C following the anion injection pathway. 128

List of tables

Table 3. 1: ICP-OES measurements of CdSe QDs prepared in the presence and the absence of 10% $[(Me_3Si)_2N]_2Sn$. 37

Table 4. 1: Evolution of ensemble parameters characterizing the growth mode. 64

Table 4. 2: Rate constants as results of a linear fit of different growth regimes. 65

Table 5. 1: Sizes of CdSe and CdSe/ZnSe QDs after specific reaction times estimated from TEM images given in fig. 5.8. 100

Table 5. 2: Ion diffusion within CdSe/ZnSe core/shell structures as a function of time: linear fit. 101

Table A. 1: Investigated *quasi* seed precursor species. 119

Table A. 2: Synthesis details (stoichiometric amounts) for the up-scaling process. 119

Table B. 1: Comparison of particle sizes derived from calculations using data from the absorption spectra and TEM investigations. 129

Table B. 2: Comparison of particle sizes derived from calculations using data from the absorption spectra and TEM investigations. 129

Acknowledgment

This dissertation is the result of three and a half years of work. During this period of time I was supported by many people, scientific and non-scientific, whom I would like to thank. This dissertation was simply impossible without them.

I would like to express my gratitude to my supervisors Prof. Dr. Alexander Eychmüller and Dr. Stephen G. Hickey, for their encouraging and stretching supervision as well as for giving me the opportunity to work in this group.

I'd like to thank Lydia Liebscher, Jan Poppe, Shiding Miao, Subhendu Panda, Vladimir Lesnyak and Zoran Popovic for scientific collaboration attended with fruitful discussions and suggestions. Regarding this kind of useful support, I would like to thank Stefanie Gabriel, Dirk Dorfs, Richard Čapek and Sameer Sapra for helpful discussions and ideas about the hot injection synthesis and its theory.

I'm thankful to the whole Nanofate team in Hamburg, Prof. U. Beisiegel, Prof. Jörg Heeren, Peter Nielsen, Oliver Bruns, Barbara Freund and Denise Bargheer, for their patience in the union of biochemistry and cell biology with physical chemistry. Many difficult questions only could be answered within long lasting and intensive discussions.

Special thanks are owed to my office mates, Aliaksei and Susanne, for many brainstorming and motivating but also deflecting and relaxing conversations.

Many thanks to all members of the Eychmüller group for all the funny hours and the scientific versatility within many discussions and conservations, in particular, tea and coffee times as well as the *Doktorandenstammtisch*.

My deepest gratitude goes to my family, to my mother Anke for her unflagging love and outstanding support throughout my life, and to my father Klaus, who taught me a kind of necessary strength for life. Although he is no longer with us, he is forever remembered. Many thanks also to my brother Marco for the empowering criticizing words and for being there in worse moments of life. I'm thankful to Marita and Peter for their interest in my work and many encouraging words.

The warmest thanks to my wife Ricarda for her sedulous support and motivation, for her shoulder to lean on, her uncomplaining patience and her perpetual love. A big thank also to my little daughter Lena-Marie for incredible happy moments in family.

List of publications

Publications in scientific journals

(in collaboration)

6. Gradated alloyed CdZnSe nanocrystals with high luminescence quantum yields and stability for optoelectronic and biological applications

Subhendu K. Panda, Stephen G. Hickey, Christian Waurisch, Alexander Eychmüller

Journal of Materials Chemistry **2011**, 21 (31) 11550-11555

(5.) Brown adipose tissue activity controls triglyceride clearance

Alexander Bartelt, Oliver T. Bruns, Rudolph Reimer, Heinz Hohenberg, Harald Ittrich, Kersten Peldschus, Michael G. Kaul, Ulrich I. Tromsdorf, Horst Weller, Christian Waurisch, Alexander Eychmüller, Philip L. S. M. Gordts, Franz Rinninger, Karoline Bruegelmann, Barbara Freund, Peter Nielsen, Martin Merkel, Joerg Heeren

Nature Medicine **2011**, 17 (2) 200-205

4. Synthesis and characterization of cadmium phosphide quantum dots emitting in the visible red to near-infrared

Shiding Miao, Stephen G. Hickey, Bernd Rellinghaus, Christian Waurisch, Alexander Eychmüller

Journal of the American Chemical Society **2010**, 132 (16) 5613-5615

(3.) Nanostructured silver substrates with stable and universal SERS properties: application to organic molecules and semiconductor nanoparticles

M. V. Chursanova, V. M. Dzhagan, V. O. Yukhymchuk, O. S. Lytvyn, M. Ya. Valakh, I. A. Khodasevich, D. Lehmann, D. R. T. Zahn, C. Waurisch, S. G. Hickey

Nanoscale Research Letters **2010**, 5 (2) 403-409

2. Size and shape control of colloidally synthesized IV-VI nanoparticulate tin(II) sulfide

Stephen G. Hickey, Christian Waurisch, Bernd Rellinghaus, Alexander Eychmüller

Journal of the American Chemical Society **2008**, 130 (45) 14978-14980

1. Refinement of the crystal structure of dipalladium gallium, Pd2Ga

Kirill Kovnir, Marcus Schmidt, Christian Waurisch, Marc Armbrüster, Yurii Prots, Yuri Grin

Zeitschrift für Kristallographie - New Crystal Structures **2008**, 223 (1) 7-8

Conference proceedings

5. New aspects in the hot injection synthesis to provide large scale high quality quantum dots

C. Waurisch, L. Liebscher, E. Sperling, S. G. Hickey, A. Eychmüller

Proceedings of the International Conference Nanomeeting (Physics, Chemistry and Application of Nanostructures) **2011**, 329-332

4. Synthesis and characterization of cadmium phosphide nanocrystals optically active in the visible to near-infrared

S. G. Hickey, S. Miao, C. Waurisch, A. Eychmüller, B. Rellinghaus

Proceedings of the International Conference Nanomeeting (Physics, Chemistry and Application of Nanostructures) **2011**, 325-328

3. High speed intravital microscopy visualizes the uptake of nanocrystals-labelled triglyceride-rich lipoproteins in stellate cells in vivo

O. Bruns, A. Bartelt, M. Calvo, C. Enrich, C. Waurisch, A. Eychmüller, R. Reimer, H. Hohenberg, U. Beisiegel, J. Heeren

Abstracts of the 78th EAS Congress: Atherosclerosis Supplements **2010**, 11 (2) 4

2. The use of nanocrystals with emission in the visible or near infrared and their applications for photonics and optoelectronics

S. G. Hickey, V. Lesnyak, L. Liebscher, S. Miao, S. Tscharntke, C. Waurisch, N. Gaponik, A. Eychmüller

Proceedings of SPIE **2009**, 7469 (746908) 1-11

1. Demonstration of shape and size control of applications relevant colloidally synthesized IV VI nanoparticulate tin(II) sulfide

S. G. Hickey, C. Waurisch, B. Rellinghaus

Proceedings of the International Conference Nanomeeting (Physics, Chemistry and Application of Nanostructures) **2009**, 321-324

Erklärung

Hiermit versichere ich, dass ich die vorliegende Arbeit ohne unzulässige Hilfe Dritter und ohne Benutzung anderer als der angegebenen Hilfsmittel angefertigt habe; die aus fremden Quellen direkt oder indirekt übernommenen Gedanken sind als solche kenntlich gemacht. Die Arbeit wurde bisher weder im Inland noch im Ausland in gleicher oder ähnlicher Form einer anderen Prüfungsbehörde vorgelegt.

Diese Dissertation wurde im Zeitraum Juli 2008 bis April 2012 an der Technischen Universität Dresden unter der wissenschaftlichen Betreuung von Prof. Dr. rer. nat. habil. Alexander Eychmüller angefertigt.

Es existieren keine früheren Promotionsverfahren.

Ich erkenne hiermit die Promotionsordnung der Fakultät Mathematik und Naturwissenschaften der Technischen Universität vom 23. Februar 2011 an.

Dresden, 03. Mai 2012

Christian Waurisch